2012

Field Monitoring and Evaluation of Curved Girder Bridges with Integral Abutments

Gus Shryack
Iowa State University

Field monitoring and evaluation of curved girder bridges with integral abutments

by

Gus L. Shryack

A thesis submitted to the graduate faculty

in partial fulfillment of requirements for the degree of

MASTER OF SCIENCE

Major: Civil Engineering (Structural Engineering)

Program of Study Committee:
Robert E. Abendroth, Co-Major Professor
Brent M. Phares, Co-Major Professor
Jeramy C. Ashlock
Loren W. Zachary

Iowa State University

Ames, Iowa

2012

Table of Contents

LIST OF FIGURES

LIST OF TABLES

LIST OF VARIABLES

A, B, and C = gauge specific constants given by manufacturer

A_c = the area of concrete

A_p = cross-sectional area of the pile tips'

A_s = the area of the steel

$B_{abutment}$ = width of the abutment

Be = effective slab width,

D = the depth of the web

D_0 = initial reading

D_i = reading at time i

$(EA)_{eff}$, = effective axial rigidity

E_c = the linear elastic modulus of concrete

E_s = the linear elastic modulus of steel

G = correction factor that converts digits to inches (provided by manufacturer)

I_f = moment of inertia of a flange about its smaller principal axis

I_{ytb}(steel) = moment of inertia of the bottom flange for Y-axis bending

I_{ytf}(steel) = moment of inertia of the top flange for Y-axis bending

K = a temperature correction coefficient given by the manufacturer (digits/°C)

K_p = the coefficient of passive lateral earth pressure (psi/psi)

K_q = end-bearing soil-spring resistance

K_v = skin-friction soil-spring resistance

L = length of bridge along curve

L = length of the member

L_{eff} = effective thermal length

L_{cable} = the length the cable

L_c = the length of the concrete member

L_e = equivalent cantilever length

Lg = distance between equivalent Mg moments

L_{gauge} = the distance from the top of the abutment to the pressure cells

L_{max} = the total height of each abutment

L_p = tributary pile length for each soil-skin-friction soil-spring

L_s = the length of the steel member

M = resulting end moment

M and *B* = constants for the model 1127 gauges given by the manufacturer

M_f = lateral bending moment acting on the flanges

M_g = resulting moment at location of strain gauges

M_{lb} = lateral bending moment in the bottom flange

M_{lt} = lateral bending moment in the top flange

M_x = strong axis bending moment

N = a constant of either 10 or 12 (engineer's discretion)

P = applied load on composite section

P = the internal axial force

P_c = applied unit load on concrete

P_s = applied unit load on steel

P_{gauge} = the maximum stress measured at the location of pressure cells

P_{max} = the approximated maximum stress at the bottom of the abutment

P_{total} = the total approximate force applied to each abutment

R = the radius of the girder

Ri = the frequency reading produced by the gauge when the vibrating wire is plucked

Y(NA) = the distance to the neutral axis measured from the center of the bottom flange

Z = depth from top of soil to location of desired stress (in.)

Δ = applied lateral end displacement

d = centerline concrete slab to centerline bottom flange

f_{bw} = tension or compression stress due to warping of the cross-section

t_s = slab thickness

x = distance from center of flange to flange tip

x_i = distance from neutral axis to strain gauge *i* along the X-axis

y_i = distance from neutral axis to strain gauge *i* along the Y-axis

$\bar{y}$ = distance from the center of the bottom flange to the neutral axis

α_c = the thermal expansion of concrete

α_{cable} = the coefficient of thermal expansion of the cable

α_{eff} = the effective thermal expansion coefficient of combined steel and concrete

α_s = the thermal expansion of steel

δ = displacement of composite section

δ_c = displacement of concrete

δ_s = displacement of steel

$\varepsilon_{current}$ = the microstrain reading at its respective time

$\varepsilon_{reference}$ = the microstrain reading on April 28th, 2011 at 6 a.m.

ε_a = internal axial strain

ε_{ylt} = lateral bending strain in the top flange

ε_{ylb} = lateral bending strain in the bottom flange

ε_i = strain reading at gauge *i*

ε_x = strong axis bending strain

ε_t = internal torsional-warping strain

ΔD_{cable} = the correction

$\Delta D_{uncorrected}$ = the reading, in inches, before a temperature correction,

ΔL_{avg} = the average bridge expansion computed via instrumentation data during the surveying time interval

ΔL_s = the surveying expansion referenced to April 28th, 2001 at 6 a.m.,

$\Delta L_s'$ = the surveying expansion at the time of the survey on April 28th, 2011

ΔT_{air} = the ambient air temperature

ΔT_{eff} = the effective bridge temperature

ΔT_c = the change in temperature of the concrete member

ΔT_s = the change in temperature of the steel member

Δd = range on longitudinal movement of fixed pier or integral abutment

$\Delta\varepsilon$ = difference in microstrain

$\Delta\varepsilon_r$ = resistance axial strain

σ_x' = total horizontal stress (psi)

σ_z' = total vertical stress (psi)

ϕ' = effective friction angle of the soil (degree)

γ' = unit weight of soil (lb/in.^{3})

ABSTRACT

The National Cooperative Highway Research Program (NCHRP) has shown concerns regarding the design, fabrication, and erection of horizontally curved steel girder bridges due to unpredicted girder displacements, fit-up, and locked-in stresses. Nationally, up to one-quarter of steel girder bridges are being designed with horizontal curvature, an alarming figure when considering the unknown behaviors of this type of bridge. The primary objective of this work was to monitor and evaluate the behavior of four in-service, horizontally curved, steel-girder bridges with integral and semi-integral abutments. Additionally, the influence and behavior of fixed and expansion piers were considered. A number of steps were performed in order to meet the project objectives. First, a national state department survey was conducted and a literature review was performed in order to understand the state-of-art regarding these types of structures. Second, a monitoring program was developed and installed on six bridges located at the I-35, I-235, and I-80 interchange northeast of Des Moines. Third, a monthly survey was conducted on each bridge with the purpose of tracking the bridge movements, and lastly, the data gathered during the monitoring period of the project was post-processed. The following general conclusions were made from the results of the study: There was no measureable difference between the horizontally curved bridges and straight bridges used in this work with regard to bridge behavior; internal strains were recorded in the composite girders as a result of thermally induced restrained expansion and contraction, and of the recorded strains, axial strain showed the largest ranges; the bridges expanded and contracted with seasons and showed more expansion and contraction near expansion piers than fixed piers. The equivalent cantilever method of steel pile analysis fell short of accurately predicting the relationship between weak axis bending strain in the piles and the pile head displacement; the measured internal stress in the abutment piles due to expansion and contraction of the bridge were generally below 50% of yield stress; and the soil pressures on the abutment backwalls were generally below approximate passive soil pressures.

ACKNOWLEDGEMENTS

I would like to take this time to thank the people that made this work possible. First, I would like to thank my mentors Brent Phares, Lowell Greimann, and Robert Abendroth for their patience and guidance throughout my time as a graduate student at Iowa State University. Second, I would also like to thank Doug Wood and Travis Hosteng for spending countless hours on my project making sure everything ran as smoothly as possible. Third, I would like to thank Andrew Barone, Brady Bogaard, Katelyn Weiler, and Peter Moreau for assisting the project in anything that was asked. Lastly, I would like to thank everyone at InTrans for providing me with a high quality and memorable learning environment.

CHAPTER 1 INTRODUCTION

This chapter presents the background to the project and the problems it addresses, the objective and scope of the project, and the research plan undertaken during the project. The final section of this chapter summarizes the organization of this report.

1.1 BACKGROUND

A report published by The National Cooperative Highway Research Program (NCHRP) raised concerns regarding the design, fabrication, and erection of horizontally curved steel girder bridges. These concerns are centered around difficult-to-predict girder displacements, fit-up issues, and unintended locked-in stresses. Because curved steel girder bridges are used in up to one-quarter of the nation's steel girder bridges, having a better understanding of actual behavior – and therefore having better design methodologies – is of notable importance. In order to have these concerns addressed, the NCHRP developed a research problem statement and gave it high priority for funding.

A major problem facing the Nation today is the need to replace large numbers of bridges. Future engineers will need to utilize cost effective and durable designs in order to meet this challenge. Bridge joints permit relative movement between bridge deck spans and abutments; however they must be continually maintained at a cost to the owner. Therefore, an urgent need exists to reduce bridge maintenance costs by eliminating or reducing deck joints. One way to achieve this is by expanding the use of integral abutments to include curved girder bridges.

1.2 OBJECTIVE AND SCOPE

The combined use of horizontally curved steel girder bridges and integral abutments stands to be a promising design; however this combination is relatively new to the nation, and to Iowa. The purpose of the work summarized herein is to investigate the use of integral abutments on curved girder bridges through a monitoring and evaluation program of in-service bridges.

1.3 RESEARCH PLAN

The objective of the research project was to gather information that will assist in the future design of integral-abutment, curved-girder bridges by monitoring and analyzing the

behavior of curved steel girder bridges with integral abutments. There are three general task groups for this project, each of which consists of several related tasks, as described below.

1.3.1 Task Group I: Information Collection

The use of integral abutments in curved girder bridges has either not been tried with great frequency or is not well documented in the technical literature. As such, the first project task group involved collection of information on the use of these combined structural systems. The following tasks were taken to fulfill this task group's objective:

Task A – Technical Advisory Committee

A Technical Advisory Committee (TAC) was formed to assist the ISU research team regarding issues related to curved girders, integral and semi-integral abutments, and fixed expansion piers. They also assisted in establishing performance metrics that could be used to evaluate the performance of curved-girder, integral-abutment bridges. The TAC was encouraged to provide other information they deemed useful to the research team.

Task B – Survey of available technologies

A survey, which was sent to all the Nation's state DOTs, was conducted to determine if integral abutments have been used for horizontally curved bridges and, if so, what were the significant findings, conclusions, or recommendations regarding these types of bridges. The survey also requested that the state bridge engineers express concerns regarding potential behavioral issues and to provide any specific information related to instrumentation and monitoring of these types of bridges.

Task C – Review of available engineering literature

Although a brief literature search and review had been performed before the project officially began, a more complete review was conducted to determine the past and present use of integral abutments for horizontally curved bridges and to uncover any concerns or problems associated with this type of bridge construction. Since significant information on curved-girder, integral-abutment bridges was not initially found in the literature, two general literature searches were conducted that individually addressed horizontally curved bridges and integral-abutment bridges separately in order to formulate potential behavioral issues and to develop a more refined project scope.

Task D – Inspect existing curved and chorded girder bridges

The re-alignment of the intersection of Interstates I-35, I-80 and, I-235 (Northeast Mix-Master) near Des Moines, Iowa included the demolition of the old bridges and the construction of six new bridges. Several bridge types were used in the reconstruction including curved girder bridges with integral or semi-integral abutments. For this task, two I-235 curved girder bridges were inspected to determine if there was any evidence of problems associated with the use of integral abutments.

1.3.2 Task Group II: Collect and Analyze Data on the Performance of Five or More Bridges

The reconstruction of the Northeast Mix-Master, started in 2008, provided the opportunity to monitor the behavior of curved and straight-steel girder bridges. The interchange design was planned so that semi-integral abutments with expansion joints were used in two curved-girder bridges, and integral abutments were used in two essentially identical bridges. There were six, 26-ft wide roadway bridges included in the research. Bridge characteristics are presented in Chapter 5 of this report. The following tasks highlight the steps taken by this task group:

Task E – Finalize an Instrumentation Plan

Working with the Iowa DOT Office of Bridges and Structures, the research team developed preliminary instrumentation schemes for five of the six Northeast Mix-Master bridges. These schemes are shown in Chapter 5, along with pertinent bridge information. The instrumentation layouts typically consist of strain gauges on girders and other elements, temperature sensors, sensors utilized to monitor the differential girder-to-substructure displacement at expansion piers and semi-integral abutments, and techniques for monitoring the global movement of the substructure elements. Along with the instrumentation placed on the bridges, each of the six bridges was outfitted with eight surveying-type reflectors for the purpose of performing monthly surveys of the bridges. These reflectors were placed on the exterior girders at both abutments and both piers. The survey procedure is discussed further in Chapter 5.

Task F – Monitor and Analyze the Behavior of the Selected Bridges

The bridges were monitored over a period of approximately 18 months. During this

period, the strains, temperatures, and displacements were recorded under a variety of loading conditions.

Task G – Develop and Validate Simple Analytical Models for the Monitored Bridges

Using the collected data, simple analytical models were developed and validated. These models may be able to be extrapolated to other design conditions (e.g., geometry, soil conditions, etc.) that may provide information on other hypothetical situations.

1.3.3 Task Group III. Develop Project Conclusions and Recommendations

The focus of this task group was to summarize the entire project with a goal of developing recommendations that will assist bridge owners with decisions regarding the combined use of curved girders and integral abutments.

Task H – Establish a Meeting with the TAC

A final meeting with the TAC was held so that the research team could present the results of the project and some initial project conclusions. The TAC was then asked to provide detailed input at this time.

Task I – Submit Final Report

The Final Report, presented herein, summarizing the results of the research was the final step for this task group.

1.4 REPORT ORGANIZATION

Chapter 1 introduces the project including the project background, the objective and scope of the project, and the research plan. Chapter 2 presents a literature review discussing the design of horizontally-curved steel-girder bridges, the use of integral and semi-integral abutments is summarized, and circumstances where both have been used are presented. Chapter 3 summarizes a survey conducted of the nation's transportation departments in regard to their current design practices for horizontally curved, steel-girder bridges with integral and semi-integral abutments. Chapter 4 summarizes a bridge inspection conducted on two partially horizontally curved bridges with integral abutments. Chapter 5 presents the experimental procedure. Chapters 6 and 7 present the results from the testing described in Chapter 5. Lastly, Chapter 8 discusses the results of the experiments, Chapter 9 presents an analytical model from the results, and Chapter 10 presents formulated conclusions, recommendations, and suggested future work with curved-girder, integral-abutment bridges.

CHAPTER 2 BACKGROUND/LITERATURE REVIEW

The design and analysis of straight, integral-abutment bridges (IABs) has a long and extensive history dating back as far as the 1930's. These bridges came about after the introduction of the Hardy Cross Method and were considered a viable solution to overcoming the downfalls of expansion joints and expansion bearings (Tennessee DOT, 1996). Although there has been a tremendous amount of research on the thermal response of straight IABs, little attention has been paid to their horizontally curved counterparts. Research on the use of integral abutments on horizontally-curved bridges is scarce and their design is not yet well documented nor understood (Hassiotis, 2006). This chapter summarizes completed work on horizontally-curved, integral-abutment bridges. This chapter also presents work on a very abbreviated summary of select, integral-abutment bridges, and on horizontally-curved, non-integral-abutment bridges.

2.1 Past Work on Thermal Loading on Horizontally Curved IABs

The most recent study to investigate the thermal behavior of horizontally-curved, steel-girder, integral-abutment brides was completed by Doust at the University of Nebraska (Doust, 2011). In this study, a detailed investigation was conducted into the behavior of horizontally- curved, steel-girder, integral-abutment bridges and horizontally-curved, concrete slab, integral-abutment bridges using the finite-element-analysis program SAP 2000. Multiple bridges were modeled with varying horizontal curvatures and total bridge lengths. The study considered the effect of different loading conditions applied to the bridges, namely gravity loads, lateral loads (longitudinal and transverse), temperature effects, concrete shrinkage, and earth pressure. From the investigation, the author concluded that for bridges longer than a specific length, dependent mainly upon bridge curvature, the internal forces due to expansion are smaller in a horizontally-curved bridge than in a straight bridge of similar length. Regarding bridge displacement, the author was able to develop an equation to predict the direction of end displacements of a horizontally-curved, integral-abutment bridge. This was important because the author also concluded that the abutment piles should be oriented to produce strong-axis pile bending in the direction of this maximum displacement. Based on this study, orienting the piles in such a fashion will reduce the maximum bending stress in the piles.

Another study involving curved, integral-abutment bridges was presented in a dissertation by Thanasattayawibul at the University of Maryland (Thanasattayawibul, 2006). This work was a parametric study performed using a three-dimensional finite-element model to investigate the effect that different parameters would have on the behavior of horizontally-curved, steel-girder, integral-abutment bridges. Bridge length, temperature, soil profile type, span length, radius, and pile type were the defining parameters selected in this study. As a result of this study, conclusions and recommendations were made for the future research and for the design of horizontally-curved, steel-girder, integral-abutment bridges. Table 2.1 lists Thanasattayawibul's results. The left column shows the parameter being studied. The middle column shows the results of the stress intensity in the piles as related to bridge radius and span length. The right column shows the results of the lateral displacement of the bridge superstore as related to bridge radius and span length.

Table 2.1. Results from Table 10.1 Thanasattayawibul (2006)

Parameter	Stress Intensity in the Piles	Lateral Displacement of Bridge Superstructure
Increase Bridge Length	• Large radius < small radius -up to 300 ft and 400 ft bridge lengths • Small radius < large radius -between 400 ft and 1200 ft bridge lengths	• Large radius < small radius -up to 400 ft and 600 ft bridge lengths • Small radius < large radius -between 600 ft and 1200 ft bridge lengths
Temperature Increase	• Large radius < small radius -50 ft and100 ft spans • 100 ft spans < 50 ft spans	• Small radius < large radius -50 ft and100 ft spans • 100 ft spans < 50 ft spans
Introduction of Predrilled Holes	• Stress intensity reduction -small radius < large radius -100 ft span < 50 ft span	• Lateral displacement reduction -large radius < small radius
Increase Number of Spans	• Stress intensity reduction -large radius < small radius	• Lateral displacement reduction -large radius < small radius.
Pile Type	• Maximum pile stress intensity -friction ≈ end-bearing	• Maximum superstructure lateral displacement -friction piles ≈ end-bearing pile
Radius Increase	• Stress intensity decrease vs. bridge length range -small radius = short bridge length range vs. large radius • Pile stress intensity increase -small radius < large radius	• Lateral displacement decrease vs. bridge length range -small radius = short bridge length range vs. large radius • Lateral displacement increase -small radius < large radius

2.2 Select Past Work on Thermal Loading on Straight IABs

ABAQUS/CAE 6.5-1 was used to conduct numerical simulations on the response of a three span, IAB to thermal loads (Shah, 2007). The purpose of the study was to investigate the soil-structure interaction due to temperature changes on IABs with different types of soil behind the abutments and along the piles. Three different soil conditions, incorporating non-linear soil response and three different temperature changes, were imposed on a model of the Bermis Road Bridge: F-4-20, Fitchburg, Massachusetts. The non-linear response of the soil was modeled using linear springs and an iterative equivalent linear approach. The spring stiffness was determined based on recommendations by *Manuals for Design of Bridge Foundations* published by National Cooperative Highway Research Program in 1991 (Barker et al., 1991). According to the study, the overall behavior of IABs is significantly affected by the type of soil surrounding the bridge abutments. As expected, an increase in soil compaction adjacent to the abutment results in smaller pile tip displacements and smaller pile bending moments. Also, at lower soil compaction levels the abutment translation tends to be larger and the abutment rotation tends to be smaller; at higher compaction levels the abutment rotation tends to be larger and the abutment translation tends to be smaller. The author also noted that vertical thermal gradient in the abutment, although considered a rigid body, produced bending of the abutment.

Abendroth and Greimann (2005) conducted a thorough investigation into the thermal behavior of IABs. First, an extensive literature review was conducted on the following topics: performance of joint-less bridges, bridge field studies, pile tests (field tests and laboratory tests), analytical studies (thermal analysis and integral-bridge analytical studies), integral-abutment design models (bridge temperature, coefficient of thermal expansion and contraction for concrete, bridge displacement, pile design, and approach slabs), and flange local buckling of I-shaped beams. Next, the thermal load responses of two IABs were monitored as described by Abendroth and Greimann:

> Develop a bridge-monitoring program to obtain long term air and concrete temperature; pile and girder strain; longitudinal and transverse abutment displacements; relative, longitudinal displacements between the bridge girders and their pier caps; pile-

head rotation relative to the abutment pile cap; and abutment rotations in a vertical plane that is parallel to the length of the bridge (1-4).

Next, finite-element models of two integral-abutment bridges were developed. These models were then calibrated and refined using the experimental results. The measured and predicted results of abutment displacements and member strains were compared to verify the accuracy of the finite-element models. Lastly, the authors developed recommendations and design procedures. The recommendations and procedures covered integral-abutment backwalls, pile caps, abutment piles, and connections; design examples were provided. Conclusions the authors drew were as follows: a good correlation exists between longitudinal displacements of the integral abutments and the recorded changes in the average bridge temperatures, the extrapolated maximum bending strains at the flange tip of the HP abutment piles exceeded the minimum yield strain of the steel at one of the bridges and was equal to approximately 73% of the minimum yield strain of the steel at the other bridge, the measured longitudinal strains in the PC girders were within acceptable limits for both bridges, and the vertical rotations and longitudinal displacements of the abutments for both bridges were over estimated by the finite-element models when compared to the measured experimental results. The authors also made a number of design recommendations from the results of their study. Please refer to Chapter 10 of Abendroth and Greimann (2005) for more details on their conclusions.

In 2005 the Federal Highway Administration (FHWA), in conjunction with West Virginia University, hosted a conference on integral abutment and jointless bridges. The purpose of the conference was to establish the current practices with regard to design, maintenance and rehabilitation, and construction of integral abutment and jointless bridges and to present case studies regarding the use of IABs. Each of the topics had five to seven presentations reporting on studies completed across the United States. One example was a presentation by Frosch et al. (2005). In this study the authors, in conjunction with the Indiana DOT, instrumented four bridges in Indiana to observe the in-service behavior of straight, integral-abutment bridges. Some notable conclusions were drawn from the study. First, the movement of the abutment can be conservatively estimated using the theoretical thermal expansion and contraction of the superstructure by $\Delta L=\alpha(\Delta T)L$. Secondly, the primary

thermal response of the abutment is to translate longitudinally and that minor abutment rotations can be ignored for analysis. Lastly, piles integrally connected with the abutment experience double curvature bending but pinned connections can be detailed to eliminate the double curvature.

2.3 Past Work on Thermal Loading on Horizontally Curved Non-IABs

Hall et al. (1999) established design specifications for horizontally-curved, steel-girder bridges. This report was published by NCHRP and was based upon over one hundred studies. Section 3.4 of this report addresses thermal loads in the bridge superstructure. It states:

> According to the Recommended Specifications, curved bridges should be designed for the assumed uniform temperature change specified in AASHTO Article 3.16. The orientation of bearing guides and the freedom of bearing movement is extremely important in determining the magnitude and direction of thermal forces that can be generated. For example, sharply skewed supports and sharp curvature can cause very large lateral thermal forces at supports if tangential movements are permitted and radial movements are not permitted. Under a uniform temperature change, orienting the bearing guides toward a fixed point and allowing the bridge to move freely along rays emanating from the fixed point will theoretically result in zero thermal forces. Other load conditions, however, can dictate the bearing orientation. The bearing restrainys and orientation, as well as the lateral stiffness of the substructure, must be considered in a thermal analysis (15).

Section 3.4 of the Hall et al. report discusses the need, in certain conditions, to consider deck temperature gradients as specified by the AASHTO LRFD Specifications. If the width of the deck is less than one-fifth of the longest span, the bridge is considered narrow and uplift can occur. Section 8.3 of this report addresses thermal induced movements in the bearings and states “Bearing devices should be designed to accommodate movements due to temperature changes in the superstructure and to accommodate rotations about the tangential and radial axes of the girder” (25).

Moorty and Roeder (1992) studied the effect various geometric parameters, orientation of the bearings, and the stiffness and resistance of the substructure had on the thermal response of curved bridges. Analytical models of a 600-ft long, three span, horizontally-curved, steel-

girder bridge had vertically varying temperature distributions applied to them. The location of the fixed point, the bearing orientation, the relative stiffness of the bearings, the stiffness of the piers, and the angle of curvature varied between models. The Sutton Creek Bridge was also used in a field study conducted by the authors to compare and validate the information provided by their models. The Sutton Creek Bridge is a 658-ft long, three-span, horizontally-curved, steel-girder bridge in the Kootenai National Forest in Montana. For the field study, the bridge temperature, the ambient air temperature, and the bridge movements were measured over a three-day period and the wind speed and cloud cover were estimated from local newspapers and radio stations. From their work, Moorty and Roeder were able to draw a number of conclusions about the design of horizontally-curved, steel-girder bridges. For example, the authors state that the method of predicting thermal movements recommended by AASHTO is reasonable for straight orthogonal bridges, but a more refined analysis may be required for skew and curved bridges. Furthermore, an increase in the curvature of the bridge results in an increase in the radial movements and stresses in the bridge. The relative stiffness of the bridge, the girder bearings, and the substructure influence the tangential and radial movements in a horizontally-curved bridge; and the transverse movements and stresses in bridges increase with an increase in the skew angle and the width of the bridge.

CHAPTER 3 SURVEY OF STATES

In March of 2010, a survey of state transportation agencies regarding their experience with horizontally curved bridges with integral abutments was conducted. This chapter covers the purpose of the survey, describes the survey, and reports the information obtained by the survey.

3.1 PURPOSE

The purpose of the survey was to synthesize the state-of-the-practice with regard to the design and construction of horizontally curved bridges with integral and semi-integral abutments and to gather available information on the behavior of these type of a bridges.

3.2 DESCRIPTION OF SURVEY

For this survey, an online questionnaire was utilized. This format helped with distribution of the survey and helped minimize response time. The DOT's were sent an email that asked for their participation in a short questionnaire along with a brief description of the questionnaire and why the survey as being conducted. The DOT's were also provided with a web page link and a password that allowed them access to the questionnaire. The survey consisted of ten questions formulated to assess the agencies experience with horizontally curved steel girder bridges with integral abutments. Following an initial evaluation of the responses, follow-up phone interviews were conducted with the states that were deemed to have the most experience. Of the 50 state agencies, a total of 27 participated, six of which were contacted for the follow-up phone interview.

3.3 INFORMATION GAINED

3.3.1 Reasons for Construction

Out of the responding agencies, those that construct horizontally curved, steel girder bridges with integral or semi-integral abutments indicated that they do so for corrosion protection and elimination of expansion joints/expansion bearings. Some agencies also indicated that they consider restrained girder ends as a benefit for both uplift and torque. Agencies that do not construct horizontally curved, steel girder bridges with integral or semi-integral abutments do so because of poor soil conditions, extreme temperature ranges,

unfamiliarity with design, concerns with additional forces on the girders, and a general lack of need for integral abutment bridges. One state indicated that, "Integral abutments inhibit movements at bridge ends. This movement is necessary to dissipate energy during seismic events."

3.3.2 Published or Unpublished Reports

Agencies were asked if they were aware of any published or unpublished documents that addressed the design, monitoring, or performance of horizontally curved, integral or semi-integral abutment, bridges. Pennsylvania, who was the only state that indicated that they knew of any published information, indicated that they had contracted with Penn State University to monitor four straight integral abutment bridges and to develop a design methodology based on the monitored behavior of the bridges.

Vermont was the only state that was aware of any current or contemplated research regarding horizontally curved, integral or semi-integral abutment bridges. In that work a single curved girder bridge is being monitored. The monitoring began in the early winter of 2009 and, at the time of this survey, had not yet resulted in published information.

3.3.3 Additional Limitations

For the most part, responding agencies do not have limitations on radius, total length, or material type for horizontally curved bridges with integral or semi-integral abutments beyond the limitations that are applicable to straight bridges with integral or semi-integral abutments. Several agencies place a limit on the skew angle and the span length, such as skew angle is limited to 30 to 45° and the span length is limited to anywhere between 250 ft to 450 ft.

3.3.4 Common Design Methods

The most commonly indicated analysis method used in the design of horizontally curved bridges with integral or semi-integral abutments was the grillage method (used by 46% of the respondents). The grillage method is an analysis technique where the physical deck is idealized into an equivalent "grid" of structural members (Hall 1999). The next most commonly indicated analysis method was the finite element method (used by 31% of the respondents). The finite element method is a numerical technique where the structure is idealized into a mesh of elements (Hall 1999). The V-load method was cited as the third most

common analysis method (used by 27% of the respondents). The V-load method is an approximate solution that assumes a distribution of radial forces between the girders. The radial forces are a result of the need to balance axial forces acting on a horizontally curved girder. Diaphragm members are assumed to resist the radial force and, as a result, cause a moment on the inside and outside girders (Richardson 1976). Finally the M/R method, an approximate method used for box girder bridges (Hall 1999), was the least cited analysis method (used by 8% of the respondents). The M/R method is a technique that follows the logic that the difference in total bending moment between any two points is the area under the shear diagram except that it utilizes torsional moments. The total change in total torsional moment between any two points is equal to the change in area under the (M/R – t) diagram between those two points (Richardson 1976). The percentage of respondents that used each respective analysis method do not sum to 100% because several (31%) respondents use more than one analysis method.

3.3.5 Follow-up Interview

Personnel in six states were interviewed by telephone to get further clarification on their initial survey responses. Most of the agencies started using integral abutments in the 1970's. Some agencies started using semi-integral abutments in the 1960's and integral abutments later. None of the agencies have any evidence of thermal expansion performance issues associated with horizontally curved steel girder bridges with integral abutments. None of the interviewed agencies use a specific erection scheme that differs from that for a horizontally curved bridge without integral abutments. All of the agencies believe that expansion and contraction of the bridge occurs with temperature changes; however, each agency has their own method to address this matter. Tennessee is the only state that attempts to fully quantify the thermal movements. All other agencies design structural components to accommodate the thermal movements. Each of the agencies uses approach slabs that are tied to horizontally curved integral abutment bridges. Typically, reinforcing bars are designed to work as a "pin" connection allowing relative rotation but not translation at the slab/bridge joint. Lastly, none of the interviewed agencies had any specific limits placed on the design of these bridges. Each state allows their designers to use their judgment in design of a bridge with suggestions to guide, not limit, their design.

CHAPTER 4 IN-SERVICE BRIDGE INSPECTIONS

On July 26th, 2010 two members of the research team accompanied an Iowa DOT Bridge Inspection crew while they inspected two steel girder bridges that were built in 2005 in the Des Moines, IA area. These bridges are partially curved and have integral abutments. This chapter covers the purpose of the inspection, the location and geometry of the bridges, and the inspection findings. The purpose of the visit was to identify any evidence of problems associated with the use of horizontally-curved, steel-girder bridges with integral abutments.

4.1 BRIDGE LOCATION AND GEOMETRY

The first bridge inspected was Bridge No. 7707.50235, which carries West 19th Street over I-235 in Des Moines, IA and has a horizontally curved off ramp on the northwest side of the bridge. The bridge cross section near the north abutment is comprised of ten steel girders with variable cross-sectional dimensions. The three most easterly girders are straight and the other seven girders are curved, with the degree of curvature increasing towards the western-most exterior girder. Due to the increasing degree of curvature, the spacing between the girders also increases as the girders approach the abutment. At the section near the north abutment the bridge deck is crowned over the fourth girder from the east side of the bridge. The deck slope varies to the west of the crown, is constant at 2.5% to the east over the straight girders, and is approximately zero at the sidewalk.

The second bridge inspected was Bridge No. 7708.20235. This bridge carries West 3rd Street over I-235 in Des Moines, IA and has a horizontally curved off ramp on the northeast side of the bridge. The bridge cross section near the north abutment has nine steel girders with varying cross-sectional dimensions. North of the north pier all nine girders have horizontal curvature. The curvature of the girders increases from the west to the easternmost exterior girder. As with Bridge 7707.50235 the girder spacing increases from west to east. The bridge deck is horizontal at the sidewalk then varies while sloping to the east.

4.2 INSPECTION FINDINGS

4.2.1 19th Street Bridge

While inspecting the 19th Street Bridge, the north abutment and girders were visually inspected for cracking and other signs of damage. Also, the bridge deck and guard rail were

visually inspected. Figure 4.1 displays a typical hairline crack in the north abutment near its mid-width. This crack runs vertically along the abutment and extends roughly over about 80% of the visible height of the abutment. This cracking is typical of hairline cracking observed in the abutment. However, these cracks could not be specifically attributed to curvature of the bridge girders.

Figure 4.1. North Abutment Hairline Crack

Figure 4.2 displays slight cracking near the interface between the steel girders and the north abutment at the bottom flange of the steel girders. These cracks typically are oriented downward at a 45° angle from the corners of the bottom flange. These cracks appeared at each of the girder-to-north abutment connections.

Figure 4.3 displays cracking in the off-ramp slab that runs perpendicular to the expansion joint. There were multiple cracks found similar to the one shown. It is interesting to note that these cracks do not follow the curve of the underlying girder.

Figure 4.4 displays transverse cracking in the deck slab. The crack shown is close to the mid-span of the bridge and runs the full width from side-to-side of the bridge. This crack was not the only transverse crack found in the slab, but was the longest.

Figure 4.5 displays transverse cracking in the guardrail that divides the roadway and pedestrian sidewalk. These cracks typically occur at five ft increments along the length of the barrier and occur on both sides of the bridge.

Figure 4.2. North Abutment and Bottom Flange Interface

Figure 4.3. Off-Ramp Slab Cracking

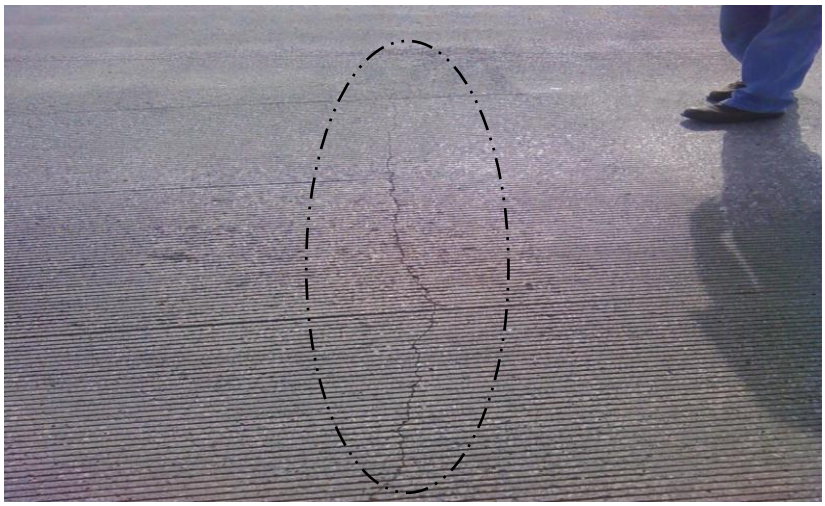

Figure 4.4. Deck Transvers Cracking

Figure 4.5. Guardrail Transverse Cracking

Figure 4.6 shows the joint at the sidewalk between the approach slab and the bridge. Comparing Figure 4.6 to Figure 4.3 reveals that the joint at the sidewalk is open more than the expansion joints in the deck.

4.2.2 Third Street Bridge

While inspecting the 3rd Street Bridge, the north abutment and girders were checked for cracking and any signs of other types of damage. Despite the similarities in design, the West 3rd Street Bridge displayed less damage than that of the West 9th Street Bridge. However, there were some notable discoveries.

Figure 4.6. Approach Slab/Bridge Joint

Figure 4.7 displays slight cracking at the joint between the steel girders and the north abutment at the bottom flange of the steel girders. These cracks run downward at a 45° angle from the corners of the bottom flange. These cracks appeared at each of the girder-to-north abutment connections. Most notably about this figure is the oxidation that has occurred around the cracks and below the girder.

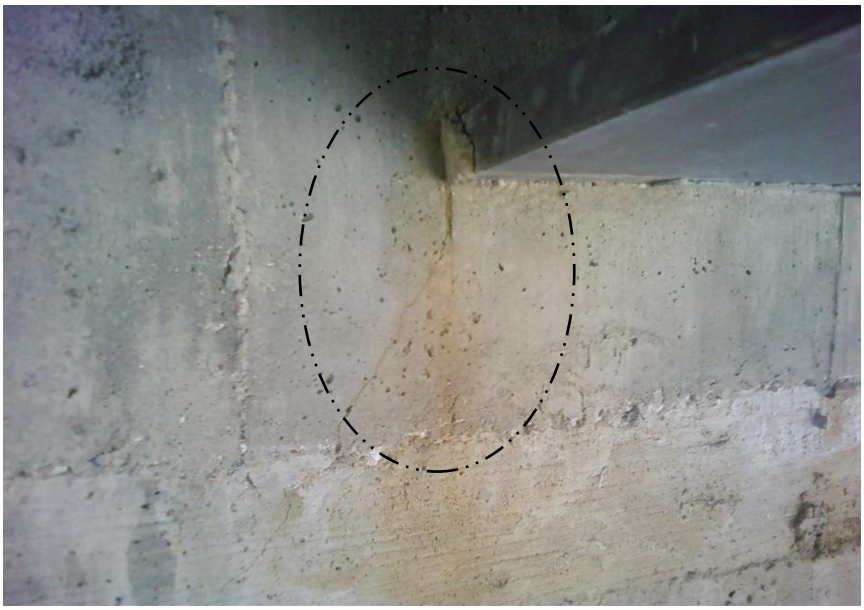

Figure 4.7. North Abutment and Bottom Flange Interface

Figure 4.8 is another photograph of cracking occurring in the abutment. This figure shows evidence of salt water infiltration as indicated by the formation of calcium carbonate crystals around the cracks.

Figure 4.8. Calcium Carbonate Formation

While on inspection, a possible fatigue crack indication, shown in Figure 4.9, was found in the girder-to-diaphragm connection of one of the horizontally curved girders. Upon further testing conducted by the Iowa DOT, the defect identified on the weld toe adjacent to the top flange on the stiffener to the web weld was the result of a lack of fusion at the weld toe.

Figure 4.9. Girder-to-Diaphragm Welded Connection

CHAPTER 5 EXPERIMENTAL }ROCEDURE

One of the principal aspects of this project was to monitor the behavior of horizontally curved, steel girder, integral and semi-integral abutment bridges under changes in temperature and live load. As such, six bridges constructed by the Iowa DOT were instrumented with various sensors at various locations. Behaviors under live loads were evaluated using point-in-time testing and the behaviors under temperature variations were monitored for a period of approximately 18 months.

5.1 BRIDGE LOCATION AND GEOMETRY

5.1.1 Site Plan View

The intersection of Interstate 80, Interstate 35, and Interstate 235 on the northeast side of Des Moines, also known as the North-East Mix Master (NEMM), was the location for the testing associated with this work. Overall, there were six, 26-ft-wide roadway bridges that were included in the research. The interchange layout was configured such that semi-integral abutments were used in two of the curved bridges and integral abutments were used in two of the curved bridges. In general the bridges had geometries that made them essentially mirror-images. Two other ramp bridges at the NEMM are straight with integral abutments and are generally in this work for comparison purposes. Figure 5.1 displays the location and site layout of the NEMM.

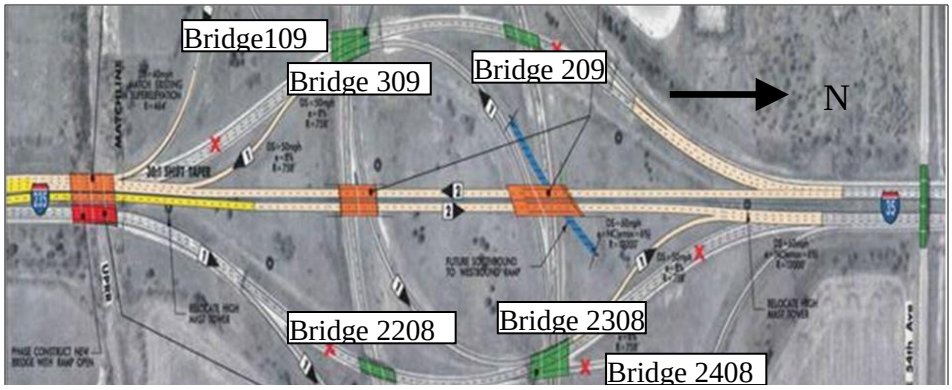

Imagery ©2011 DigitalGlobe, GeoEye, USDA Farm Service Agency, Map data

Figure 5.1. NEMM bridge location and site layout

The six bridges labeled in Figure 5.1 are part of an on ramp or an off ramp at the NEMM interchange. The Iowa DOT assigned the bridge labels, identifying them as shown in the

figure. The top left bridge, Bridge 109; and the bottom right bridge, Bridge 2408; are the straight, steel-girder bridges with integral abutments. The remaining four bridges are the horizontally curved, steel-girder bridges with integral and semi-integral abutments: Bridge 209, 309, 2208, and 2308. The center of curvature for each of the horizontally curved bridges is the same for all four girders of the same bridge and therefore the radii for the girders vary.

5.1.2 Bridge Configurations

Bridge 109 is a one lane, three-span bridge with a straight-alignment and spans of 80 ft, 144 ft, and 80 ft, as shown in Figure 5.2. The spans are measured between the centerline of the abutments and the piers. The baseline of the bridge, a line that is a base for measurement or for construction, is located 4 ft – 6 in. from the west exterior girder and the abutments and piers are skewed 15°. The bridge abutments are integral abutments, the south pier is an expansion pier (EP), and the north pier is a fixed pier (FP).

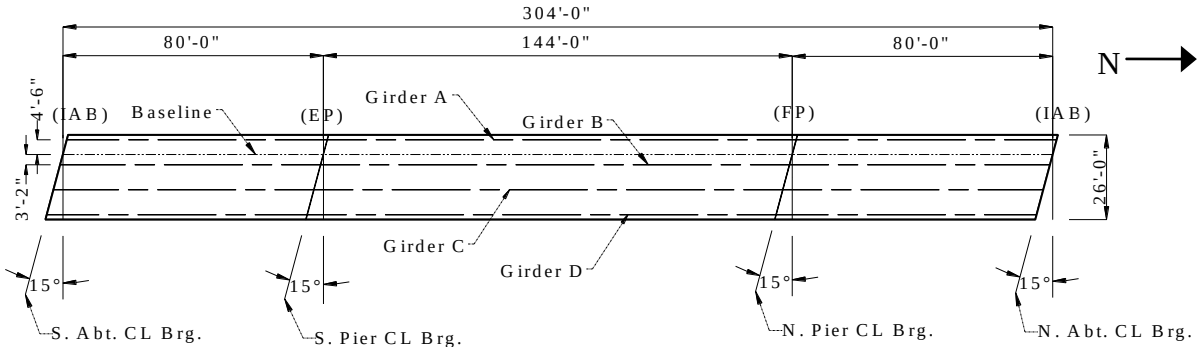

Figure 5.2. Bridge 109 plan view

Bridge 209 is a one lane, three-span, semi-integral abutment bridge with a 1,340 ft horizontal curvature radius, and spans of 90 ft, 152 ft, and 90 ft, as shown in Figure 5.3. The spans are measured along the bridge baseline between the centerline of the abutments and the piers. The baseline is located 4 ft - 6 in. east of the centerline of the west exterior girder (i.e., Girder A). The abutments and piers are skewed at a 35° right ahead. The radius of the baseline is 1,340 ft. The abutments are semi-integral abutments, the south pier is an expansion pier, and the north pier is a fixed pier.

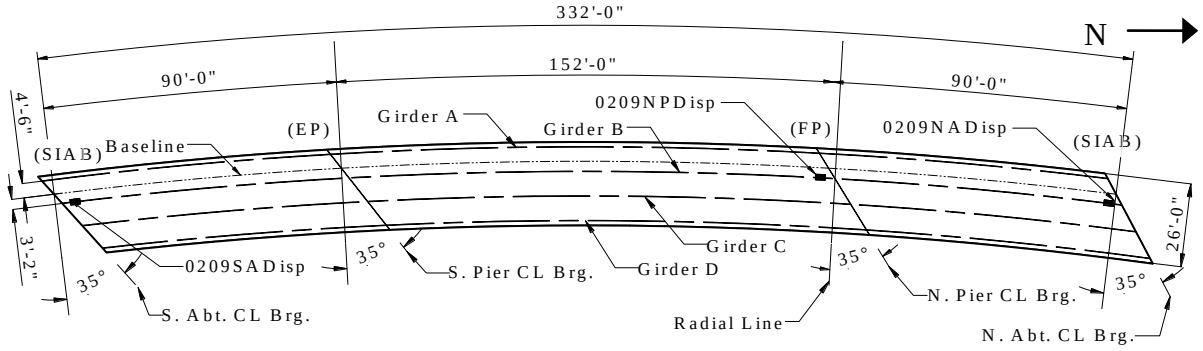

Figure 5.3. Bridge 209 plan view

Bridge 309 is a one lane, three span, integral abutment bridge with a 950 ft horizontal baseline curvature radius, and spans of 85 ft, 149 ft, and 85 ft, as shown in Figure 5.4. The baseline is located 2 ft – 6 in from the west exterior girder, measured perpendicular to the roadway. The abutments and piers are skewed at 15° left ahead. The south pier is a fixed pier and the north pier is a fixed pier.

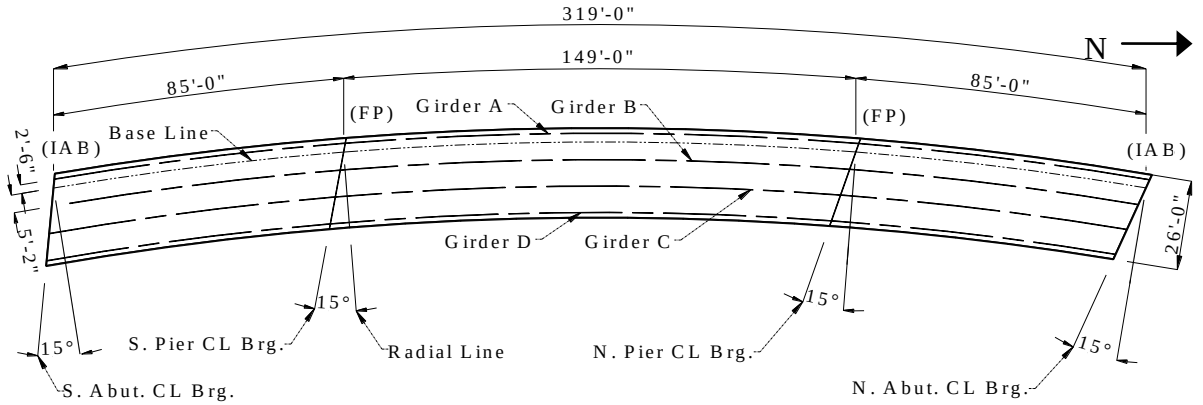

Figure 5.4. Bridge 309 plan view

Figure 5.5 shows the plan view for Bridge 2208. This bridge is a one lane, three span bridge with a horizontal radius of 1340 ft and spans of 90 ft, 150 ft and 90 ft. The baseline is located 4 ft – 6 in. west of the east exterior girder, and the abutments and piers are skewed at 35° right ahead. The abutments are integral abutments, the south pier is an expansion pier, and the north pier is a fixed pier.

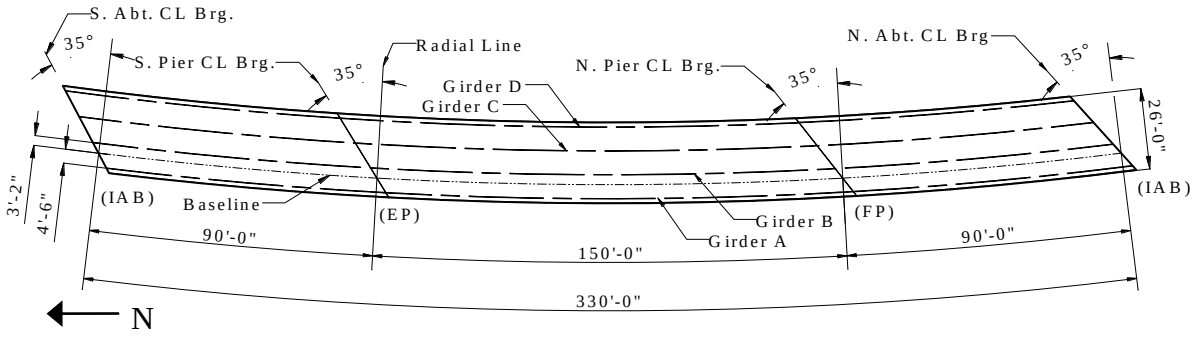

Figure 5.5. Bridge 2208 plan view

Bridge 2308 is a one lane, three span semi-integral abutment bridge with spans of 80 ft, 142 ft and 80 ft and a horizontal curvature of 950 ft, as shown in Figure 5.6. The baseline is located 2 ft – 6 in. from the east exterior girder, and the abutments and piers are skewed at 35° left ahead. The north and south piers are fixed piers.

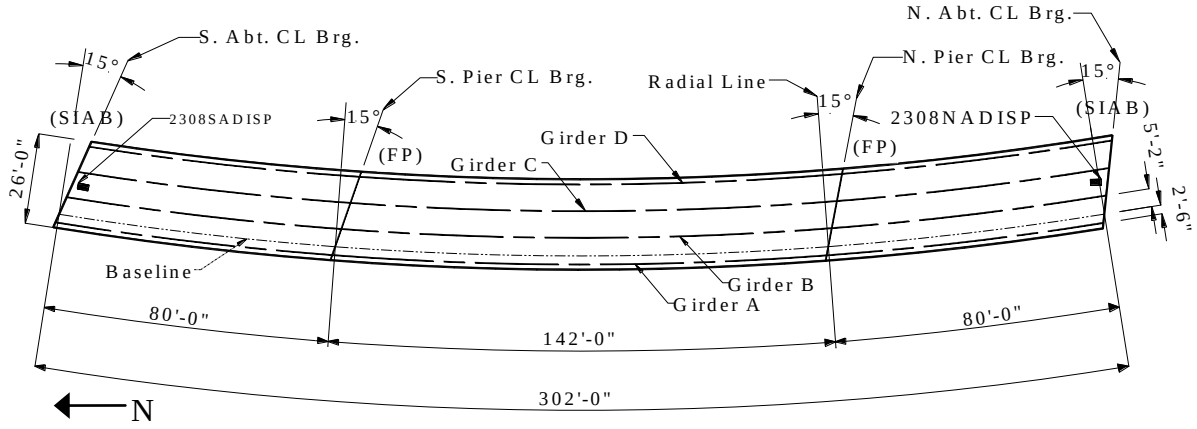

Figure 5.6. Bridge 2308 plan view

Bridge 2408 is a one lane, three span integral abutment bridge with spans of 80 ft, 144 ft and 80 ft, as shown in Figure 5.7. The abutments and piers are skewed at 15° left ahead. The south pier is a fixed pier and the north pier is an expansion pier.

Geometric similarities and differences for the six brides become more apparent in a tabular presentation than with the separate plan views for these bridges that are shown in Figure 5.2 through 5.7. Table 5.1 lists the length, width, skew angle, curve, radius, spans, abutment type, and pier fixity for each bridge.

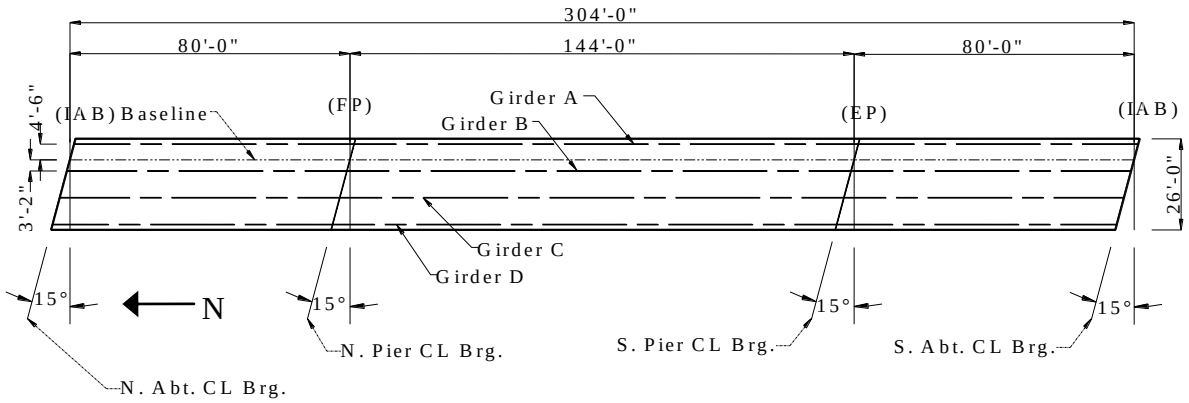

Figure 5.7. Bridge 2408 plan view

Table 5. 1. NEMM bridge geometry

Design No.	109	209	309	2208	2308	2408
Length (ft)	304	332	319	330	302	304
Width (ft)	26	26	26	26	26	26
Skew (°)	15	35	15	35	15	15
Radius (ft)	N/A	1340	950	1340	950	N/A
Spans (ft)	80-144-80	90-152-90	85-149-85	90-150-90	80-142-80	80-144-80
Abut. Type	Integral	Semi-Integral	Integral	Integral	Semi-Integral	Integral
S. Pier Fixity	Expansion	Fixed	Fixed	Expansion	Fixed	Fixed
N. Pier Fixity	Fixed	Expansion	Fixed	Fixed	Fixed	Expansion

After an examination of Table 5.1, one will notice there are bridge pairings based on general geometry and restraint conditions. Additionally, all bridges are generally similar in terms of span lengths and total length. Bridges 109 and 2408 are both straight bridges with the same abutment type and the same skew angle. The only notable difference between these two bridges is the geographic location of their expansion and fixed piers. Bridges 209 and 2208 share similar span lengths, total length, radius of horizontal curvature, pier fixity, and skew angle. The only major difference between the two bridges is their abutment type. Bridges 309 and 2308 are almost identical to one another. The only major difference between Bridges 309 and 2308 is the abutment type.

5.1.3 Bridge Cross Section

Except for the girder dimensions and diaphragm configuration, the cross-sectional properties for all six bridges are similar. Each of the bridges has a roadway width of 26 ft and a total width of 29 ft-2 in. The horizontally curved bridges have non-composite bent plate diaphragms and the straight bridges have cross frames with WT horizontal members and angle diagonal members. The typical bridge cross section is shown in Figure 5.8. The left half of the figure shows the diaphragm configuration for the horizontally curved bridges and the right side of the figure shows the cross frames of the straight bridges.

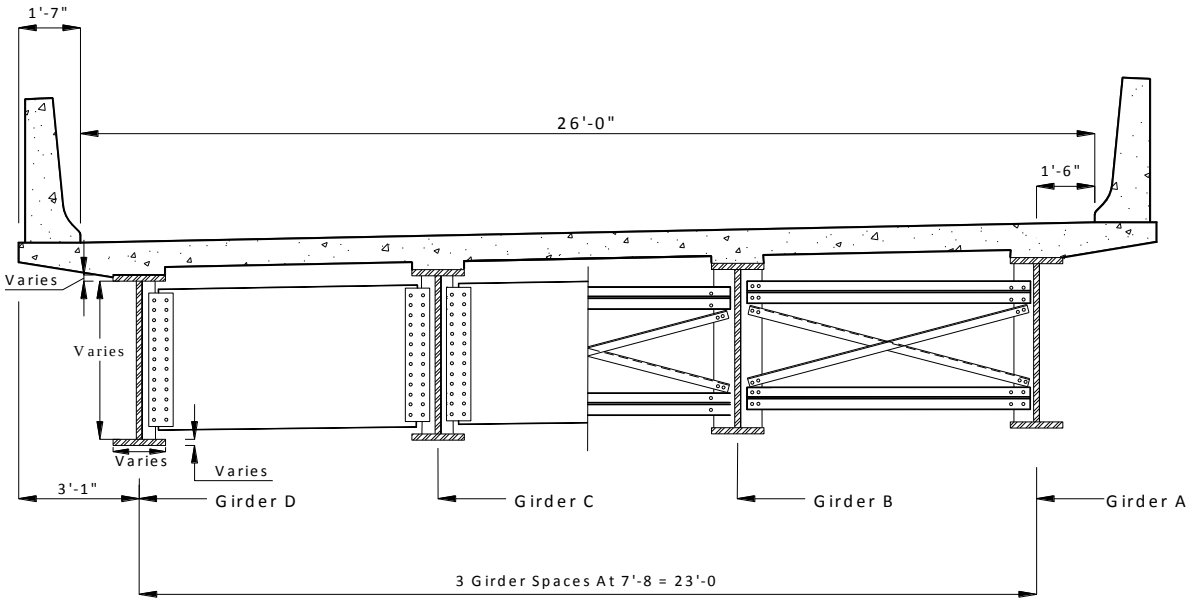

Figure 5.8. Typical bridge cross section

For the six bridges at the NEMM, the Iowa DOT labeled the west exterior girder as Girder A and the east exterior girder as Girder D. However, in this work, the exterior girder on the outside of the curve has been labeled Girder A and the exterior girder on the inside of the curve has been labeled Girder D. Therefore, for the four horizontally curved bridges, Girder A measures the longest total length. Similarly, Girder D measures the shortest total length. The two straight bridges are labeled in a similarly consistent manner and that Girder A and Girder D have the same geometrical properties for a particular bridge. Relabeling was done to eliminate confusion while comparing results between monitored girder locations.

5.1.4 Girder Cross Section

All six bridges were constructed with welded, I-shaped, plate girders. Along with the variation within a span and from span-to-span, field splices and slab haunches change the cross-sectional properties of the girders. In this work variations in slab haunches were ignored. Table 5.2 lists the girder dimension at the locations within each span that were monitored with strain-gauges. The gauge locations are discussed in Section 5.2.2.

Table 5.2. Steel girder dimensions (all dimensions in inches)

Bridge	Span and Girder Location											
	North and South Span Girder A						Center Span Girder A					
	t_{ft}	b_{ft}	t_w	h_w	t_{fb}	b_{fb}	t_{ft}	b_{ft}	t_w	h_w	t_{fb}	b_{fb}
109	-	-	-	-	-	-	3/4	16	7/16	54	1 1/8	16
209	1	22	7/16	42	1	22	3/4	18	7/16	42	1 1/4	22
309	1	20	7/16	48	1	20	7/8	20	7/16	48	1 3/8	20
2208	1	22	7/16	42	1	22	3/4	18	7/16	42	1 1/4	22
2308	7/8	18	7/16	48	1	18	3/4	18	7/16	48	1 3/8	18
	North and South Span Girder D						Center Span Girder D					
	t_{ft}	b_{ft}	t_w	h_w	t_{fb}	b_{fb}	t_{ft}	b_{ft}	t_w	h_w	t_{fb}	b_{fb}
109	-	-	-	-	-	-	3/4	16	7/16	54	1 1/8	16
209	1	20	7/16	42	1	20	3/4	18	7/16	42	1 1/8	20
309	7/8	18	7/16	48	1	18	3/4	18	7/16	48	1 3/8	18
2208	1	20	7/16	42	1	20	3/4	18	7/16	42	1 1/8	20
2308	7/8	16	7/16	48	7/8	16	3/4	16	7/16	48	1 1/8	16

* "-" location with no strain-gauge

To aid in data analysis, a local coordinate system was established for each girder as shown in Figure 5.9. In this coordinate system, while facing north, the positive X-axis direction is to the left and the positive Y-axis direction is downward.

In the positive moment regions the concrete deck was made composite with the steel girders with welded shear studs. In this work it was assumed that the effective cross-section of each composite girder was symmetric about their local Y-axis. The effective slab width is considered twice the distance from the centerline of the girder to the end of the deck overhang for each bridge. A constant slab thickness of 8 in. was also assumed.

The approximate cross sectional properties of Girder A and Girder D, at the location of strain-gauges, are listed in Table 5.3 and Table 5.4 respectively. For each strain-gauge location, Table 5.3 lists $(EA)_{eff}$, the effective axial rigidity; $(EI_x)_{eff}$, the effective flexural axial

rigidity for X-axis bending; I_{ytf}(steel) and I_{ytb}(steel), the moment of inertia of the top and bottom flange for Y-axis bending, respectively; and Y(NA), the distance to the neutral axis (in the Y direction) measured from the center of the bottom flange. These properties were used to calculate internal forces and moments in the girders from the measured strains.

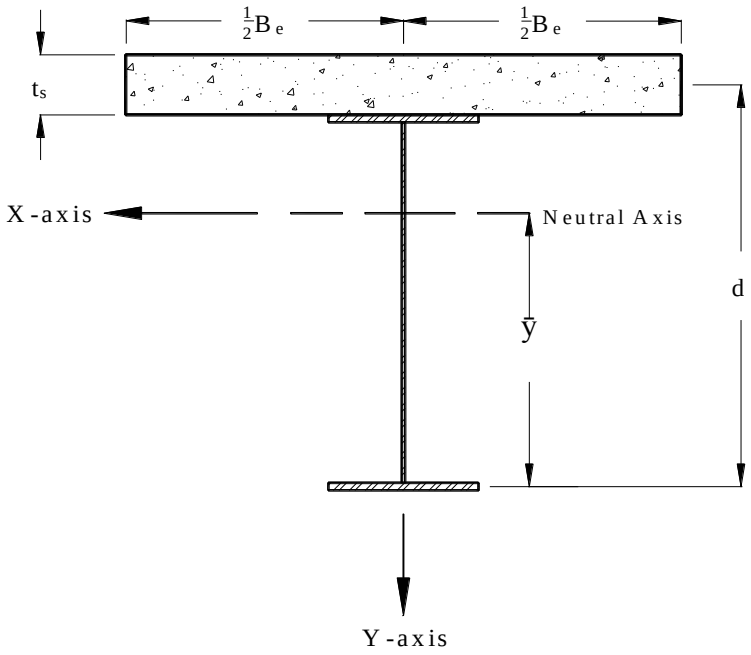

Figure 5.9. Local Girder Coordinate System

where,

B_e = effective slab width,

t_s = slab thickness

d = centerline concrete slab to centerline bottom flange, and

$\bar{y}$ = distance from the center of the bottom flange to the neutral axis.

Table 5.3. Composite section properties Girder A at strain-gauge locaions

	North and South Span Girder A				
Bridge	**$(EA)_{eff}$ (k)**	**$(EI_x)_{eff}$ (k-in.^{2})**	**I_{ytf} (Steel) (in.^{4})**	**I_{ybf} (Steel) (in.^{4})**	**Y (NA) (in.)**
209	$4.1e^6$	$2.0e^9$	$8.9e^2$	$8.9e^2$	$4.0e^1$
309	$4.0e^6$	$2.5e^9$	$6.7e^2$	$6.7e^2$	$4.1e^1$
2208	$4.1e^6$	$2.0e^9$	$8.9e^2$	$8.9e^2$	$3.6e^1$
2308	$3.9e^6$	$2.4e^9$	$4.3e^2$	$4.9e^2$	$4.1e^1$

Center Span Girder A					
Bridge	**$(EA)_{eff}$ (k)**	**$(EI_x)_{eff}$ (k-in.^{2})**	**I_{ytf} (Steel) (in.^{4})**	**I_{ybf} (Steel) (in.^{4})**	**Y (NA) (in.)**
109	$3.7e^6$	$2.6e^9$	$2.6e^2$	$3.0e^2$	$4.6e^1$
209	$4.0e^6$	$2.5e^9$	$3.6e^2$	$11.1e^2$	$3.4e^1$
309	$4.2e^6$	$3.1e^9$	$5.8e^2$	$9.2e^2$	$3.9e^1$
2208	$4.0e^6$	$2.5e^9$	$3.6e^2$	$11.1e^2$	$3.4e^1$
2308	$4.0e^6$	$2.9e^9$	$3.6e^2$	$6.7e^2$	$3.9e^1$

Table 5.4. Composite section properties Girder D

North and South Span Girder D					
Bridge	**$(EA)_{eff}$ (k)**	**$(EI_x)_{eff}$ (k-in.^{2})**	**I_{ytf} (Steel) (in.^{4})**	**I_{ybf} (Steel) (in.^{4})**	**Y (NA) (in.)**
209	$4.0e^6$	$1.9e^9$	$6.7e^2$	$6.7e^2$	$3.6e^1$
309	$3.9e^6$	$2.4e^9$	$4.3e^2$	$4.9e^2$	$4.1e^1$
2208	$4.0e^6$	$1.9e^9$	$6.7e^2$	$6.7e^2$	$3.6e^1$
2308	$3.7e^6$	$2.1e^9$	$3.0e^2$	$3.0e^2$	4.23^1
Center Span Girder D					
Bridge	**$(EA)_{eff}$ (k)**	**$(EI_x)_{eff}$ (k-in.^{2})**	**I_{ytf} (Steel) (in.^{4})**	**I_{ybf} (Steel) (in.^{4})**	**Y (NA) (in.)**
109	$3.7e^6$	$2.6e^9$	$2.6e^2$	$3.0e^2$	$4.6e^1$
209	$3.8e^6$	$2.1e^9$	$3.6e^2$	$7.5e^2$	$3.5e^1$
309	$4.0e^6$	$2.9e^9$	$3.6e^2$	$6.7e^2$	$3.9e^1$
2208	$3.8e^6$	$2.1e^9$	$3.6e^2$	$7.5e^2$	$3.5e^1$
2308	$3.7e^6$	$2.4e^9$	$2.6e^2$	$3.8e^2$	$4.1e^1$

5.1.5 Pier Bearings

Two types of pier bearings were used for the NEMM bridges studied in this work. Figure 5.10 shows an expansion pier bearing. For this pier design a curved sole plate with a pintle is welded to the girder bottom flange. The curved sole plate rests on a neoprene pad, which is on top of the pier cap. An expansion pier is designed to allow rotation about an axis perpendicular to the longitudinal direction of the girder at the pier location and translation in the longitudinal direction of the girder at the pier location.

Figure 5.11 shows a fixed pier bearing. For this pier design a curved sole plate with a pintle is welded to the girder bottom flange. The curved sole plate rests on a masonry plate, which is attached to the top of the pier cap. A fixed pier is designed to allow only rotation about an axis perpendicular to the longitudinal direction of the girder at the pier location.

Translation in the longitudinal direction of the girder is restrained at the pier location.

(a) On Location

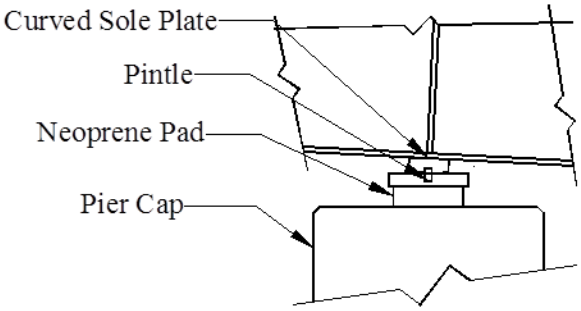

(b)Schematic

Figure 5.10. Expansion pier bearing

(a) On Location

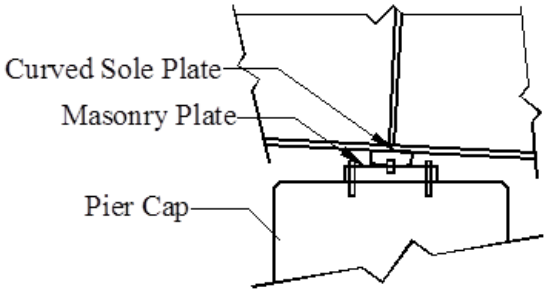

(b) Schematic

Figure 5.11. Fixed pier bearing

5.1.6 Substructure Description

The research presented in this report involved bridges with differing abutment and pier fixity conditions, as listed in Table 5.1. Each IAB at the NEMM was 29 ft – 2 in. wide, the width of each maskwall measured 1 ft – 7 in., and the height of each integral abutment varied from bridge to bridge. Figure 5.12 shows a typical front elevation of an IAB used at the NEMM.

Each girder bears on a short length of an S3x7.5, which bears on the abutment pile cap, as shown in Figure 5.13. The entire abutment is supported by vertical piles, with size and spacing varying from bridge to bridge. For clarity, the reinforcing steel in the reinforced

concrete backwall, mask wall, and pile cap are not shown. Some of the vertical reinforcing bars extend from the pile cap into the abutment backwall and mask walls to form a composite section between the pile cap and the abutment walls.

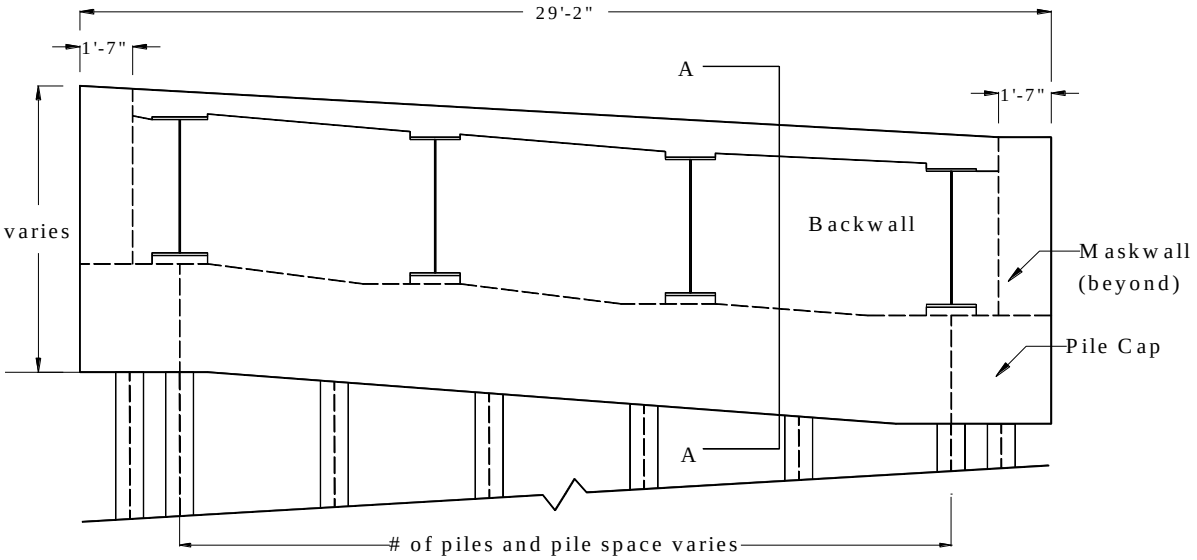

Figure 5.12. Integral abutment – front elevation

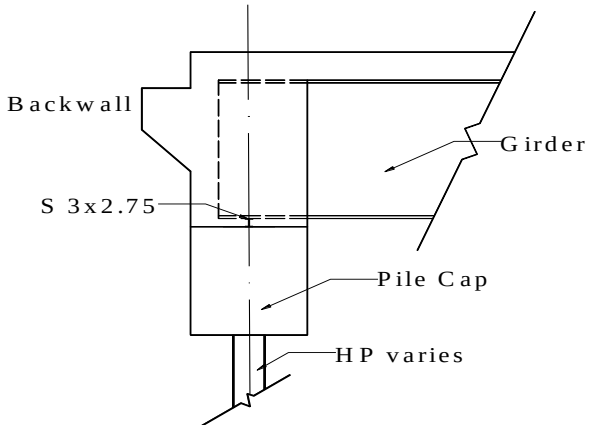

Figure 5.13. Integral abutment section A-A

Figure 5.14 shows a typical front elevation of a SIAB used at the NEMM. Each girder bears on a curved sole plate with a pintle and a laminated neoprene pad, as shown in Figure 5.15.

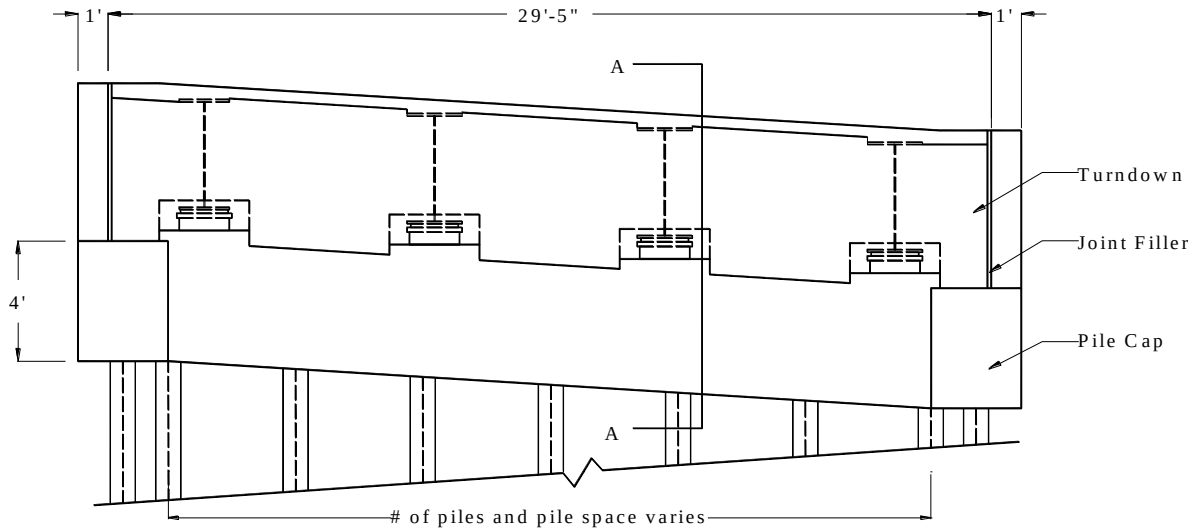

Figure 5.14. Semi-integral abutment – front elevation

Not shown in these figures are the reinforcing steel in the reinforced concrete backwall, mask wall, and pile cap. For the SIAB, no vertical reinforcing bars extend from the pile cap into the backwall. Semi-integral abutments eliminate expansion joints from the bridge deck and their design is intended to eliminate bending strains in the piles due to bridge expansion and contraction because horizontal displacement can occur along the interface between the abutment backwall and pile cap.

5.1.7 Pile Geometry

Each abutment of Bridge 309 (the only bridge to have instrumented substructure elements) had eight HS 10 x 57 piles. Figure 5.16 shows the global coordinate system for the north and south abutment piles of Bridge 309. For these piles, the positive X-axis direction was chosen to be in the same direction as outward expansion of the bridge and the positive Y-axis direction follows the right-hand-rule for a Cartesian coordinate system. For convenience the coordinate system originates at the top of the pile. This coordinate system

facilitates better comparisons between abutment pile bending strains and abutment displacements.

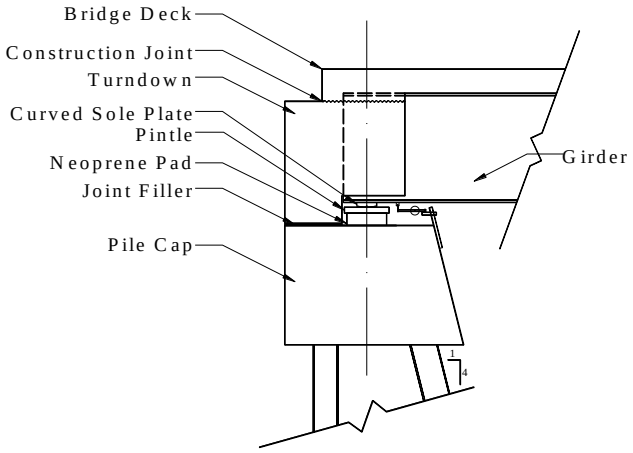

Figure 5.15. Semi-integral abutment section A-A

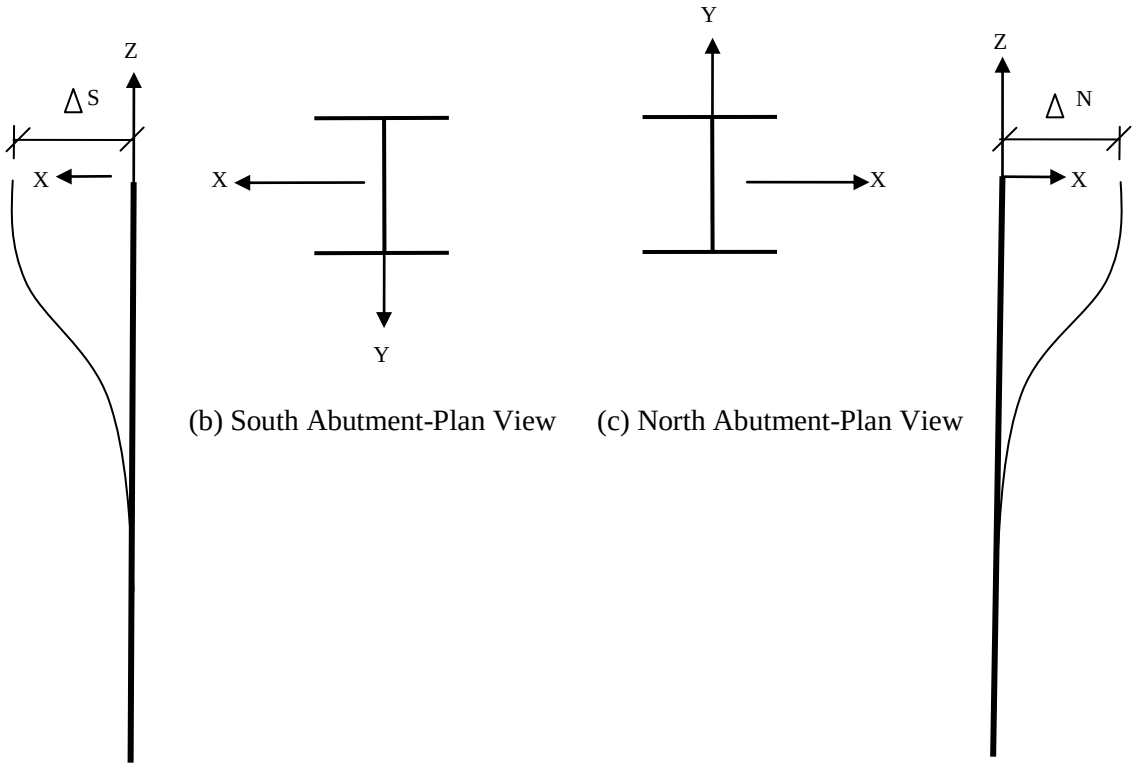

(b) South Abutment-Plan View (c) North Abutment-Plan View

(a) South Abutment–Elevation (d) North Abutment–Elevation

Figure 5.16. Abutment pile coordinate system

5.2 LONG TERM INSTRUMENTATION AND DATA COLLECTION PROTOCOL

5.2.1 Electronic Gauge Instrumentation

Five of the six bridges described previously were instrumented with a variety of electronic devices for measuring changes in strains, displacements, and temperatures that occurred during the bridge monitoring period for the project. The most common instrument attached to the bridges was Geokon's Model 4150 vibrating-wire strain-gauge. This gauge is designed to measure load-induced strain on structural steel members. Strains are measured using the vibrating-wire principle: as the tension in a wire changes, so does its vibration frequency. A change in the vibration frequency relates to a change in strain in the wire and, therefore, any element, to which the gauge is mounted. The tension is measured by plucking the wire and measuring the resonant frequency of vibration with an electromagnetic coil positioned next to the wire (Geokon 2009c). Figure 5.17 shows a vibrating strain-gauge mounted to a piece of steel prior to the application of the protective coatings.

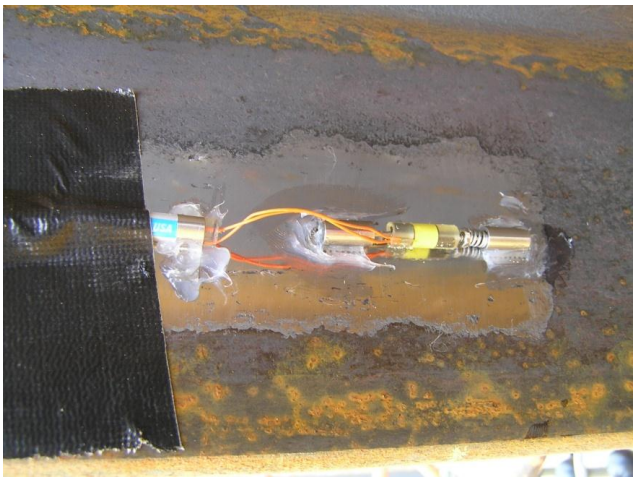

Figure 5.17. Vibrating-wire strain-gauge

For this work, strain-gauges measured strains at mid-length of select girders and spans. Only the exterior girders (Girder A and Girder D) were monitored. Horizontally curved bridges were monitored at each span and one straight bridge, Bridge 109, was monitored at mid-span of the center span.

At the locations monitored, four strain-gauges were attached to the inside face of the top and bottom flanges. The gauges were placed 1 in. from the flange tips and oriented to

measure the longitudinal strains. Four strain-gauges were also attached to the inside faces of both flanges of six piles of Bridge 309. These gauges were placed at a distance of 1 in. from the flange tips. The gauges were located 9 in. below the abutment pile cap.

The next most common instrumentation attached to the bridges is Geokon's Model 4420vibrating wire crack meter. This instrument is designed to measure movement across joints. In the case of this work, the gauge was used to measure the movement between the bridge girders and piers and/or the bridge girders and abutments, depending on the particular bridge being monitored. Herein, this gauge is referred to as an expansion meter. The instrument consists of a vibrating-wire sensing element in series with a spring, which is connected to the wire at one end and to a connecting rod at the other end. As the connecting rod is pulled out from the gauge body, the spring is stretched causing an increase in the tension. This increase in tension is sensed by the vibrating-wire element. Since the tension in the wire is directly proportional to the spring extension, the opening of the joint can be determined (Geokon 2008). Figure 5.18 shows an expansion meter attached to the bottom of a steel girder and to the top of a semi-integral abutment. A similar detail was used to attach an expansion meter at pier loations.

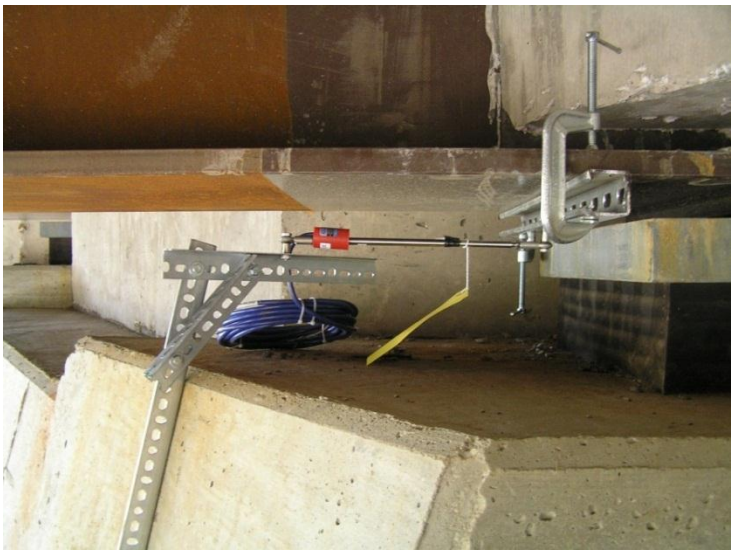

Figure 5.18. Expansion meter

An instrument that was only used on Bridge 309 is Geokon's Model 4427 vibrating-wire long range displacement meter. This instrument is designed to measure displacements of up

to 2 meters. The instrument consists of a spool on which is wound stainless-steel aircraft cable. As the bridge temperature increases, which will induce bridge expansion, the cable unwinds from the spool. When the bridge temperature decreases, which will cause the bridge contraction, the cable is rewound on the spool. The spool is connected to a lead-screw in such a way that the rotation of the spool in converted into a linear motion of the lead-screw. The lead-screw is connected to a Model 4450 vibrating-wire displacement transducer, which measures the linear motion between the two attached objects (Geokon 2009b). Figure 5.19 shows a vibrating-wire long-range displacement meter attached to the abutment backwall. To permit the measurement of relative displacements between two points that are far apart, a long steel aircraft cable was connected to the cable that extends from the reel of the transducer. Bridge 309 was instrumented with three of these sensors allowing relative movement between each of the substructure elements to be monitored.

Figure 5.19. Long range displacement meter

Ambient air temperature was measured using Geokon's Model 4700 vibrating-wire temperature-gauge. Inside the temperature gauge is a tensioned steel wire. The body of the gauge is stainless steel, while the wire is normal grade steel. As the temperature changes the wire and the body expand and contract at differing rates, causing a change in tension in the wire. The change in tension results in a different vibrating frequency for the wire, which is converted into a temperature change (Geokon 2004). Figure 5.20 shows a gauge hanging from the bottom of one of the bridge decks.

Figure 5.20. Temperature gauge

There were a few instrumentation devices that were attached to the bridges whose locations could not be photographed. Geokon thermistors, Model 3800, were place at mid-depth of the bridge decks. These gauges are typically used to measure hydration and cooling temperatures in mass concrete (Geokon 2009a). In this work the gauges measured the temperature of the deck concrete.

On the back side of each abutment pile caps for Bridge 309, two Geokon vibrating-wire pressure cells, Model 4800, were attached. These gauges measure the pressure of the soil induced on the abutment backwall. Earth pressure cells are constructed by welding together the periphery of two stainless-steel plates and leaving a narrow space between them. The hollow space created by the plates is completely filled with de-aired hydraulic oil. The oil pressure is converted to an electrical signal by a hydraulically connected pressure transducer. The electrical signal is transmitted through a signal cable to the readout location (Geokon 2010).

Each of the monitored bridges was instrumented in different ways depending upon individual configurations and the project goals. As shown in Figure 5.2.1, Bridge 109 had the least amount of instrumentation. Four strain-gauges were attached at mid-length of the center span on Girder A and Girder D. Also, an expansion meter 109NPDisp was mounted to the north pier to measure relative movement between Girder B and the pier (a fixed pier).

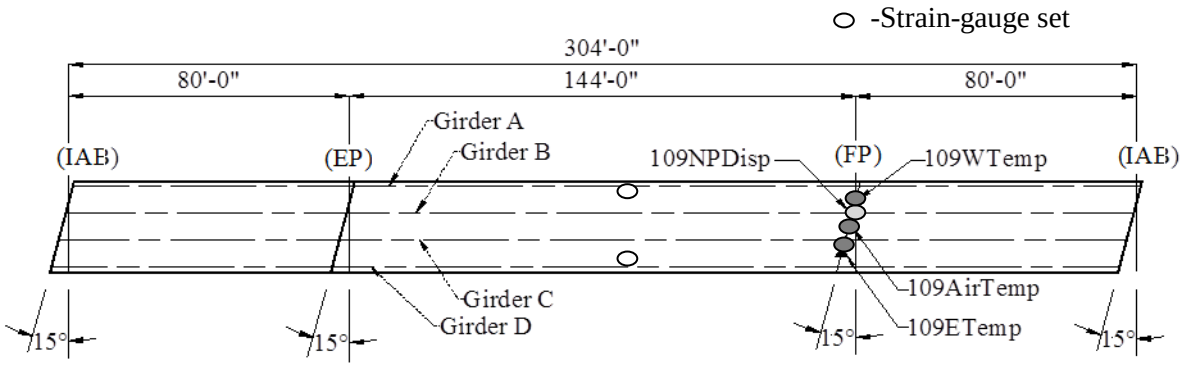

Figure 5.21. Bridge 109 instrumentation

Figure 5.22 shows the instrumentation that was installed on Bridge 209. Strain-gauges were installed on the flanges of Girder A and Girder D at the mid-length of all three spans. Also, expansion meters 209SADisp, 209NPDisp, and 209NADisp were mounted to the south abutment, north pier, and north abutment, respectively. The expansion meters measured the relative movement in a direction tangential to the horizontal curve for Girder B. Relative movement was also measured between Girder B, near each end. Also relative movement between Girder B and the expansion pier was monitored.

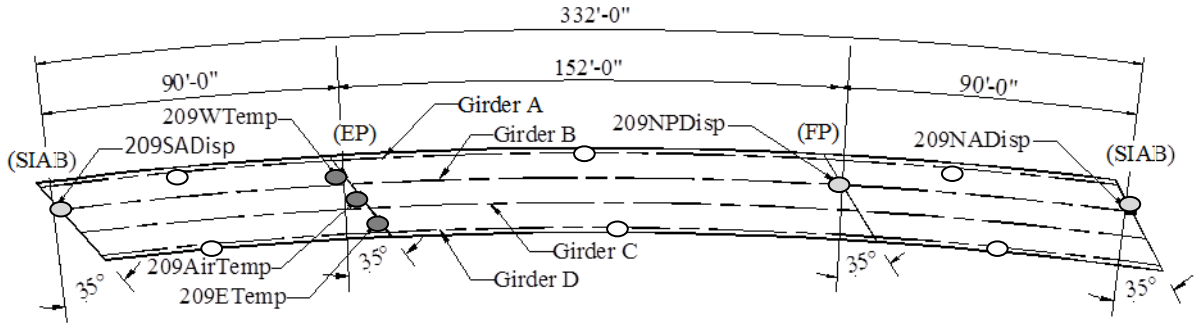

Figure 5.22. Bridge 209 instrumentation

Bridge 309 was the most heavily instrumented bridge. Figure 5.23 shows the location of these monitoring devices. Strain-gauges were attached to Girder A and Girder D at mid-length of each span. Not shown on the figure are the strain-gauges that were attached to the three piles at each abutment. Long range displacement meters 309SAP1Disp, 309P1P2Disp, and 309NAP2Disp were mounted at the south abutment, south pier, and north abutment,

respectively, to measure the change in the chord length of each span. Two pairs of pressure cells 309SAPrW and 309SAPrE, and 309NAPrW and 309NAPrE were mounted at the third points of each abutment width and at the mid-height of the pile cap to measure soil pressure behind the south and north abutments, respectively. Lastly, temperature gauges 309ETemp and 309WTemp were installed inside the deck on the east and west side of the north pier to measure the concrete temperature and temperature gauge 309AirTemp was hung below the deck at the middle of the north pier to measure ambient air temperature.

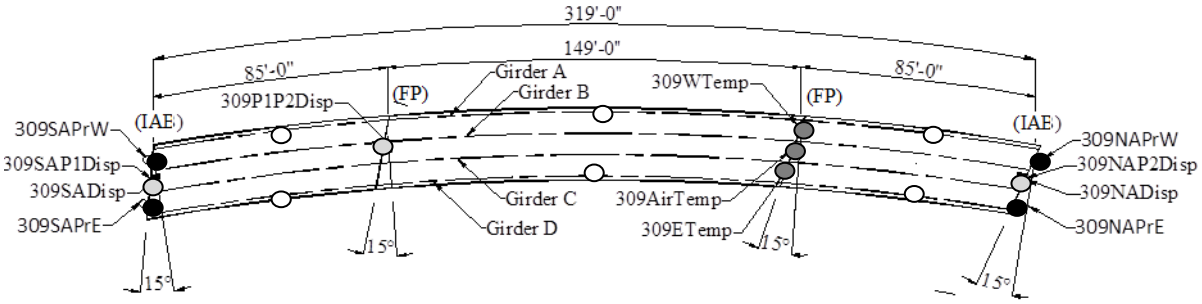

Figure 5.23. Bridge 309 instrumentation

As shown in Figure 5.24, the instrumentation for Bridge 2208 was similar to that used on Bridge 209, with the exception that expansion meters were not placed at the abutments. Expansion meter 2208NPDisp was mounted on the south pier to measure relative movement between Girder B and the pier, an expansion pier.

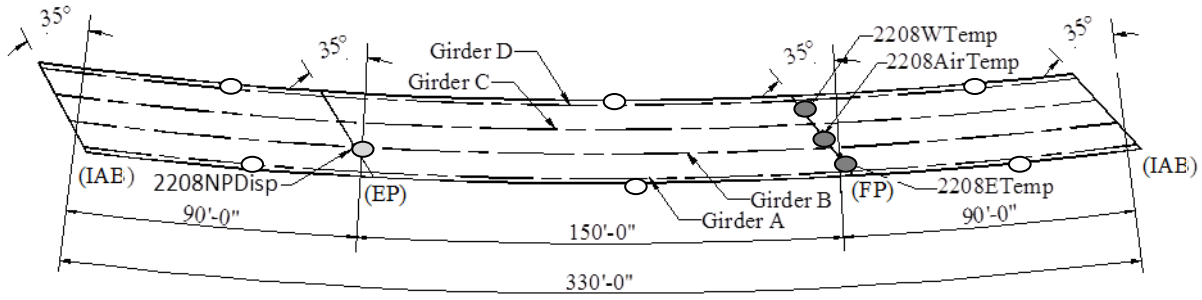

Figure 5.24. Bridge 2208 instrumentation

Figure 5.25 shows that the Instrumentation for Bridge 2308 was similar to that used on Bridge 209, with the exception that expansion meters were not placed at either pier. Expansion meters 2308SADisp and 2308NADisp were mounted on the south and north

abutments, respectively, to measure relative movement between Girder B and the abutments. Also, temperature gauges 2308ETemp and 2308WTemp were cast inside the deck at mid-length of center span to measure the concrete temperature and temperature gauge 2308AirTemp was hung below the deck mid-length of center span to measure ambient air temperature surrounding that location of the bridge.

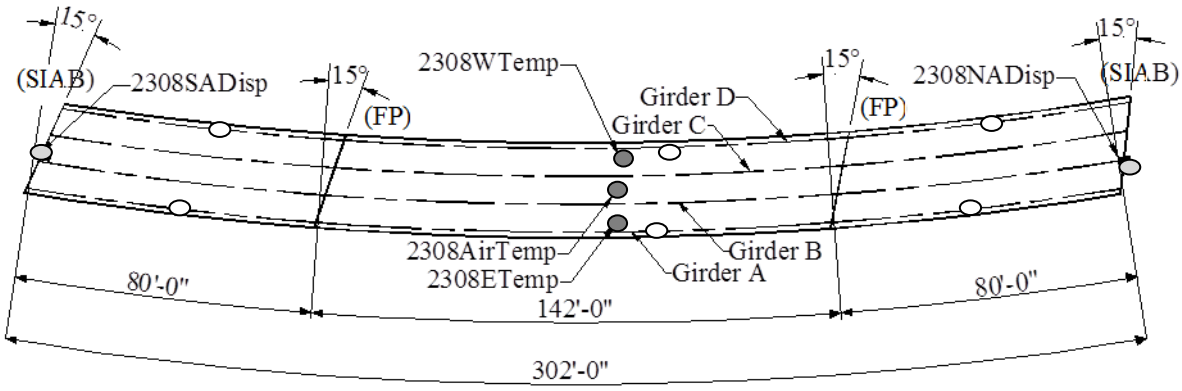

Figure 5.25. Bridge 2308 instrumentation

Along with all the gauges presented in this section, a data collection and storage system for each bridge was assembled, configured, and installed. The data acquisition system consisted of Campbell Scientific data loggers and associated components. The system featured solar power so that line power was not required. Data from each sensor was collected once an hour during the monitoring period.

5.2.2 Survey Instrumentation

Surveying techniques were used to monitor displacements of each of the previously described six bridges. Each bridge had prism reflectors that were mounted near the bearing points of Girder A and Girder D. These reflectors were used as survey targets for monthly surveys of each bridge during the monitoring period. In total, each bridge had eight reflectors that were located at the abutments and piers. As shown in Figure 5.26, a reflector was bolted to the bottom flange of a metal channel track that was attached to the girder bottom flange. Each reflector was positioned directly below the girder web and was aligned for optimal viewing. These reflectors provided a consistent point to survey each bridge.

Figure 5.26. Reflector Instrumentation

Twelve bench marks were installed near the six bridges to establish consistent survey coordinates systems. These benchmarks (which were assumed to not move) were then used to establish the X, Y, Z coordinates for each reflector location. The bench marks consisted of a 3 in. dia. by 10 ft long steel pipe that was embedded 42 in. into the ground. The bottom of the pipe was encased into a concrete footing that rested on undisturbed soil below the frost depth. Figure 5.27a shows a bench mark post during construction. A PVC pipe was sleeved over the steel pipe to shield the steel pipes from direct sunlight that could cause a temperature gradient in the steel pipe and to shield the post from wind that could cause the post to vibrate. A survey reflector was attached to the top of each steel pipe. To shield the reflector from direct sunlight and wind, a T-shaped PVC plumbing fixture was placed over the top of the vertical PVC pipe as shown in Figure 5.27b. The goal with placing these benchmarks was to establish a set of non-moving points in the vicinity of each bridge therefore allowing movements of the bridges to be assessed.

Figure 5.28 shows the relative locations of the reflectors (309P01 through 309P08) that were attached to the Bridge 309 girders, three reflectors (109BM1 though 109BM3) that were mounted to the top of bench mark posts, and the two relative positions where the

surveying instrumentation was placed (309TS1 and 309TS2) for Bridge 309. Note that the locations shown in this figure for the total station and for the bench marks were not drawn to scale. Further, this configuration is representative of that utilized at all bridges. From each total station location, the eight reflectors on the bridge girders and the three reflectors on the bench mark posts were clearly visible when viewed with the survey instrument.

(a) Construction

(b) Operational

Figure 5.27. Survey benchmark

The surveyor used a Topcon GPT-7501 Pulse Total Station to monitor the bridges during the monitoring period of the project. The GPT-7501 Total Station is accurate to 1 in. at 3000 meters and comes pre-loaded with Windows CE.NET.4.2 and TopSURV 7.2 surveying software (Topcon 2007).

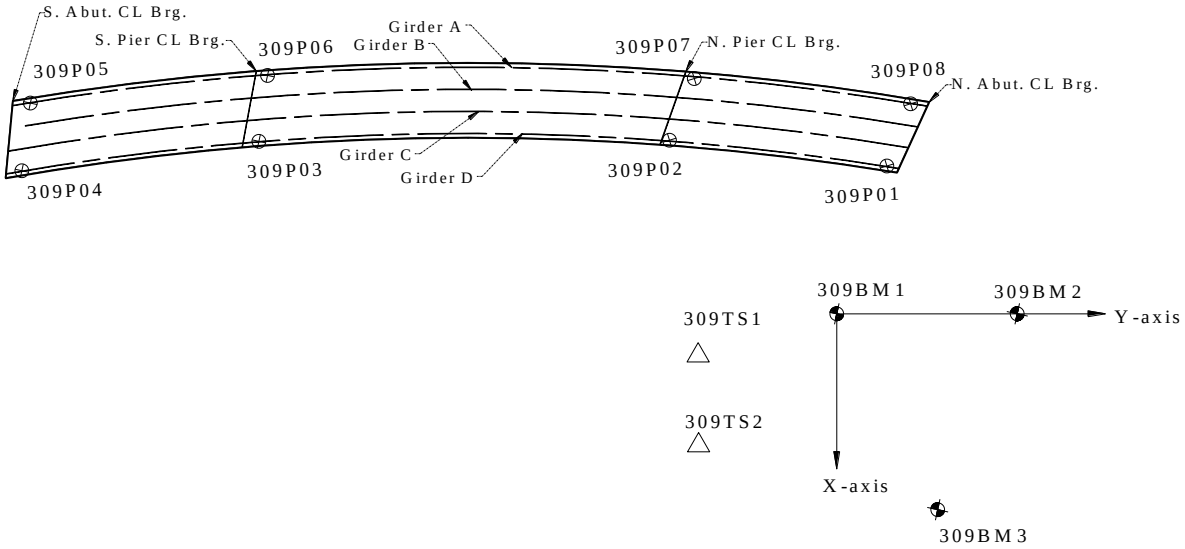

Figure 5.28. 309 Reflector, TS, and BM Locations

5.2.3 Data Collection

Once a month a team traveled to the NEMM. While there, the team retrieved the electronic data and surveyed the bridges in the following order: 309, 109, 2208, 2308, 2408, and 209. The survey process at each bridge took approximately one hour. Three survey cycles were completed in which the surveyor shot and recorded the relative location of the benchmark reflectors and the bridge reflectors. The data for each point were stored in the total station as slope distance, horizontal angle, and zenith angle. In all cycles the total station was rotated through 360° such that any closure error could be accounted for while post-processing the data. After the first three cycles, the surveyor moved and re-setup the total station and repeated the process used during te first three cycles. After all six bridges were surveyed the data were transferred from the total station to a permanent storage location.

The team post processed the data to transform the new survey data into a Cartesian coordinate system originating at BM1. With the Y-axis oriented from BM1 to BM2 and the X-axis 90° clockwise from the Y-axis, as shown in Figure 5.28.

CHAPTER 6 LONG TERM EXPERIMENTAL PROCEDURE AND RESULTS

6.1 PREANALYSIS

6.1.1 Thermal Strains due to Solar Radiation

During initial evaluation of data collected from the strain gauges mounted on the girders an unusual amount of outliers were noticed. It was found that the cover used to protect the strain gauges did not provide enough thermal protection when exposed to direct sunlight. The sunlight raised the temperature of the gauge significantly and resulted in what were determined to be erroneous readings. To remedy this, only girder strain-gauge data collected between 9 p.m. to 6 a.m. were considered in the analysis.

6.1.2 Setting a Reference Date

Because the installed instrumentation measured changes over time a reference date is needed to be set. The reference date is the date where the sensors were essentially zeroed. The reference date was selected to be the reading at 6 a.m. April 28th, 2011. April 28th was the first date that all the measured data were believed to be high quality. Prior to this date, the team had instrumentation issues that resulted in erroneous data.

No April 28th survey data were available at the 6 a.m. reference date since surveys were performed during the daylight. However, the survey from the April 28th survey was set as the reference date for the survey data.

All data in this report are presented with respect to the reference date. Therefore, all date reference data presented here is equal to the difference between the instrument reading at that date and the instrument readings at the reference date. For example, the difference between the strain reading at the reference date and the current strain reading would be calculated as:

$$\Delta\varepsilon = \varepsilon_{current} - \varepsilon_{reference} \tag{6.1}$$

where,

$\Delta\varepsilon$ = difference in microstrain,

$\varepsilon_{current}$ = microstrain reading at its respective time, and

$\varepsilon_{reference}$ = microstrain reading on April 28th, 2011 at 6 a.m.

Since there is a slight difference between the reference date for the instrumentation data and for the surveying data, to compare instrumentation data and surveying data, the difference between the reference positions of the two data sets had to be taken into account. Equation 6.3 presents the proper conversion. Effectively, equation 6.3 aligns the reference date of the survey data and the instrumentation data when they are displayed together.

$$\Delta L_s = \Delta L_s' + \Delta L_{avg} \tag{6.3}$$

where,

ΔL_s = adjusted surveying total bridge expansion referenced to April 28th, 2010 at 6 a.m.,

$\Delta L_s'$ = surveying total bridge expansion at the time of the survey on April 28th, 2011; and

ΔL_{avg} = average bridge expansion computed via instrumentation data during the surveying time interval.

6.1.3 Effective Temperature and Effective Alpha

Since concrete and steel expand and contract at differing rates, it was necessary to formulate an effective coefficient of thermal expansion, α_{eff} , to simulate the composite behavior of the bridge. In this section, the following variables will be utilized.

α_{eff} = effective thermal expansion coefficient of combined steel and concrete,

A_c = area of concrete,

A_s = area of the steel,

E_c = linear elastic modulus of concrete,

E_s = linear elastic modulus of steel,

α_c = thermal expansion coefficient of concrete,

α_s =thermal expansion coefficient of steel,

L_c = length of the concrete member, and

ΔT_c = change in temperature of the concrete member,

L_s = length of the steel member,

ΔT_s = change in temperature of the steel member,

ΔT_{eff} = effective bridge temperature,

P_s = applied unit load on steel,

P_c = applied unit load on concrete,

P = applied load on composite section,

δ_s = displacement of steel,

δ_c = displacement of concrete, and

δ = displacement of composite section.

Equation 6.4 has been used in previous studies and will be used herein to represent the effective thermal expansion (Abendroth 2005).

$$\alpha_{eff} = \frac{(A_c E_c \alpha_c + A_s E_s \alpha_s)}{(A_c E_c + A_s E_s)} \tag{6.4}$$

To describe the temperature of the entire bridge, an effective temperature, T_{eff}, was derived. Figure 6.1 displays a rectangular concrete member with an axial tension load, P_c, and the resulting displacement, δ_c.

Figure 6.1. Concrete memeber

Equation 6.5 is the governing equation that combines the change in length due to the applied load and due to a change in temperature of the concrete member.

$$\delta_c = \frac{P_c L_c}{A_c E_c} + \alpha_c \Delta T_c L_c \tag{6.5}$$

Figure 6.2 displays a rectangular steel member with an axial tension load, P_s, and the resulting displacement, δ_s.

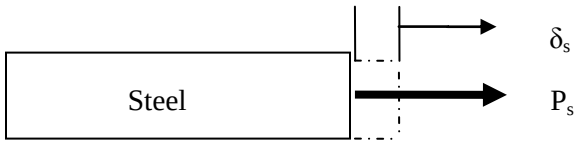

Figure 6.2. Steel member

Equation 6.6 is the governing equation that combines the change in length due to applied load and due to a change in temperature of the steel member.

$$\delta_s = \frac{P_s L_s}{A_s E_s} + \alpha_s \Delta T_s L_s \tag{6.6}$$

Next in a perfectly composite element, it is assumed that the change in lenght of the concrete member, δ_c, is equal to the change in lenght of the steel member, δ_s, and the length of both members, L_c and L_s, are also equal to L. Figure 6.3 displays a composite concrete and steel rectangular member with an axial tension, P, and a resulting change in length, δ.

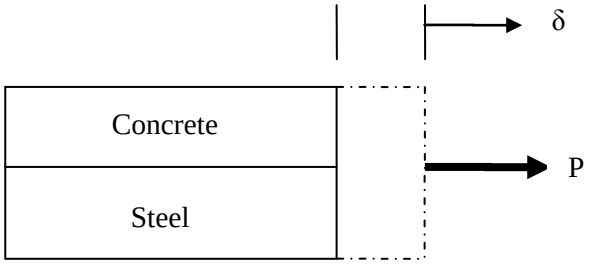

Figure 6.3. Composite concrete and steel member

Considering the assumptions stated in the previous paragraphs and Equations 6.5 and 6.6 and the equation for the effective thermal expansion coefficient for combined steel and concrete (Equation 6.4). An effective bridge temperature can be derived as follows:

1. Since $\delta = \delta_s = \delta_c$ and $L = L_s = L_c$
   a. Then $\delta = \left(\frac{P_s L}{A_s E_s}\right) + \alpha_s \Delta T_s L = \left(\frac{P_c L}{A_c E_c}\right) + \alpha_c \Delta T_c L$
2. If $P_c + P_s = P$ and $P = 0$ for free expansion
   a. Then $P_s = -P_c$
   b. And $\delta = \left(\frac{-P_c L}{A_s E_s}\right) + \alpha_s \Delta T_s L = \left(\frac{P_c L}{A_c E_c}\right) + \alpha_c \Delta T_c L$
   c. Re-arranging like terms $\alpha_s \Delta T_s - \alpha_c \Delta T_c = P_c \left(\frac{1}{A_c E_c} + \frac{1}{A_s E_s}\right)$
   d. Lastly $P_c = \left(\frac{\alpha_s \Delta T_s - \alpha_c \Delta T_c}{\frac{1}{A_c E_c} + \frac{1}{A_s E_s}}\right)$
3. Substitute equation from step 2d into eq. 6.5
   a. $\delta = \left(\frac{(\alpha_s \Delta T_s - \alpha_c \Delta T_c) L}{A_c E_c \left(\frac{1}{A_c E_c} + \frac{1}{A_s E_s}\right)}\right) + \alpha_c \Delta T_c L$
   b. $\delta = \left(\frac{(\alpha_s \Delta T_s - \alpha_c \Delta T_c) L}{\left(1 + \frac{A_c E_c}{A_s E_s}\right)}\right) + \alpha_c \Delta T_c L$
   c. $\delta = \left(\frac{\alpha_s \Delta T_s L - \alpha_c \Delta T_c L + \alpha_c \Delta T_c L \left(1 + \frac{A_c E_c}{A_s E_s}\right)}{\left(1 + \frac{A_c E_c}{A_s E_s}\right)}\right)$

By simplifying step 3c one last time equation 6.7 results. Equation 6.7 gives the free change in length of the combined concrete and steel member under a uniform temperature change.

$$\delta = \left(\frac{A_c E_c \alpha_c \Delta T_c L + A_s E_s \alpha_s \Delta T_s L}{A_c E_c + A_s E_s}\right) \tag{6.7}$$

In a similar manner:

$$\Delta T_{eff} = \left(\frac{\delta}{L}\right)\left(\frac{1}{\alpha_{eff}}\right) \tag{6.8}$$

Substituting equations 6.4 and 6.7 into equation 6.8 produces the final equation for the effective bridge temperature, $\Delta T_{eff.}$

$$\Delta T_{eff} = \frac{(A_c E_c \alpha_c \Delta T_c + A_s E_s \alpha_s \Delta T_s)}{(A_c E_c \alpha_c + A_s E_s \alpha_s)} \quad (6.9)$$

Utilizing the temperatures measured from each of the strain gauges, and from the temperatures gauges embedded in the concrete, an effective temperature could be calculated when all measurements were taken.

6.1.4 Temperature Correction for Long Range Distance Meters (LRDM)

Internal Correction

Temperature ranges greater than 50° Fahrenheit impact a LRDM's displacement reading (Geokon 2009). Given the expected operational temperature ranges, it was necessary to apply a temperature correction to the results. Equation 6.10 is the controlling formula for making such corrections.

$$\Delta D_{corrected} = \Delta D_{uncorrected} + K(T_i - T_0)G \quad (6.10)$$

where,

$\Delta D_{uncorrected}$ = reading, in inches, before a temperature correction,

K = a temperature correction coefficient given by the manufacturer (digits/°C), and

G = correction factor that converts digits to inches (provided by manufacturer).

$\Delta D_{uncorrected}$, and K are calculated by the following equations:

$$\Delta D_{uncorrected} = D_i - D_0 \quad (6.11)$$

$$K = MR_i + B \quad (6.12)$$

where,

D_0 = initial reading,

D_i = reading at time i,

M and B = constants for the model 1127 gauges given by the manufacturer, and

R_i = the frequency reading produced by the gauge when the vibrating wire is plucked.

To calculate R_i it is necessary to use equation 6.13. The quadratic formula is then solved to calculate the values of R_i.

$$D_i = AR_i^2 + BR_i + C \tag{6.13}$$

where,

A, B, and C = gauge specific constants given by manufacturer.

External Correction

An external temperature correction was applied to the cable connected to the LRDMs. Specifically, as the cable's temperature rose above the initial temperature the cable would naturally lengthen. As a result, the measured value would be smaller than actual. Similarly, as the cable's temperature lowered below the initial temperature the cable would naturally shorten. As a result, the measured displacement would be greater than actual displacment. Equation 6.14 shows the appropriate correction that is applied.

$$\Delta D_{cable} = \alpha_{cable} \Delta T_{air} L_{cable} \tag{6.14}$$

where,

ΔD_{cable} = the correction,

α_{cable} = the coefficient of thermal expansion of the cable,

ΔT_{air} = the ambient air temperature, and

L_{cable} = the length the cable.

6.2 MEMBER STRAINS AND FORCES

As mentioned previously, five of the six bridges in the study were instrumented with strain gauges. The data collected from these strain gauges were used to calculate the internal strains and forces induced in each bridge due to ambient temperature changes. Member strains are induced as a result of restraining temperature induced expansion and contraction of a bridge.

6.2.1 Superstructure

Girder Resolved Strains and Forces

As discussed previously, a girder coordinate system was established and the important girder section properties calculated. Figure 6.4 depicts the forces considered in analysis of the composite section. The forces were chosen to align with AASHTO's codified approach for calculating lateral forces due to live loading (AASHTO 4-3).

Referencing Figure 6.4, the following describes each of the external forces induced on each girder, measured by each strain sensor, and then resolved using the subsequently described process:

P represents the axial force induced on the entire cross-section; tension is positive. M_x represents strong axis bending of the entire cross-section, M_x is positive when the top flange is in compression. M_{lt} and M_{lb} represent lateral bending of the top and bottom flange, respectively; as is considered in AASHTO, tension in the flange tip on the outside of the curve is considered positive.

According to AASHTO: (1) flange lateral bending is the bending of a flange about an axis perpendicular to the flange plane due to lateral loads applied to the flange and/or non-uniform torsion in the member (AASHTO 4-3), (2) flange lateral bending stress is the normal stress caused by flange lateral bending (AASHTO 4-3), and (3) lateral moment, M_l, is the total moment about the Y-axis in the top and bottom flange and replaces combined weak axis bending plus torsional warping. For reference Equation 6.15 can be found in the AASHTO Bridge Design Guidelines (Eq. C4.6.1.2.4b-1), and is used to calculate the Lateral Moment a girder cross-section due to live loading (Note: current AASHTO specifications contain no codified approach for calculating temperature induced loadings):

$$M_l = \frac{M_x L^2}{NRD} \tag{6.15}$$

where,

M_x = major axis bending,

L = length of the member,

N = a constant of either 10 or 12 (engineer's discretion),

R = the radius of the girder, and

D = the depth of the web.

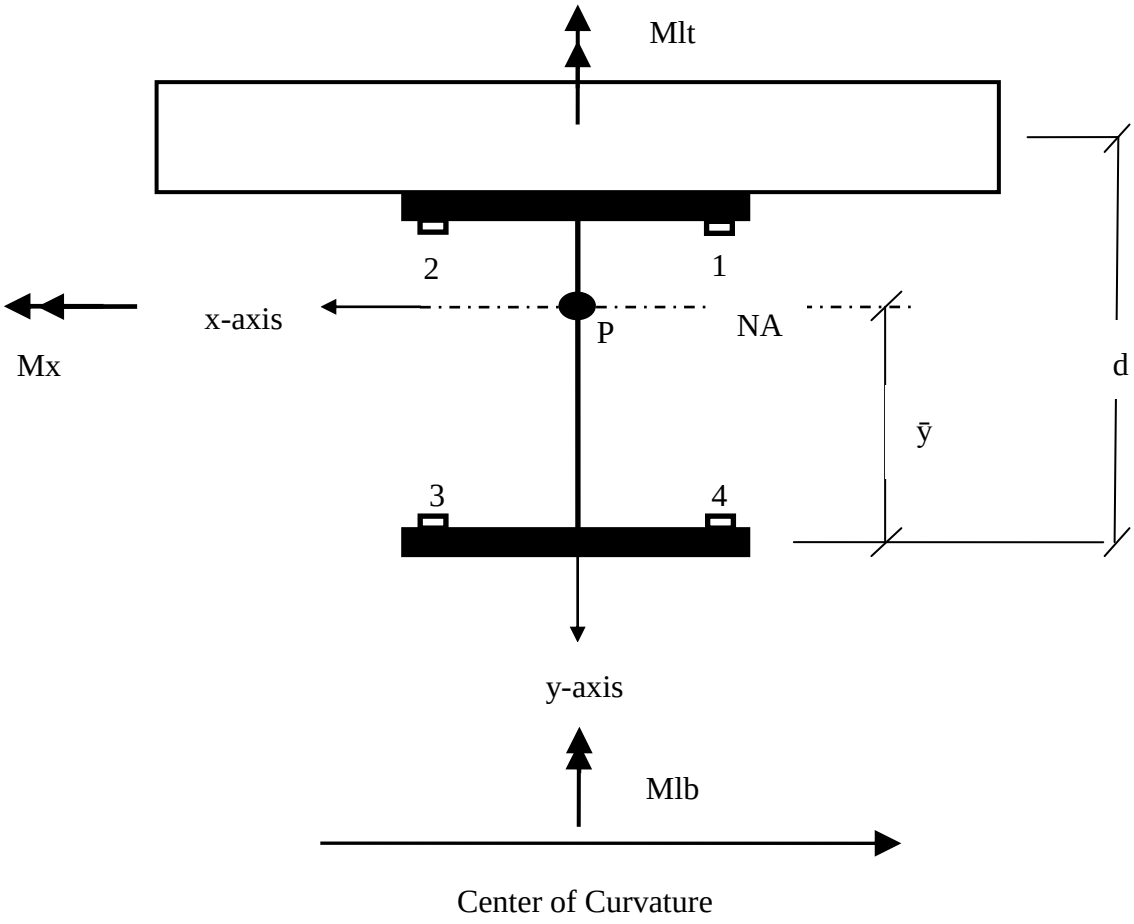

Figure 6.4. Resolved girder forces

Utilizing the four measured strains at each girder cross section and the specific girder cross sectional properties, one is able to calculate the four resolved girder forces described

previously. Figure 6.5 displays a set of matrices that describe the relationship between the four known internal strains at the strain gauge locations and the four desired internal strains.

$$\begin{Bmatrix} \varepsilon_1 \\ \varepsilon_2 \\ \varepsilon_3 \\ \varepsilon_4 \end{Bmatrix} = \begin{bmatrix} 1 & y_1 & x_1 & 0 \\ 1 & y_2 & x_2 & 0 \\ 1 & y_3 & 0 & x_3 \\ 1 & y_4 & 0 & x_4 \end{bmatrix} \begin{Bmatrix} \dfrac{P}{(AE)_{eff}} \\ \dfrac{M_x}{(EI_x)_{eff}} \\ \dfrac{M_{lt}}{E_s I_{yft}} \\ \dfrac{M_{lb}}{E_s I_{yfb}} \end{Bmatrix}$$

Figure 6.5. Four equations and four unknowns

where,

ε_i = strain reading at gauge *i*,

x_i = distance from neutral axis to strain gauge *i* along the X-axis, and

y_i = distance from neutral axis to strain gauge *i* along the Y-axis.

The relationship between internal axial strain and internal axial force is described by equation 6.16. The relationship between major axis bending strain and major axis bending moment is described by equation 6.17. The relationship between lateral bending strain and lateral bending moment in the top and bottom flange in represented by equations 6.18 and 6.19.

$$\varepsilon_a = \frac{P}{(AE)_{eff}} \tag{6.16}$$

where,

ε_a = internal axial strain, and

P = the internal axial force.

$$\varepsilon_x = \frac{M_x y_3}{(EI_x)_{eff}} \tag{6.17}$$

where,

ε_x = strong axis bending strain, and

M_x = strong axis bending moment.

$$\varepsilon_{ylt} = \frac{M_{lt} x_2}{E_s I_{yft}} \tag{6.18}$$

where,

ε_{ylt} = lateral bending strain in the top flange, and

M_{lt} = lateral bending moment in the top flange.

$$\varepsilon_{ylb} = \frac{M_{lb} x_4}{E_s I_{yfb}} \tag{6.19}$$

where,

ε_{ylb} = lateral bending strain in the bottom flange, and

M_{lb} = lateral bending moment in the bottom flange.

Typical Girder Strain Data at Gauge vs. Time

Figure 6.6 through Figure 6.9 illustrate typical girder strain gauge data versus date. Each of the figures represents a specific composite girder flange location and the illustrations represent data from the center span of Girder D on Bridge 309.

Figures 6.6 through 6.9 show a strain change that cycle daily and annually. Generally speaking the daily cycle range is small compared to the annual cycle range. The bottom flange strains show a larger cycle range in both daily and annual cycles, and the bottom flange data shows more scatter than the top flange data.

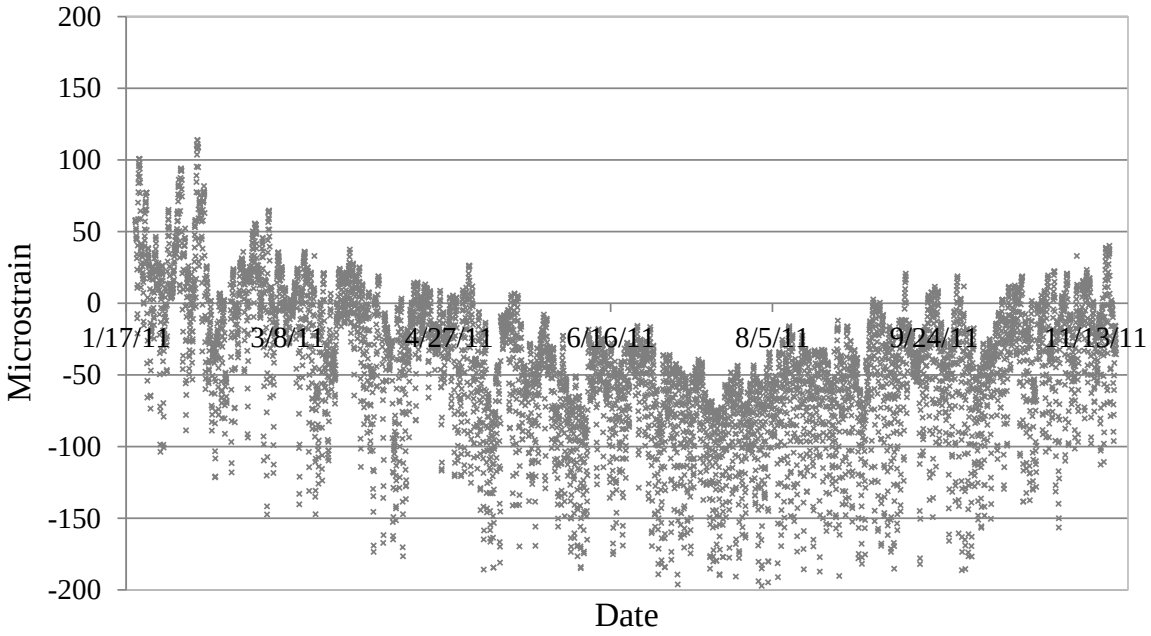

Figure 6.6. Bottom flange east strain gauge reading

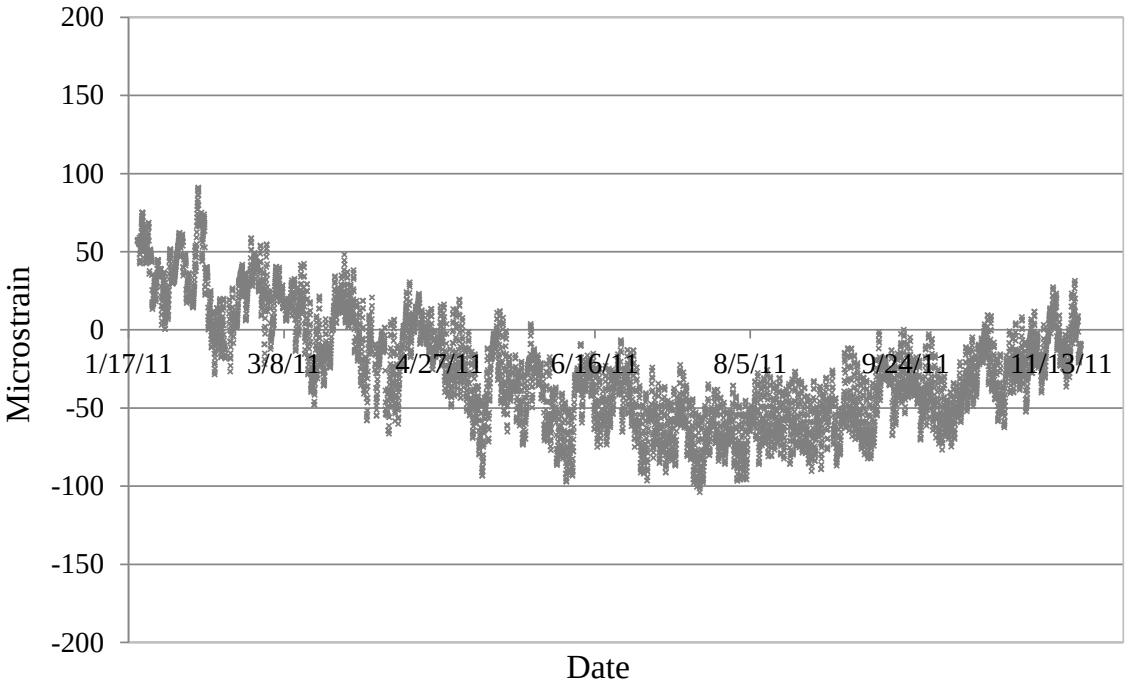

Figure 6.7. Top flange east strain gauge reading

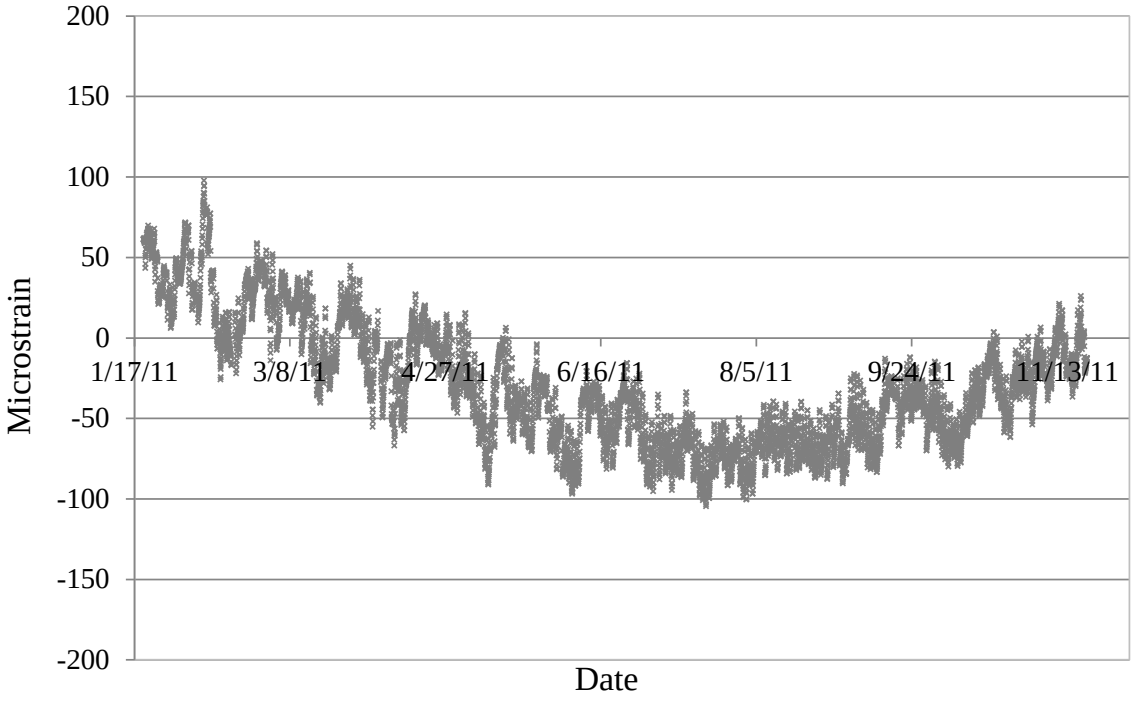

Figure 6.8. Top flange west strain gauge reading

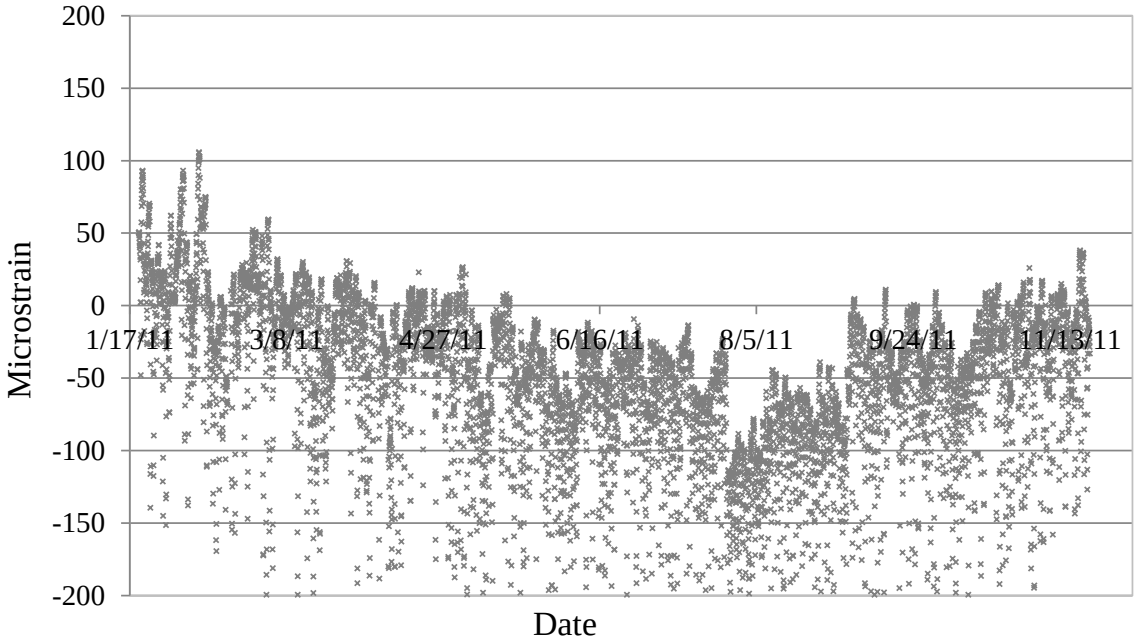

Figure 6.9. Bottom flange west strain gauge reading

Typical Girder Strains vs. Time

Figure 6.10 though Figure 6.13 show the internal girder strain measurements versus time for the four calculated strains at the center span of Girder D of Bridge 309. Figure 6.10 shows internal axial strain versus time, Figure 6.11 shows strong axis bending strain versus time, Figure 6.12 shows top flange lateral bending versus time, and Figure 6.13 shows bottom flange lateral bending versus time. In each figure, the light grey data shows the strain from the life of the project and the black data with white highlights shows the daily strain cycle from specific days of the project. The data denoted by squares represent a low temperature day, the data denoted by circles represent a moderate temperature day, and the data denoted by the triangles represent a high temperature day.

Figure 6.9 through 6.13 show a daily and annual cycle when compared with the date. The annual cycle range is larger than the daily cycle range for axial strain. In the case of major axis bending and lateral flange bending in both the top and bottom flanges the daily cycle range is comparable to the annual cycle range.

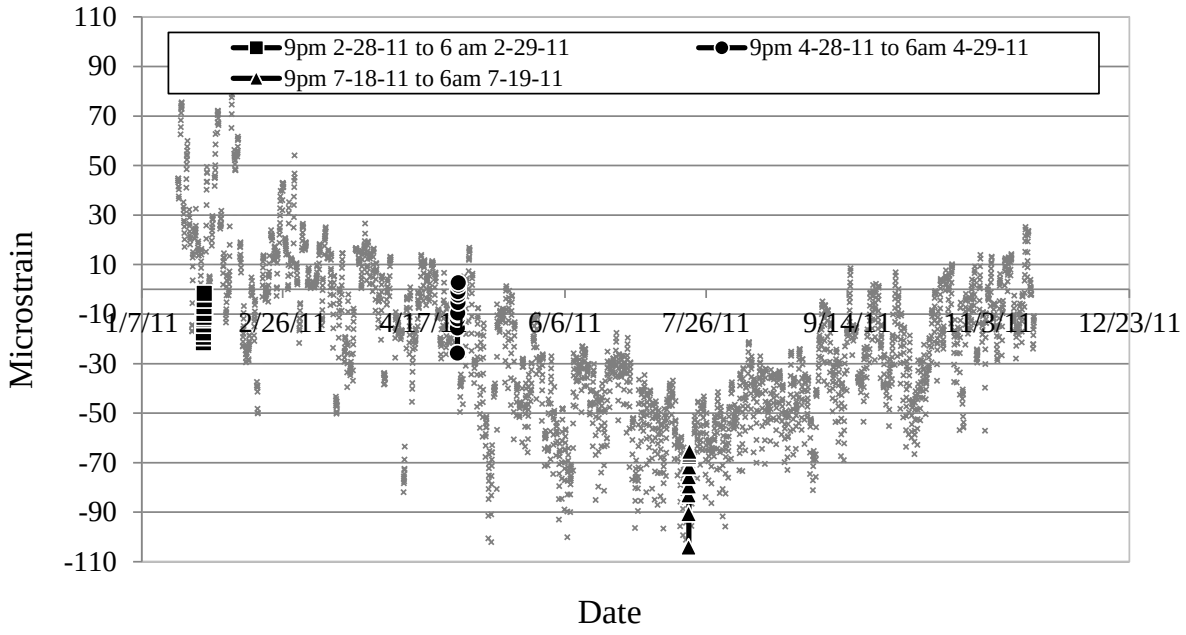

Figure 6.10. Axial strain vs. time

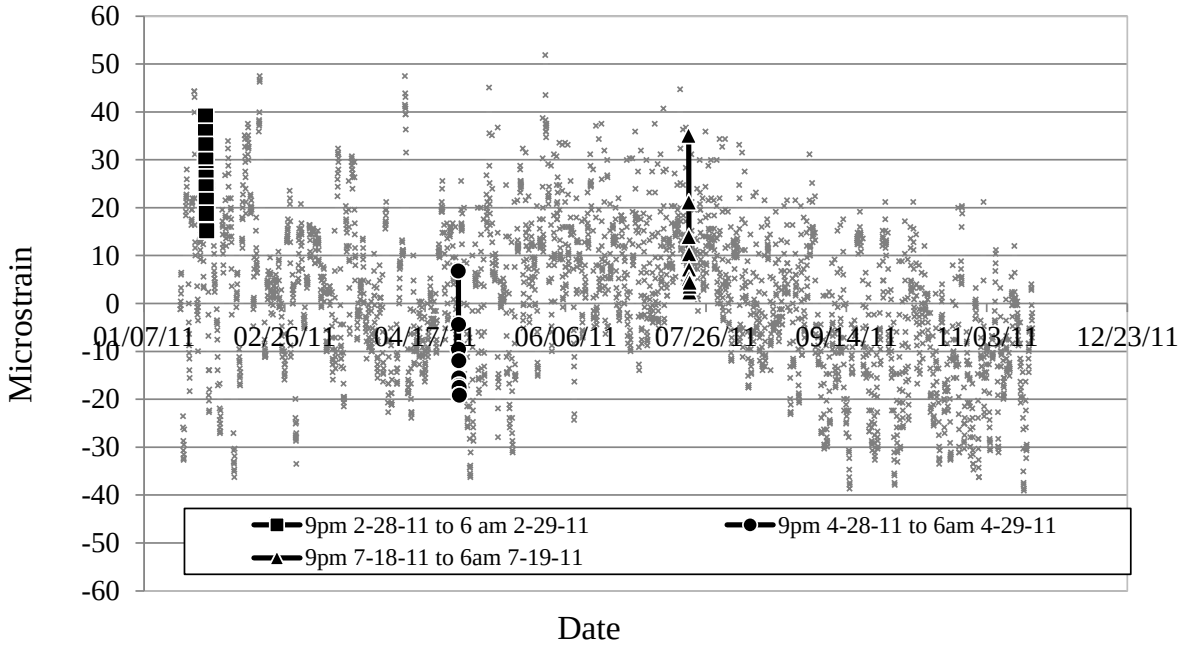

Figure 6.11. Major axis bending vs. time

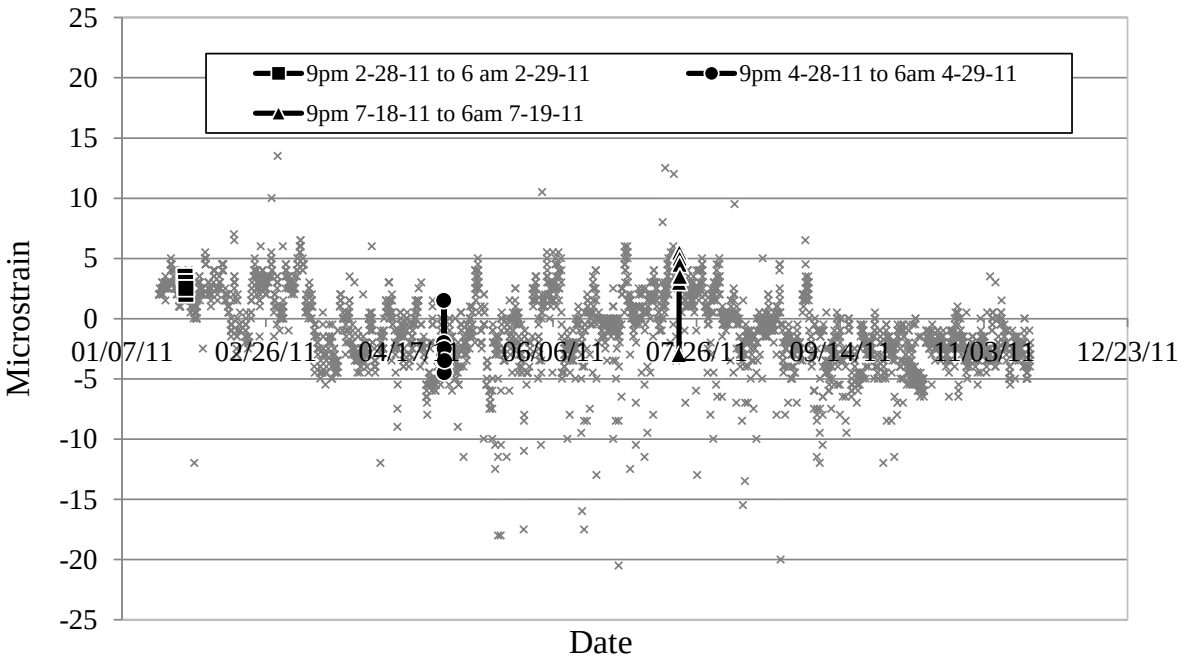

Figure 6.12. Top flange lateral bending vs. time

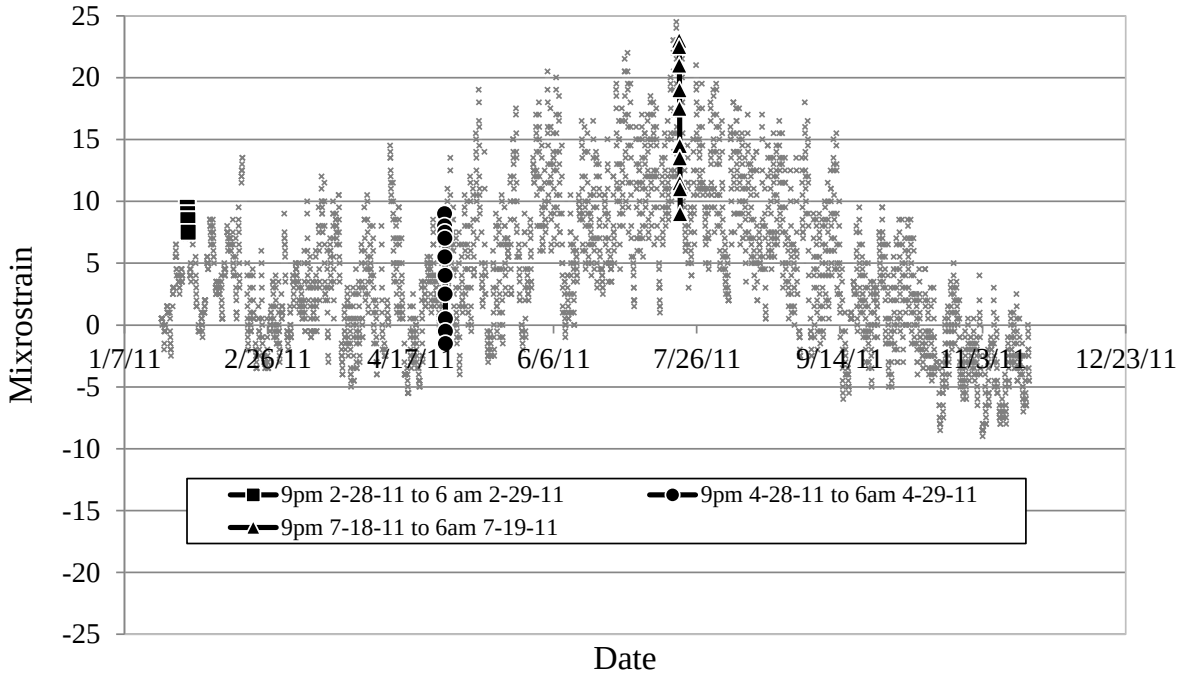

Figure 6.13. Bottom flange lateral bending vs. time

Typical Girder Strains vs. Teff

Figure 6.14 though Figure 6.17 show the internal girder strain measurements versus the effective bridge temperature for the four calculated strains at the center span of Girder D of Bridge 309. Figure 6.14 shows internal axial strain versus effective bridge temperature, Figure 6.15 shows strong axis bending strain versus effective bridge temperature, Figure 6.16 shows top flange lateral bending versus effective bridge temperature, and Figure 6.17 shows bottom flange lateral bending versus effective bridge temperature. In each figure, the light grey data shows the strain for the entire effective bridge temperature range, and the black data with white highlights shows the strain for an effective bridge temperature for single days. As with the previous figures, the data denoted by squares represent a low temperature day, the data denoted by circles represent a moderate temperature day, and the data denoted by the triangles represent a high temperature day.

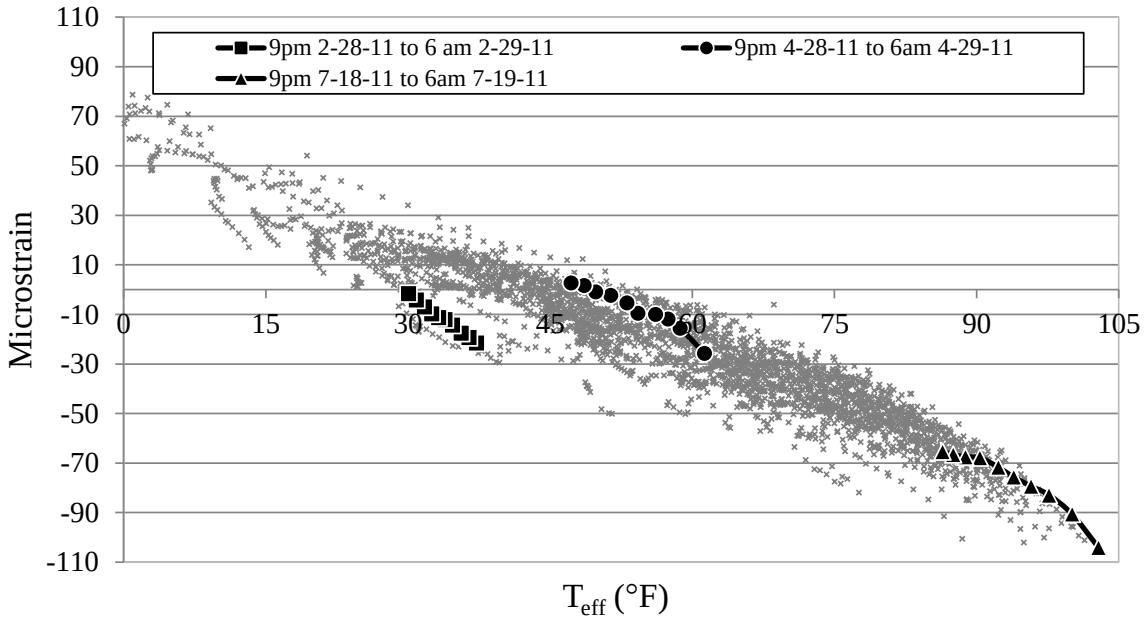

Figure 6.14. Axial strain vs. T_{eff}

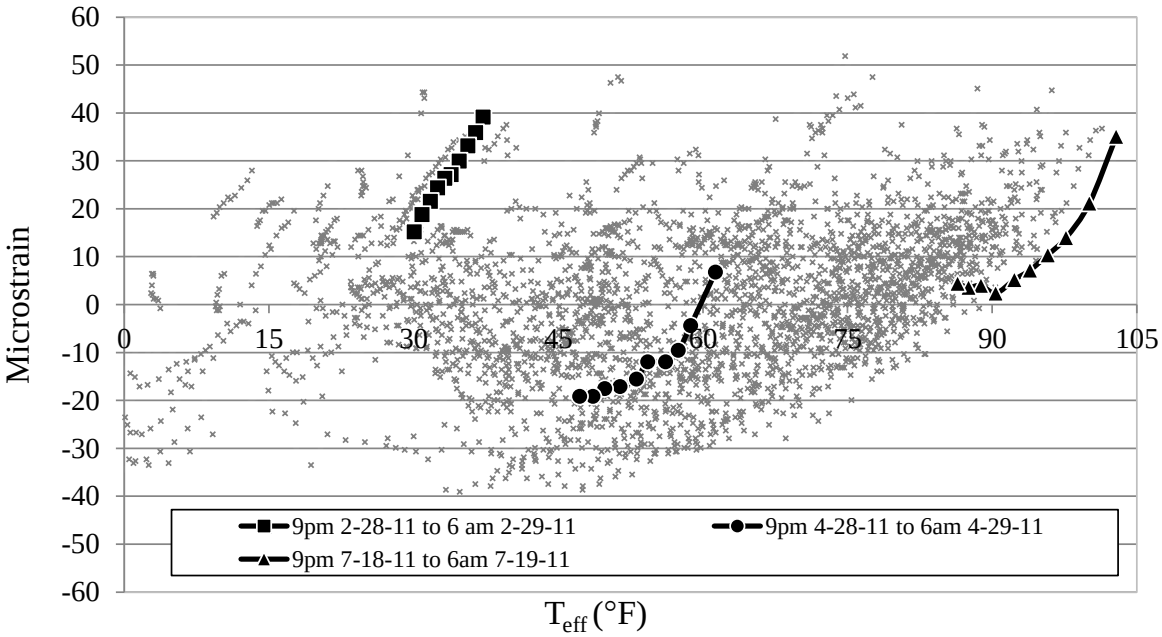

Figure 6.15. Major axis bending vs. T_{eff}

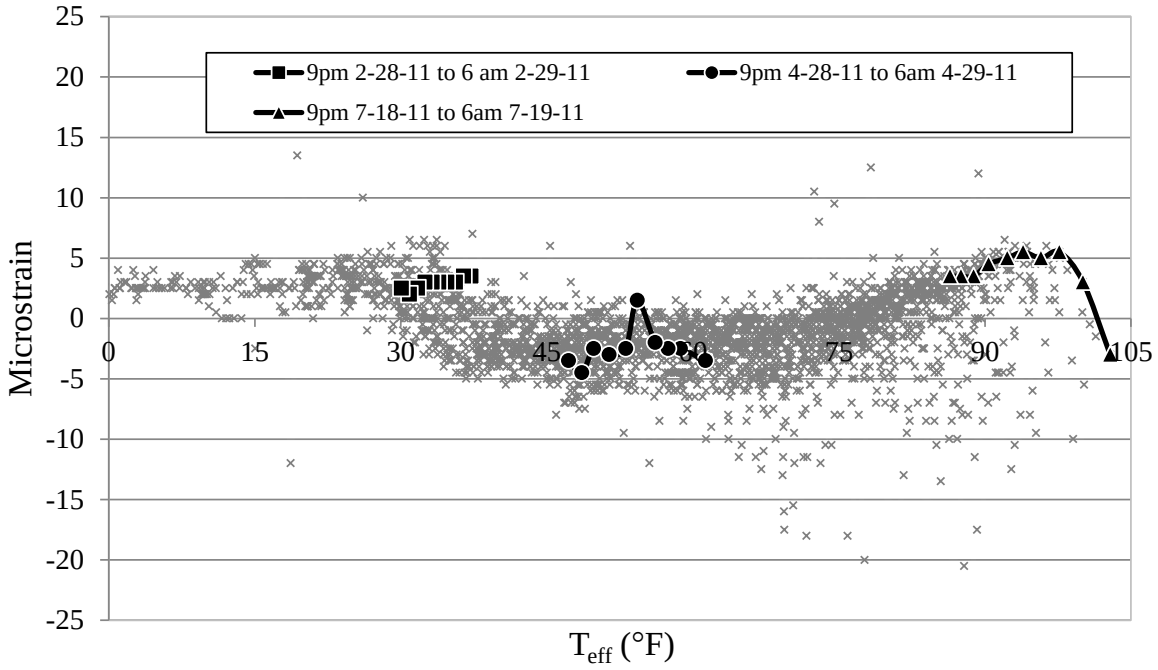

Figure 6.16. Top flange lateral bending vs. T_{eff}

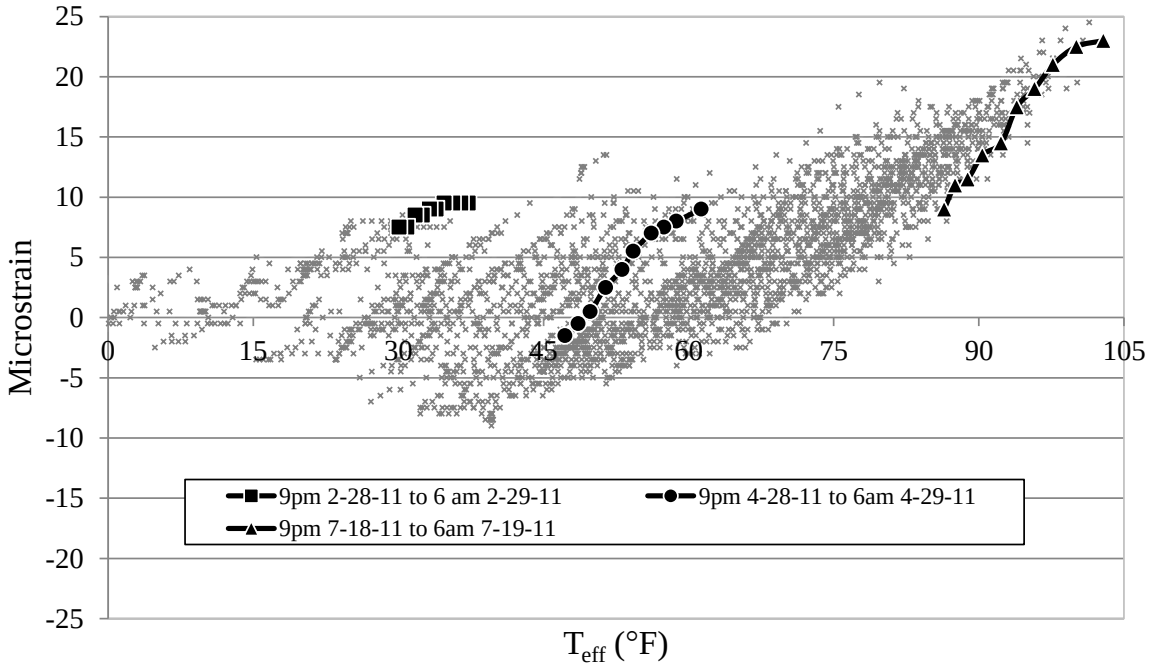

Figure 6.17. Bottom flange lateral bending vs. T_{eff}

Each of the internal strains have different relationships with temperature. Axial strain exhibits a generally linear relationship with the daily and annual effective bridge temperature

cycles, and the daily range for axial strain is small compared to the annual range for axial strain. The relationship between strong axis bending strain and the annual effective temperature cycle is very difficult to describe. However, the daily range for strong axis bending strain is comparable to the annual range and displays a consistent, non-linear, relationship. Top and bottom flange lateral bending strain display a smaller daily and annual strain range compared to axial and strong axis bending strains. Top flange lateral bending strain is consistently between 5 and -5 microstrain but with no obvious relationship with temperature. Bottom flange lateral bending strain shows a somewhat linearal relationship with daily effective temperature cycles, the range of which is proportion to annual effective temperature cycles.

Girder Strain and Force Range

For further data analysis, the research team determined a strain range experienced at each location over an equivalent temperature change. Over the course of a year, each location experiences a change in T_{eff} of approximately 100 °F. For each strain type the range was determined similar to the results displayed in Figure 6.18. In this way, the dashed lines represent the strain range over an annual effective temperature cycle. Note that this process was completed with some level of judgment involved and in many cases the upper and lower bounds did not necessarily capture all data points.

Once the strain range for each internal strain was determined, the ranges were tabulated and summarized based on strain type, bridge, and span location. Table 6.1 shows the values collected for outside girder, Girder A, for each bridge. Table 6.2 shows the values collected for the inside girder, Girder D, for each bridge. All values displayed are in microstrain.

Once the internal strain ranges were tabulated the internal force ranges were calculated by substituting values from Table 6.1 and Table 6.2 into equations 6.16–6.19. Table 6.3 and Table 6.4 display the calculated values based on force type, bridge, and span location, for their respective girder.

After the internal strain and force ranges were tabulated, the values were represented alongside their respective locations on representations of the bridges. For ease of interpretation Bridge 309 and Bridge 2308 were placed on the same graphic and Bridge 209 and Bridge 2208 were similarly compared due to their similar geometries. From the

illustration, the research team made observations about the nature of the results with respect to bridge configuration.

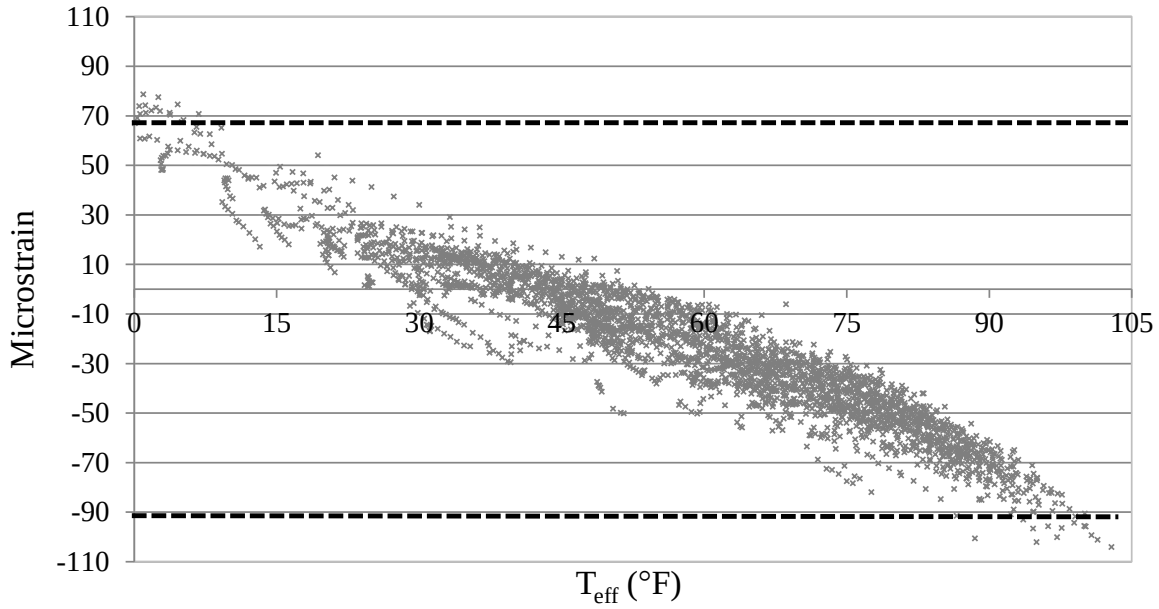

Figure 6.18. Strain range calculation – axial strain example

Table 6.1. Strain Range Girder A

	Bridge #	S span	C span	N span	Avg.
$\varepsilon_a = P/(AE)_{eff}$	**109**	NA	180	NA	180
	209	150	155	150	152
	309	170	160	170	167
	2208	70	85	120	92
	2308	130	150	80	120
$\varepsilon_x = M_x y_3/(EI_x)_{eff}$	**109**	NA	70	NA	70
	209	80	80	80	80
	309	50	40	50	47
	2208	110	80	100	97
	2308	60	60	100	73
$\varepsilon_{lt} = M_{lt}x_1/E_sI_{yt}$	**109**	NA	60	NA	60
	209	100	25	25	50
	309	20	15	15	17
	2208	10	40	NA	25
	2308	40	10	60	37
$\varepsilon_{lb} = M_{lb}x_3/E_sI_{yb}$	**109**	NA	NA	NA	NA
	209	NA	20	NA	20
	309	NA	NA	15	15
	2208	20	NA	20	20

	Bridge #	S span	C span	N span	Avg.
	2308	30	10	NA	20

Table 6.2. Strain range Girder D

	Bridge #	S span	C span	N span	Avg.
$\varepsilon_a = P/(AE)_{eff}$	**109**	NA	180	NA	180
	209	180	200	180	187
	309	130	180	180	163
	2208	140	120	80	113
	2308	190	220	140	183
$\varepsilon_x = M_x y_3/(EI_x)_{eff}$	**109**	NA	70	NA	70
	209	110	20	90	73
	309	80	70	80	77
	2208	90	70	80	80
	2308	60	100	35	65
$\varepsilon_{lt} = M_{lt}x_1/E_sI_{yt}$	**109**	NA	40	NA	40
	209	10	50	20	27
	309	30	10	40	27
	2208	15	10	20	15
	2308	15	20	70	35
$\varepsilon_{lb} = M_{lb}x_3/E_sI_{yb}$	**109**	NA	10	NA	10
	209	30	35	10	25
	309	15	30	25	23
	2208	120	NA	15	68
	2308	NA	90	60	75

Table 6.3. Force Range Girder A

	Bridge #	S span	C span	N span	Average
$P = \varepsilon_a(AE)_{eff}$	**109**	NA	666	NA	666
	209	610	618	611	613
	309	685	668	686	680
	2208	285	339	489	371
	2308	500	598	308	469
$M_x = \varepsilon_x(EI_x)_{eff}/y_3$	**109**	NA	2580	NA	2580
	209	3070	3630	3070	3260
	309	2060	2100	2060	2070
	2208	4220	3630	3840	3900
	2308	2290	2750	3820	2950
$M_{lt} = \varepsilon_{lt}E_sI_{yt}/x_1$	**109**	NA	64	NA	64
	209	257	33	64	118
	309	43	28	32	34
	2208	26	53	NA	39
	2308	62	13	93	56
$M_{lb} = \varepsilon_{lb}E_sI_{yb}/x_3$	**109**	NA	NA	NA	NA
	209	NA	64	NA	64
	309	NA	NA	32	32
	2208	52	NA	52	51

	Bridge #	S span	C span	N span	Average
	2308	53	24	NA	39

Table 6.4. Force range Girder D

	Bridge #	S span	C span	N span	Average
$P = \varepsilon_a(AE)_{eff}$	109	NA	666	NA	666
	209	712	768	712	731
	309	501	717	693	637
	2208	554	461	317	444
	2308	700	823	516	680
$M_x = \varepsilon_x(EI_x)_{eff}/y_3$	109	NA	2580	NA	4030
	209	3930	776	3220	2640
	309	3050	3370	3050	3160
	2208	3220	2720	2860	2930
	2308	1930	3810	1130	2290
$M_{lt} = \varepsilon_{lt}E_sI_{yt}/x_1$	109	NA	42	NA	42
	209	22	66	43	44
	309	46	13	62	40
	2208	32	13	43	29
	2308	19	21	87	42
$M_{lb} = \varepsilon_{lb}E_sI_{yb}/x_2$	109	NA	12	NA	12
	209	64	85	22	57.
	309	26	73	44	48
	2208	258	NA	32	145
	2308	NA	143	74	109

Figure 6.19 through Figure 6.30 display the internal strains for the four curved and the one straight bridge that has electronic instrumentation mounted to their girder flanges. In the figures, north is to the right with respect to Bridge 309 and Bridge 209. North is to the left with respect to Bridge 2308 and Bridge 2208. All values are in microstrain.

Figures 6.19 through 6.21 show the measured internal axial strains, ε_a, for each of the five bridges. The results for each of the measured locations are roughly the same (150—170 με). The strain values are somewhat larger for semi-integral abutments and the center span strain is somewhat greater when between two fixed piers.

Figure 6.22 through 6.24 show the measured internal strong axis bending strains, ε_x, for each of the five bridges. The results for most measured locations all fall in the range of 60 to 90 microstrain. The measured results at the center span of the horizontally curved bridges are typically very close to the measured results at the center span of the straight bridge.

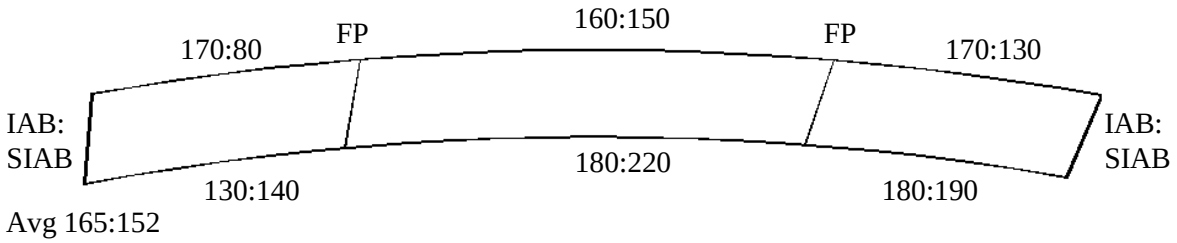

Figure 6.19. Axial strain range Bridge 309:2308

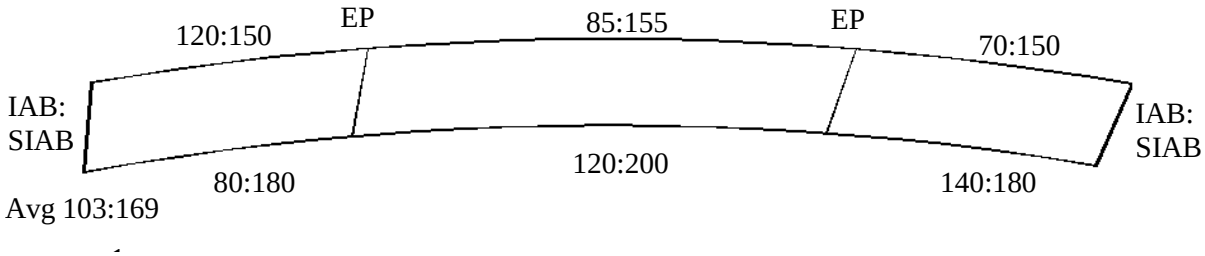

Figure 6.20. Axial strain range Bridge 209:2208

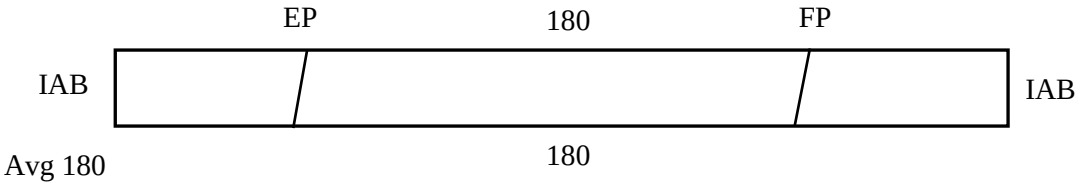

Figure 6.21. Axial strain range Bridge 109

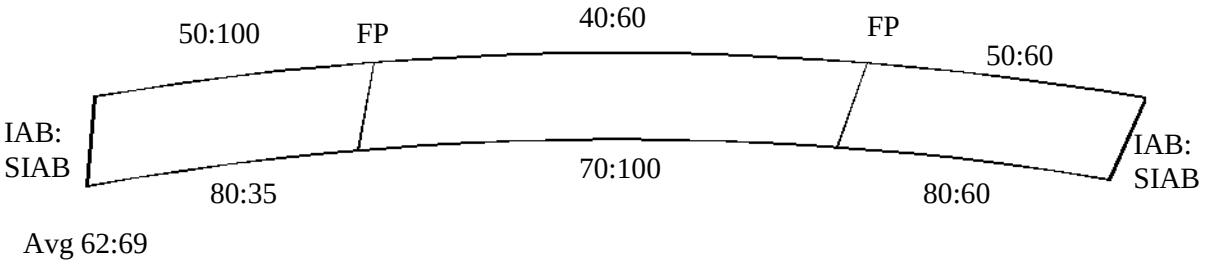

Figure 6.22. Strong axis bending strain range Bridge 309:2308

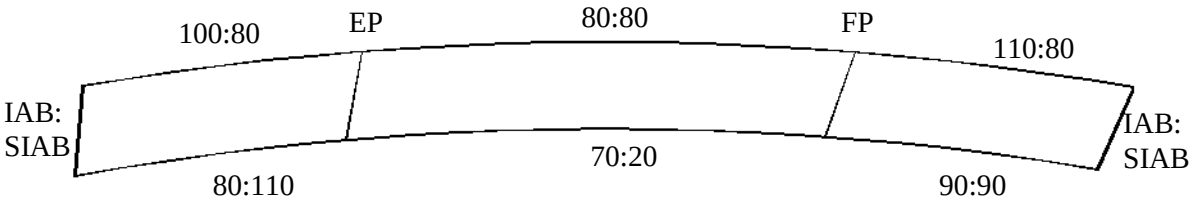

Figure 6.23. Strong axis bending strain range Bridge 209:2208

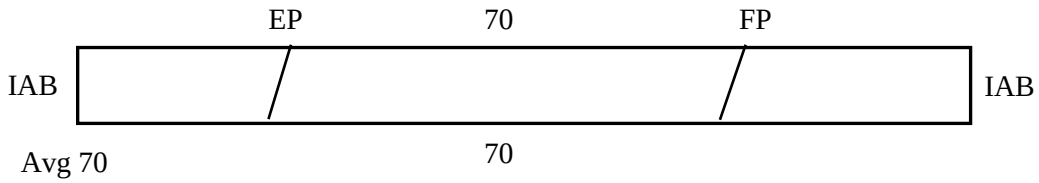

Figure 6.24. Strong axis bending strain range Bridge 109

Figure 6.25 through 6.27 show the measured internal top flange lateral bending strain, ε_{lt}, for each of the five bridges. The results from the measured values are all roughly equivalent (20—30 με), with some outliers. There are no notable differences with respect to bridge radius or skew, and the results from the straight bridge are only slightly higher than the results from the horizontally curved bridges.

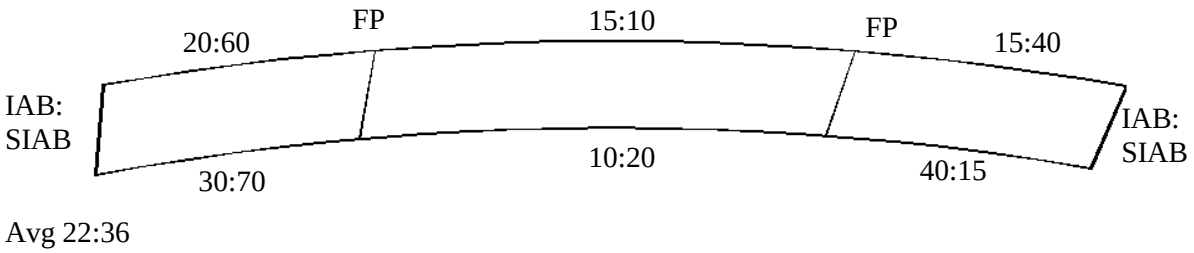

Figure 6.25. Lateral bending strain top flange range Bridge 309:2308

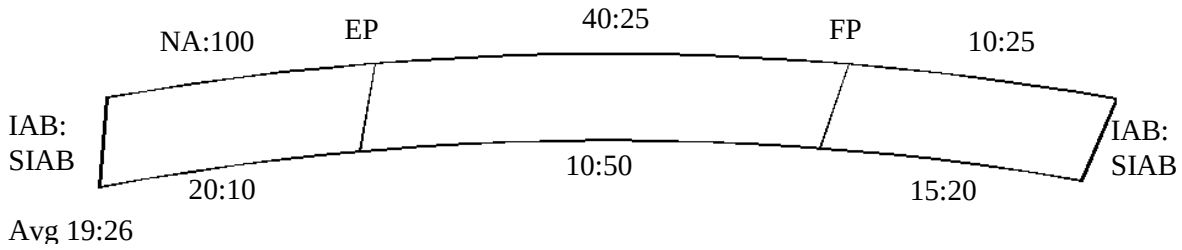

Figure 6.26. Lateral bending strain top flange Bridge 209:2208

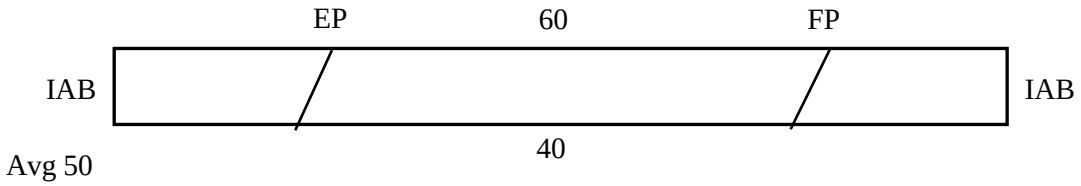

Figure 6.27. Lateral bending strain top flange Bridge 109

Figure 6.28 through 6.30 show the measured internal bottom flange lateral bending strain, ε_{lb}, for each of the five bridges. The results from the measured values are similar to the results of top flange lateral bending strain; typically around 20 to 30 με. As with top flange lateral bending, there are no notable differences between the straight and curved bridges and no notable difference with respect to bridge radius or skew.

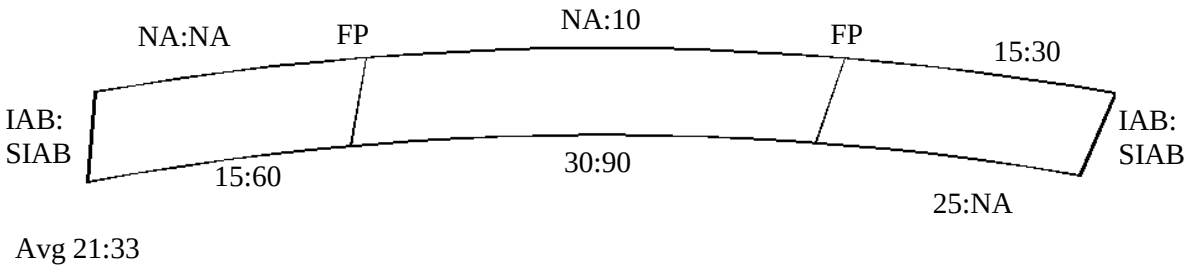

Figure 6.28. Lateral bending strain bottom flange Bridge 309:2308

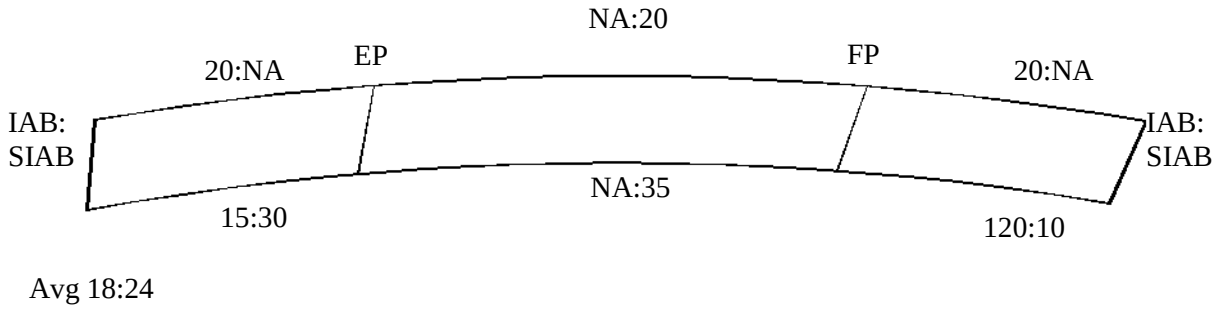

Figure 6.29. Lateral bending strain bottom flange Bridge 209:2208

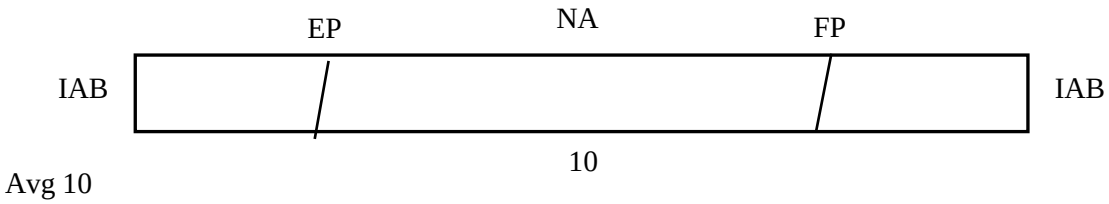

Figure 6.30. Lateral bending strain bottom flange Bridge 109

Figure 6.31 through 6.42 show the calculated internal forces for the four curved and the one straight bridge that had strain gauge instrumentation on their girders. As with the internal strain figures, north is to the right with respect to Bridge 309 and Bridge 209, and north is to the left with respect to Bridge 2308 and Bridge 2208.

Figure 6.31 through 6.33 show the internal axial force, *P*, for each of the five bridges. The results for the inside girder of bridge 109, the straight bridge, is lower than Bridge 309, 209 and 2308; and is higher than the results for the inside girder of Bridge 2208. The outside girder for Bridge 109 is close to Bridge 209, 309, and 2308; and is higher than the outside girder of Bridge 2208. All values in the figures are in kip.

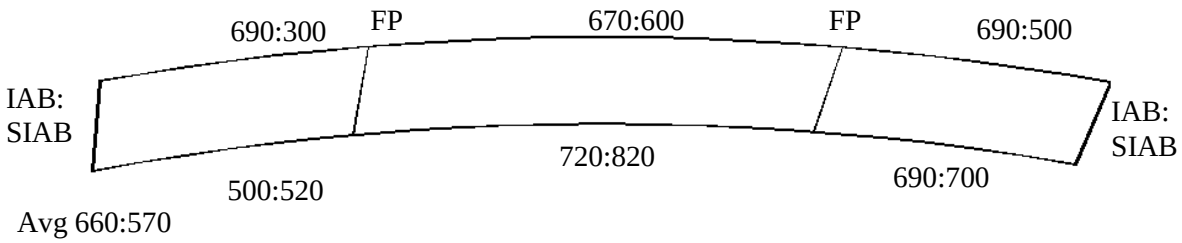

Figure 6.31. Axial force range Bridge 309:2308

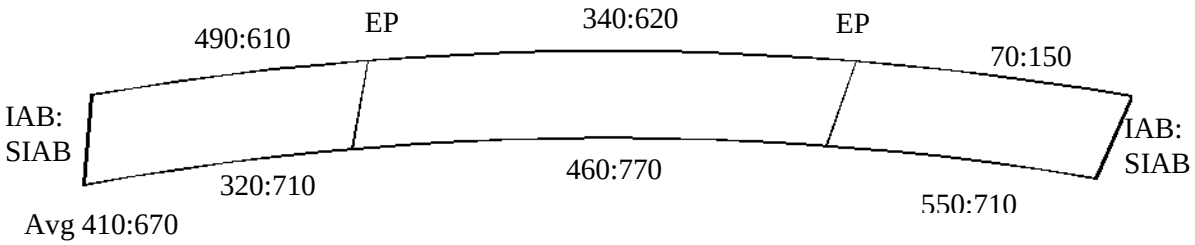

Figure 6.32. Axial force range Bridge 209:2208

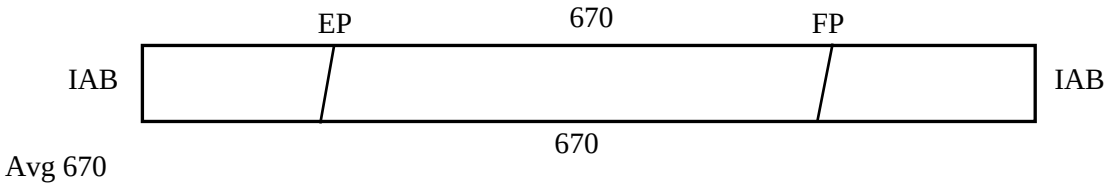

Figure 6.33. Axial force range Bridge 109

Figure 6.34 through 6.36 show the internal strong axis bending moment, M_x, for each of the five bridges. With the exception of one span, the values at the center span of Bridge 309 and Bridge 2308, between two fixed piers, are higher than the center span values of the other bridges. The inside girder results of Bridge 109 are lower than the inside girder results of Bridge 309 and Bridge 2308 and are similar to the results of the inside girder results of Bridge 209 and Bridge 2208. The outside girder results are lower than the outside girder results of Bridge 209 and Bridge 2208, and are similar to the outside girder results of Bridge 309 and Bridge 2308. All values in the figures are in kip-in.

Figure 6.37 through 6.42 shows the results of internal lateral flange bending moment in the top and bottom flanges. Since a number of gauges malfunctioned and their data had to be ignored, the results of lateral flange bending in both the top and bottom flanges were incomplete for all the bridges, which makes it hard to draw any solid conclusion. However, typically the results were larger in the bottom flanges, and the lateral flange bending moment was smaller in Bridge 109, the straight bridge, than in any of the horizontally curved bridges. All values in the figures are in kip-in.

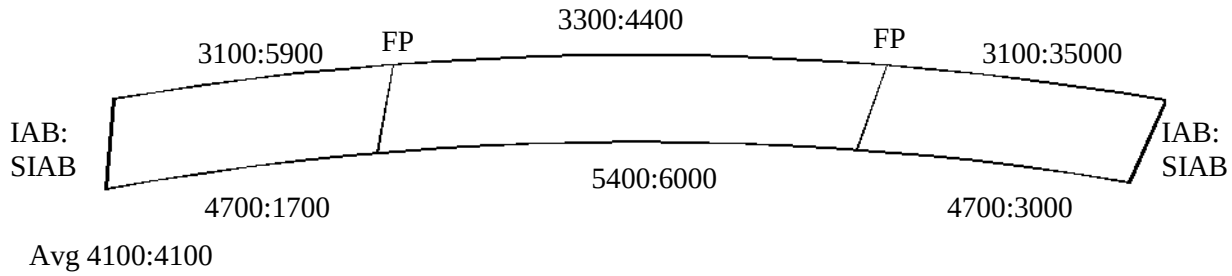

Figure 6.34. Strong axis moment range Bridge 309:2308

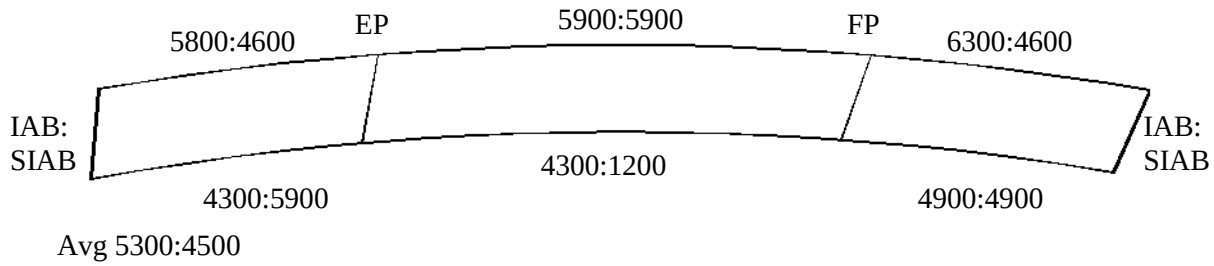

Figure 6.35. Strong axis moment range Bridge 209:2208

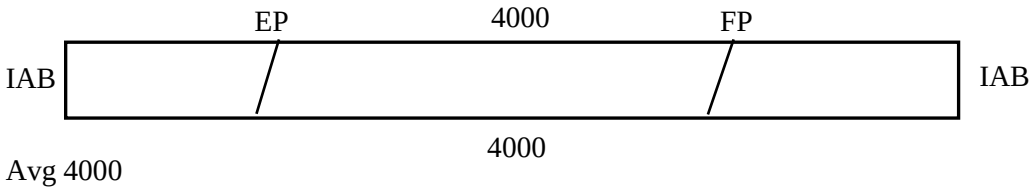

Figure 6.36. Strong axis bending moment range Bridge 109

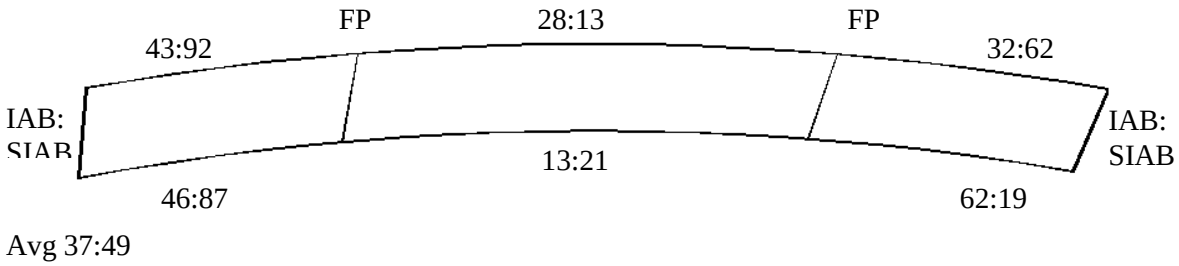

Figure 6.37. Lateral bending moment top flange range Bridge 309:2308

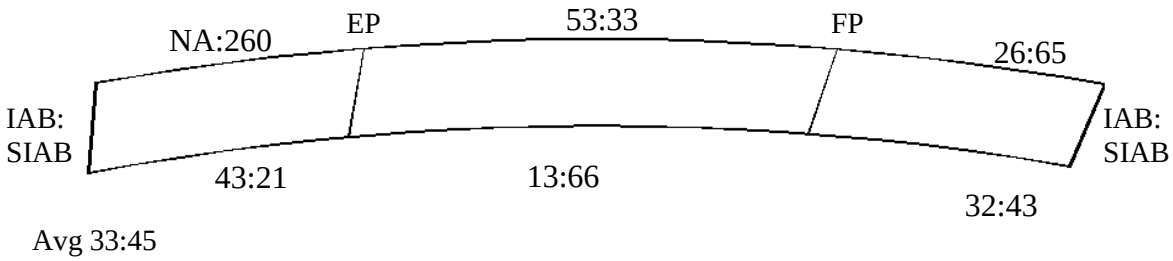

Figure 6.38. Lateral bending moment top flange Bridge 209:2208

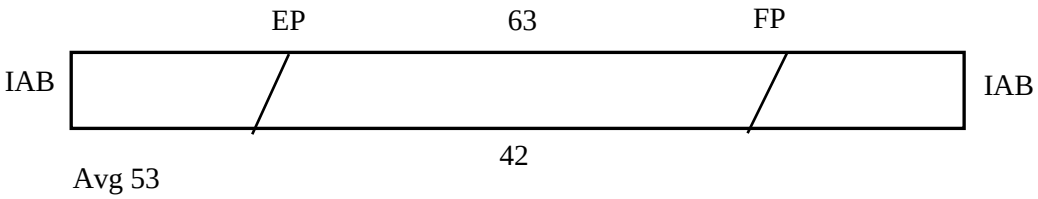

Figure 6.39. Lateral bending moment top flange Bridge 109

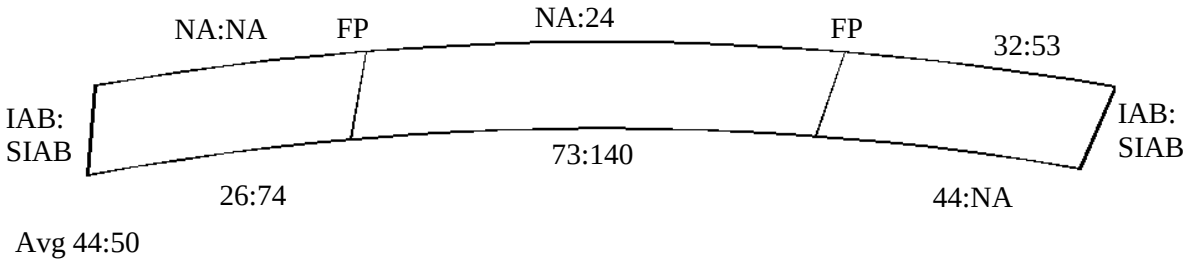

Figure 6.40. Lateral bending strain bottom flange Bridge 309:2308

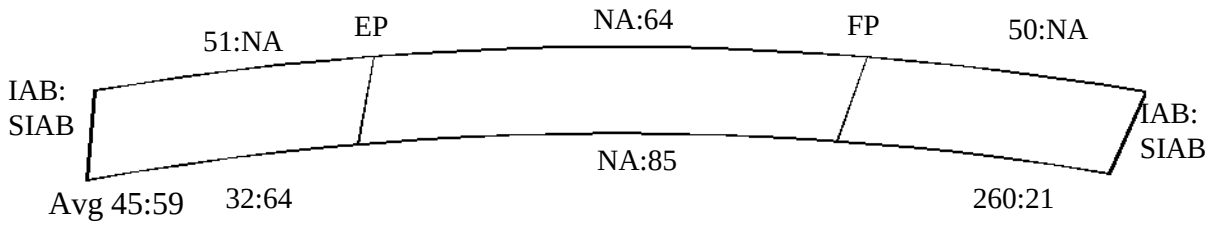

Figure 6.41. Lateral bending strain bottom flange Bridge 209:2208

Figure 6.42. Lateral bending strain bottom flange Bridge 109

6.2.2 Substructure

Pile Resolved Strains

There are six piles cast into each abutment pile cap of Bridge 309. At the north abutment, the west most pile, outside the curve, was labeled NAHP1, and the labeling continued east with the east most pile, inside the curve, labeled NAHP6. At the south abutment, the west most pile, outside the curve, was labeled SAHP1, and the labeling continued east with the east most pile, inside the curve, labeled SAHP6. At each abutment of Bridge 309 piles HP1, HP4, and HP6 were instrumented with strain-gauges, the results of which are discussed in this section.

As discussed previously, the coordinate system for each set of piling was established so that the positive X-axis was in the direction of outward expansion and the positive Y-axis was 90 degrees counter-clockwise from the X-axis. In both the north and south abutment piles, positive minor axis bending caused tension in the outside flange. The positive direction of the other strains was different between each abutment and was controlled by the equations used to calculate the strains. Figure 6.43(a) shows the pile coordinate system and the resultant strains of the south abutment piles. Figure 6.43(b) shows the pile coordinate system and the resultant strains of the north abutment piles.

Using the sign conventions shown in Figure 6.43, the total internal strain at all four gage locations were used to calculate the four resultant strains in the south abutment instrumented piles. Equations 6.20 through 6.23 are the necessary equations to determine the resultant strains. Equation 6.22.1 was used to determine the weak axis bending strain in the south abutment piles while Equation 6.22.2 was used to determine the weak axis bending strain in the north abutment piles. The rest of the equations are relevant for the piles at either abutment.

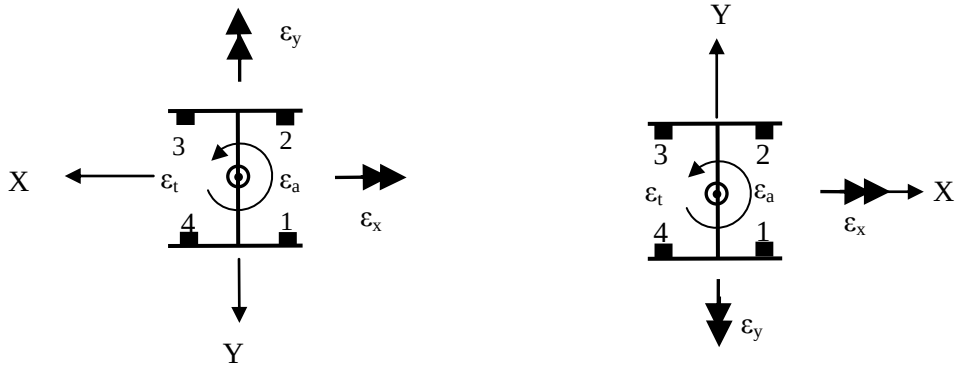

(a) south abutment (b) north abutment

Figure 6.43. Abutment pile internal forces

$$\Delta\varepsilon_a = \tfrac{1}{4}(\varepsilon_1+\varepsilon_2+\varepsilon_3+\varepsilon_4) \quad (6.20)$$

$$\Delta\varepsilon_x = \tfrac{1}{4}(-\varepsilon_1+\varepsilon_2+\varepsilon_3-\varepsilon_4) \quad (6.21)$$

$$\Delta\varepsilon_y = \tfrac{1}{4}(\varepsilon_1+\varepsilon_2-\varepsilon_3-\varepsilon_4) \quad (6.22.1)$$

$$\Delta\varepsilon_y = \tfrac{1}{4}(-\varepsilon_1-\varepsilon_2+\varepsilon_3+\varepsilon_4) \quad (6.22.2)$$

$$\Delta\varepsilon_t = \tfrac{1}{4}(-\varepsilon_1+\varepsilon_2-\varepsilon_3+\varepsilon_4) \quad (6.23)$$

where,

ε_a = internal axial strain,

ε_x = internal strong axis bending strain,

ε_y = internal weak axis bending strain, and

ε_t = internal torsional-warping strain.

Figures 6.44 through 6.47 show the typical results of internal strains versus effective bridge temperature. These results are from HP1 of the north abutment. The gray, background data in the figures are the total data over the length of the monitoring period. Three separate days of data are also displayed in the figures, separate from the total data. January 28th, 2011, a cold day, is represented by triangles; April 28th, 2011, a moderate day, is represented by

circles; and July 19th, 2011, a hot day, is represented by squares.

Figure 6.44 shows the typical internal axial strain in the piles. A solid description of a relationship between axial strain and effective temperature is hard to produce. The range due to the annual effective temperature cycle is large compared to the strain range due to the daily effective temperature cycle. Internal axial strain is small compared to strong axis bending and weak axis bending strain but is large compared to torsional-warping strain.

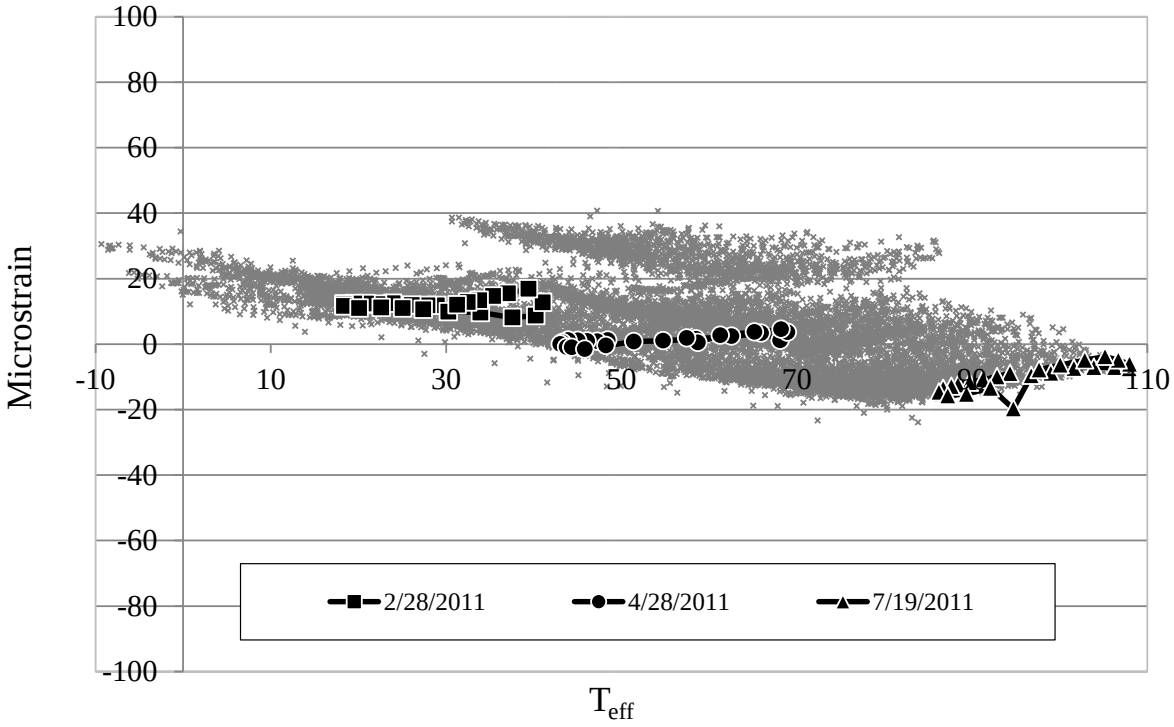

Figure 6.44. Typical internal axial strain

Figure 6.45 shows the typical internal strong axis bending strain in the piles. The results show a strong linear relationship with effective bridge temperature. The range due to the annual effective temperature cycle is larger compared to the strain range due to the daily effective temperature cycle. The resulting strong axis bending strain range is larger than the internal axial strain and torsional-warping strain range but is small compared to the minor axis bending strain.

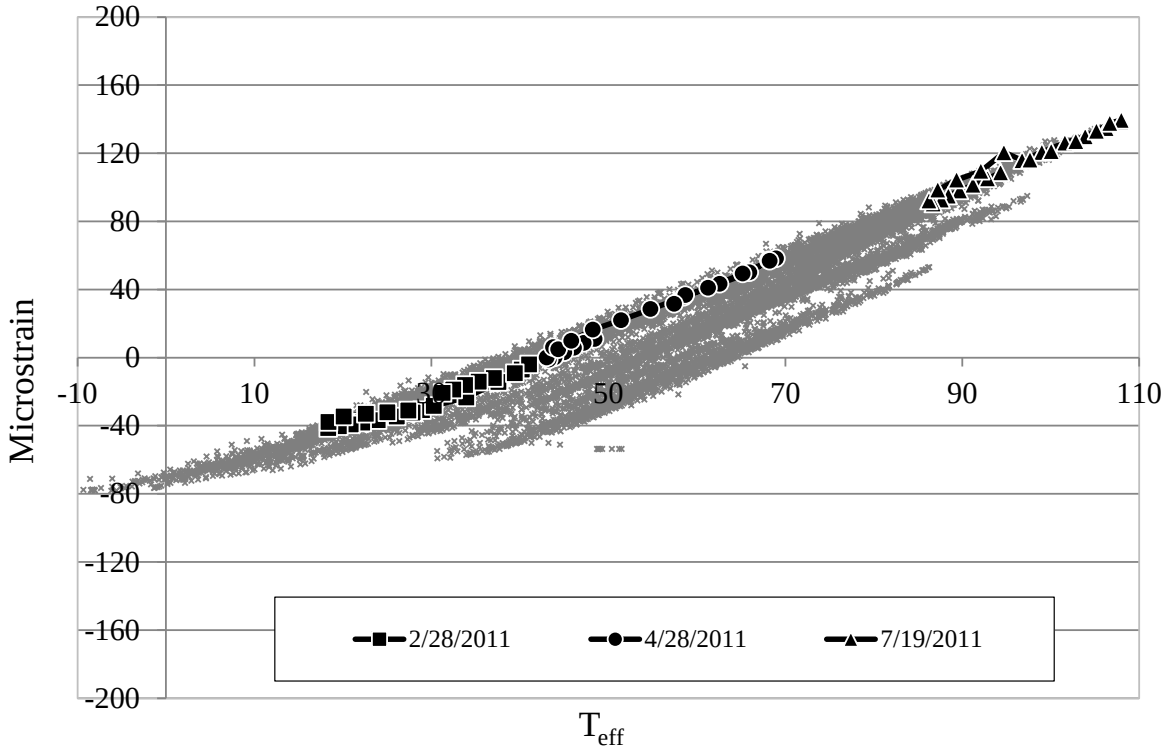

Figure 6.45. Typical internal major axis bending strain

Figure 6.46 shows the typical internal weak axis bending strain in the piles. As expected, the weak axis bending strain range is much large than the range of any other measured internal strain. The results show a strong linear relationship with effective bridge temperature. The range due to the annual effective temperature cycle is large compared to the strain range due to the daily effective temperature cycle.

Figure 6.47 shows the typical internal torsional-warping strain in the piles. Typically the data tends to hover around a value of zero microstrain. There is no solid relationship between the strain and the effective bridge temperature, and the ranges due to the annual effective temperature cycle and the daily effective temperature cycle are both minimal.

As was done with the measured internal girder strain, the measured internal strain ranges at each instrumented pile location were found and tabulated for comparison. Table 6.5 shows the measured pile internal strain ranges.

Table 6.5. Measured pile internal strain ranges

Pile/Strain	NH1	NH4	NH6	SH1	SH4	SH6
$\varepsilon_a(\mu\varepsilon)$	60	90	60	120	90	80
$\varepsilon_x(\mu\varepsilon)$	220	240	240	140	160	190
$\varepsilon_y(\mu\varepsilon)$	900	800	590	810	710	700
$\varepsilon_t(\mu\varepsilon)$	45	60	30	NA	NA	20

The internal weak axis bending strain showed larger ranges than the other three strains in all six monitored piles with an average of 751 microstrain. The internal strong axis bending strain showed the next largest strain ranges in all six monitored piles with an average of 198 microstrain. The average internal axial strain range of all six piles was 83 microstrain. The smallest of all four strains was the torsional-warping strain with an average of 39 microstrain for the four piles with available results.

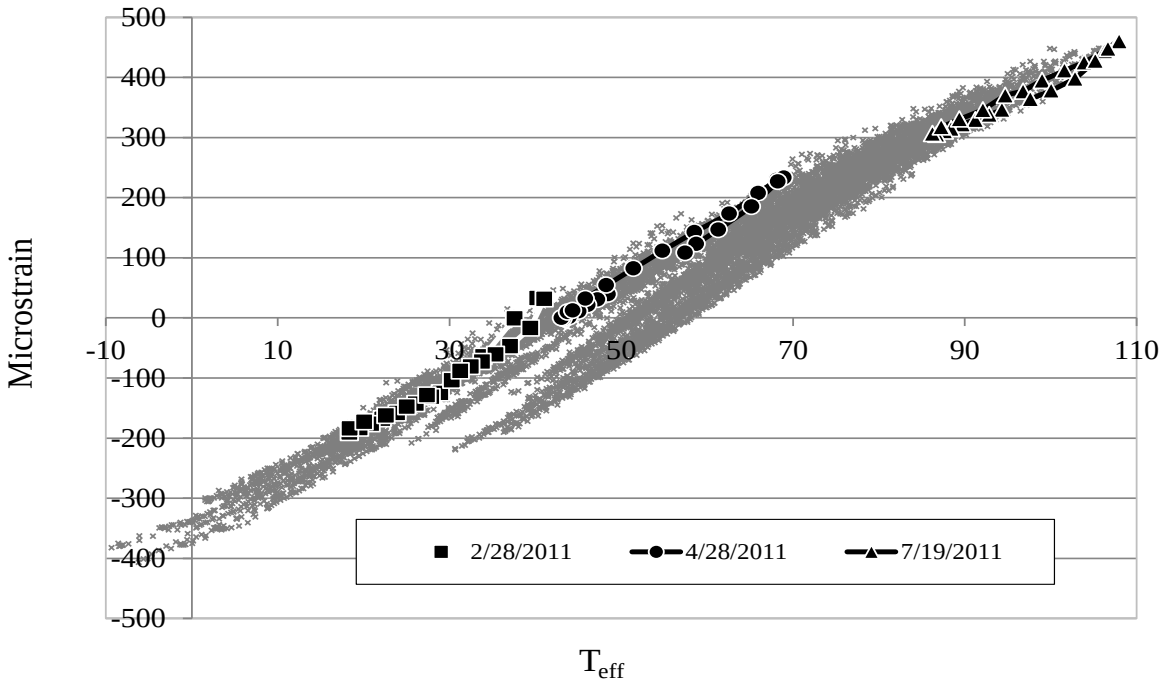

Figure 6.46. Typical internal minor axis bending strain

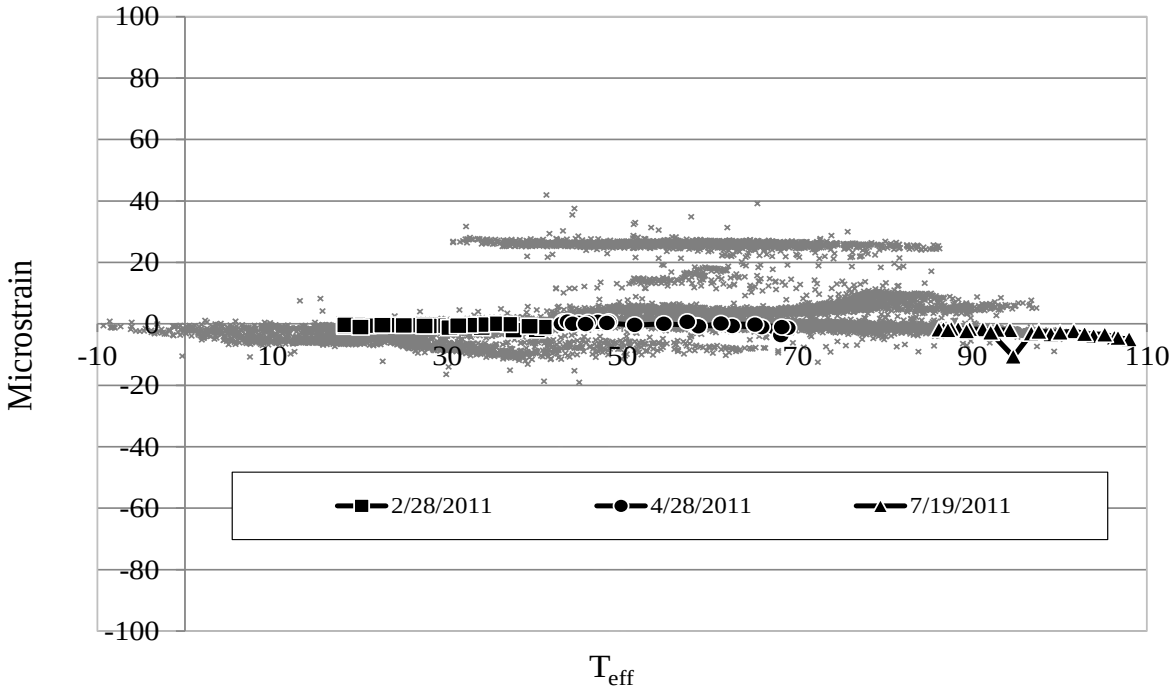

Figure 6.47. Typical internal torsional-warping strain

Using the cross-sectional properties of the HP 10x57 abutment piles and the measured pile internal strain range, the pile internal force ranges were calculated. Table 6.6 shows the calculated values. In the table axial load, P, strong axis bending, Mx, and weak axis bending, My, were calculated using familiar strength of materials equations. The lateral bending moment, Mf, is a lesser known quantity and was calculated using the following equation from Salmon, et al (2009):

$$\varepsilon_t = \frac{f_{bw}}{E_s} = \frac{M_f x}{I_f E_s} \tag{6.24}$$

where,

f_{bw} = tension or compression stress due to warping of the cross-section

E_s = modulus elasticity of the steel

M_f = lateral bending moment acting on the flanges

x = distance from center of flange to flange tip

I_f = moment of inertia of a flange about its smaller principal axis

Table 6.6. Calculated pile internal force ranges

Pile/Force	NH1	NH4	NH6	SH1	SH4	SH6
P(kips)	290	440	290	590	440	390
M_x(kip-in.)	380	410	410	240	270	320
M_y(kip-in.)	520	460	340	470	410	400
M_f(kip-in.)	12	16	8	NA	NA	5

As shown in Table 6.6, axial load in the South abutment is typically higher than axial load in the North abutment, although both abutments show similar values. Generally minor axis bending is larger than major axis bending in all instrumented piles in both the North and South abutments, and lateral flange bending, where data are available, is very small compared to all other measured forces.

Abutment Backwall Pressure

The soil pressure on the abutment backwalls of Bridge 309 increases as the bridge expands into the backfill soil. This condition is called passive soil pressure (Coduto 2001) and was measured by the pressure cells mounted to the abutment backwalls. If the soil conditions in the abutment backfill are known, the maximum passive soil pressures can be approximated using the following equations:

$$K_p = \frac{\sigma_x'}{\sigma_z'} \tag{6.25}$$

$$K_p = tan^2(45° + \phi'/2) \tag{6.26}$$

$$\sigma_z' = \gamma' Z \tag{6.27}$$

where,

Kp = the coefficient of passive lateral earth pressure (psi/psi),

σ_x' = effective horizontal stress (psi),

σ_z' = effective vertical stress (psi),

ϕ' = effective friction angle of the soil (degree)

γ' = buoyant unit weight of soil (lb/in.^{3}), and

Z = depth from top of soil to location of desired stress (in.)

By making a few assumptions on the backfill soil properties the research team was able to approximate the range of passive soil stress on the north and south abutments of Bridge 309. The approximation was calculated at the depth of the pressure cells. According to the bridge plan set, the backfill soil consists of A-6 soil type, a clayey soil with >35% passing the 0.075mm sieve (ASTM D3283). Considering the soil classification, the following assumptions were made following recommendations by Coduto 2011:

$\phi \approx 30°—40°$, and

$\gamma \approx 110—135$ pcf

By substituting the assumptions for ϕ and γ into Equation 6.25 through 6.27 the research team was able to calculate an approximate range between 10−19 psi for passive stress on the abutment backwalls at the depth of the pressure cells for Bridge 309.

Figures 6.48 through 6.51 show the external stress on the north and south abutment pressure cells attached to Bridge 309, respectively. As expected, the stresses increase as the temperature increases and drops to zero at lower temperatures. According to the figure, over the life of the monitoring period of the project the north abutment experience higher stresses. Also shown in the figure are the upper-bound and lower-bound approximations of passive pressure, denoted by dashed horizontal lines.

Figure 6.48 shows the external stress on the north-west abutment pressure cell on Bridge 309 versus the effective temperature of the bridge. The north-west corner of the bridge is outside of the horizontal curve and is on the side of the bridge that is elongated due to skew.

Figure 6.49 shows the external stress on the north-east abutment pressure cell on Bridge 309 versus the effective temperature of the bridge. The north-east corner of the bridge is on the inside of the horizontal curve and is on the side of the bridge that is shortened due to skew. The measured passive stress range was the greatest at this location, compared to the other three locations.

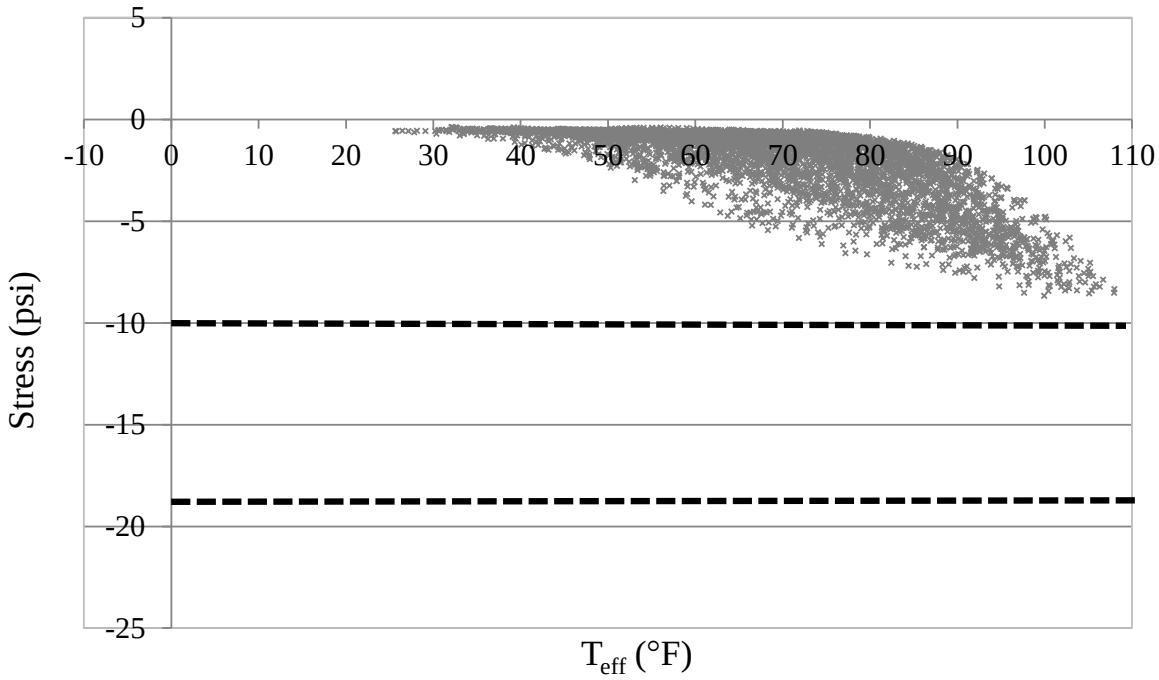

Figure 6.48. North-west abutment backwall pressure vs. effective temperature

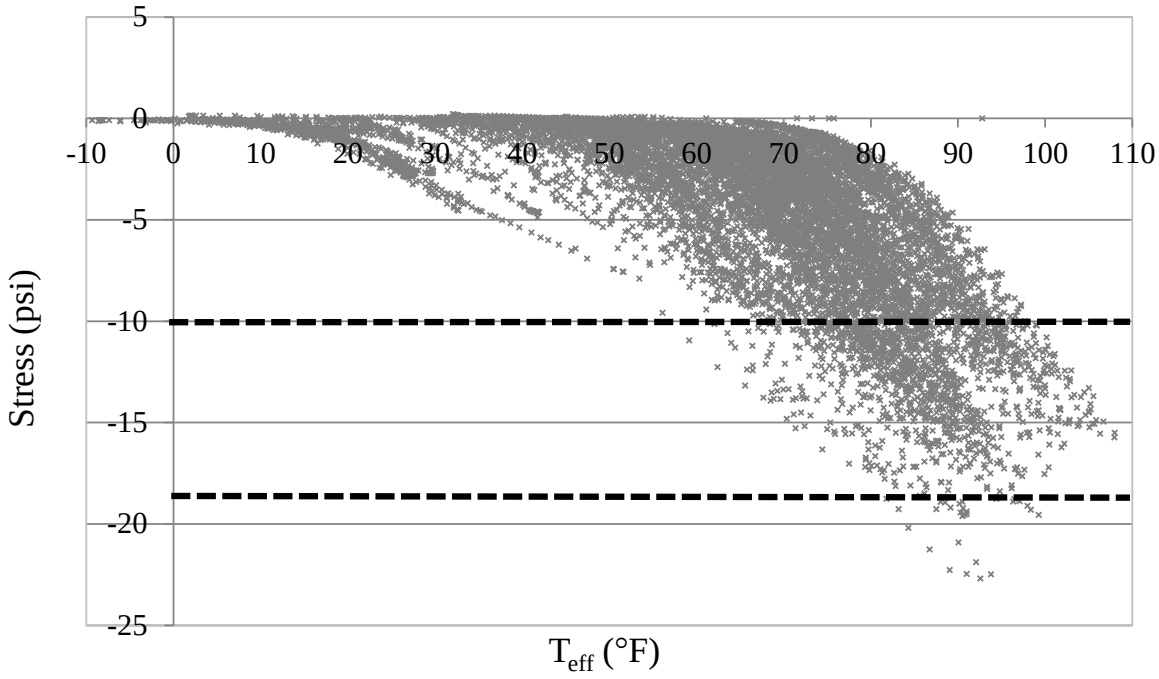

Figure 6.49. North-east abutment backwall pressure vs. effective temperature

Figure 6.50 shows the external stress on the south-west abutment pressure cell on Bridge 309 versus the effective temperature of the bridge. The south-west corner of the bridge is on the outside of the horizontal curve and is on the side of the bridge that is shortened due to the skew.

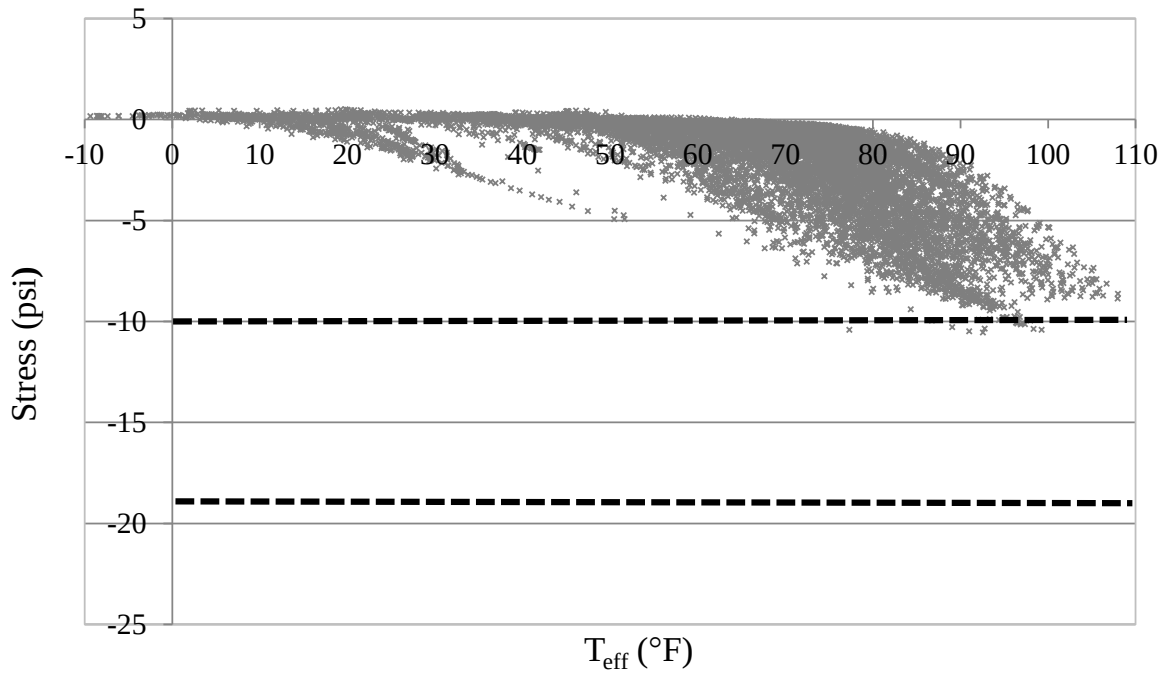

Figure 6.50. South-west abutment backwall pressure vs. effective temperature

Figure 6.51 shows the external stress on the south-east abutment pressure cell on Bridge 309 versus the effective temperature of the bridge. The south-east corner of the bridge is on the inside of the horizontal curve and is on the side of the bridge that is elongated due to the skew.

During the monitoring period of the project a critical hardware component had to be replaced. As a result, six months of data from the south end of Bridge 309 was considered untrustworthy and had to be disregarded. Losing this period of data could have influenced the stress ranges measured and could be a reason for higher stress ranges in the north abutment.

From the pressure cell results, an estimation of the axial stresses in the girders due to soil pressure was calculated, with the purpose of checking the values obtained from the strain gauges. If the soil behind each abutment was assumed to be homogenous and the stress

distribution increases linearly from zero at the surface downward as shown in Figure 6.52. Soil pressure ranges from the pressure cells, mounted 10 in. below the abutment corbel, were observed over a 100 °F range. The measured pressure range for the soil pressure at the bottom of the pile cap was then found by Equation 6.28

$$p_{max} = \frac{p_{gauge} L_{max}}{L_{gauge}} \tag{6.28}$$

where,

L_{max} = the total height of each abutment,

L_{gauge} = the distance from the top of the abutment to the pressure cells,

P_{gauge} = the maximum stress measured at the location of pressure cells, and

P_{max} = the approximated maximum stress at the bottom of the abutment.

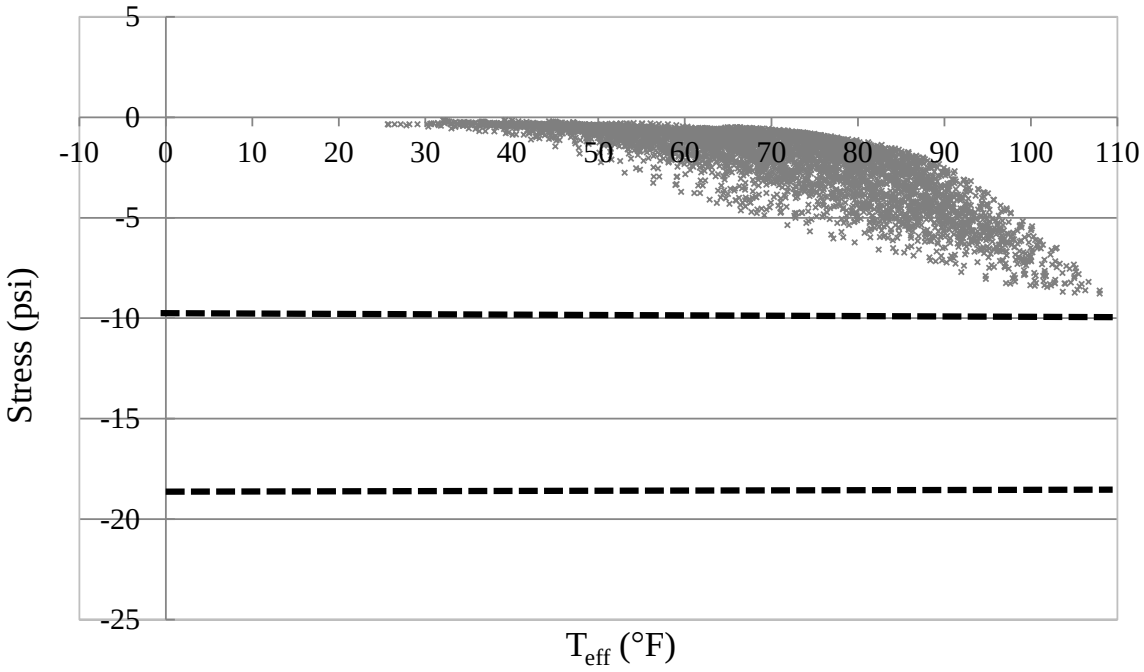

Figure 6.51. South-east abutment backwall pressure vs. effective temperature

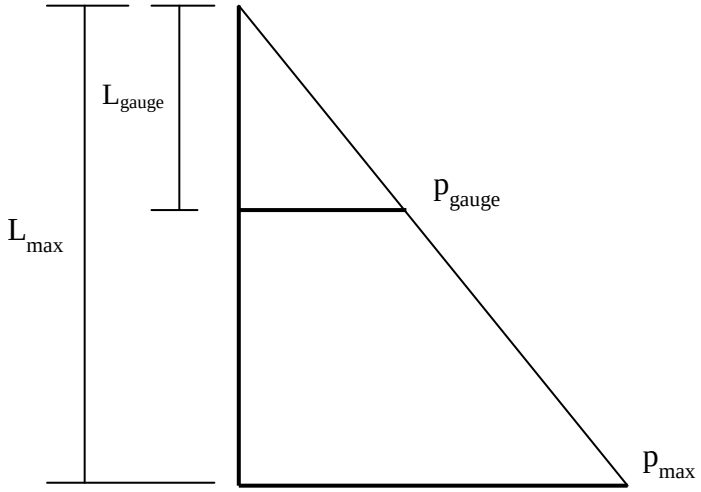

Figure 6.52. Assumed backfill passive stress distribution

Since the measured values of p_{gauge} were different for the east and west pressure cells of each abutment, the calculated values of p_{max} were inconsistent. Therefore, for each abutment an average pressure, p_{avg}, was calculated from the two corresponding values of p_{max} and was assumed constant across the length of the abutment backwall. For each abutment a total passive force (kips) applied to the respective abutment backwall was calculated by

$$P_{total} = (1/2)L_{max}p_{avg}B_{abutment} \quad (6.29)$$

where,

P_{total} = the total approximate force applied to each abutment, and

$B_{abutment}$ = width of the abutment

It was assumed the total force was distributed evenly among each of the four girders, from which a single girder force, $P_{pergirder}$, could be calculated. Table 6.7 shows the results of the approximation.

Table 6.7. Approximation of girder axial force from abutment backwall pressure

	NAPRW (GA)	NAPRE (GD)	SAPRW (GA)	SAPRE (GD)
$P_{approx.}$ (kip)	134		73	
$P_{measured}$(kip)*	690	690	690	500

The discrepancy between the measured and calculated axial forces can be explained by other restraining forces, such as forces from the piers, piles, and pavement.

6.3 MEASURED DISPLACEMENTS

6.3.1 Superstructure Displacement

Coordinate Systems and Coordinate Transformations

The raw survey data for each bridge were initially transformed into global bridge coordinates X and Y, as described previously. To make the raw data useful, the research team transformed the data into local coordinate systems. Figure 6.53 shows both of the local coordinate systems and the global coordinate system. Each abutment and pier has two Cartesian coordinate systems that originate at their respective interior reflector. The first of the two local coordinate systems is aligned with the skew of the abutments and piers. The x-axis of the first system is related to the abutment/pier geometry. The y-axis is 90 degrees counter-clockwise to the x-axis. Displacements for these systems are labeled u, x-axis displacement, and v, y-axis displacement.

The second of the two local coordinate systems is related to the bridge radius. The r-axis is aligned with the radial line passing through the same origin. The t-axis is the 90 degrees counter-clockwise of the r-axis and runs tangent to the bridge's horizontal curve. Displacements for the radial system are labeled u′, r-axis displacement, and v′, t-axis displacement.

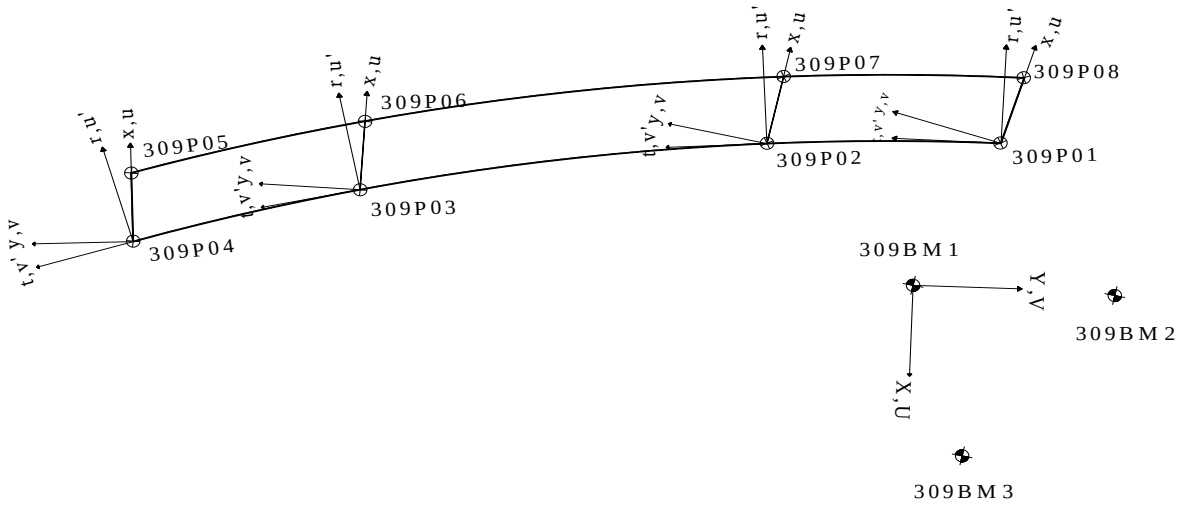

Figure 6.53. Local abutment and pier coordinate systems

Bridge 309 Benchmark Three Movements

The surveying results rely upon the assumption that the benchmarks remain stationary throughout the length of the project and their location can be accurately measured with a total station. Figure 6.54 shows the average location of benchmark three for Bridge 309, as measured by the monthly surveys, for each month a survey was conducted. Each month is represented by a circle and is labeled accordingly. The figure shows that there are errors in either the assumption that the benchmark remains stationary or that its location can be accurately measured during each survey. In general, most of the months are within roughly 0.3in. of each other. Two outliers, August 2011 and November 2011, are roughly 0.6 in apart.

Total Change in Length

Throughout the project each bridge at the NEMM was surveyed each month. From these data the research team was able to track the length changes of each bridge. The total change in length for each bridge was calculated from the displacements in the t-axis direction, v′, at both abutments. Figures 6.55 through 6.60 show the change in length of bridges 109, 209, 309, 2208, 2308, and 2408 versus effective bridge temperature. In each of the figures, each survey month is represented by a rectangle where the vertical sides of the rectangle represent the 95% confidence interval of the results and the horizontal sides of the rectangle represent the change in effective temperature during the time of the survey. The solid diagonal line

represents the change in length based on free expansion and contraction of the bridge, and the dashed diagonal line represents the best fit line from the survey results. The horizontal solid and dashed lines represent the range of the change in length of theoretical free expansion and measured expansion of the bridge, respectively. These ranges can also be considered the total change in length of the bridges during the project.

Figure 6.55 shows the measured values of the change bridge length versus the effective temperature for Bridge 109, a straight integral abutment bridge with two fixed piers. The best fit line of the surveying results shows a linear relationship between the change in length and the effective temperature of the bridge that is similar to that of the theoretical free expansion line.

Figure 6.56 shows the total change in length of Bridge 209, a semi-integral abutment bridge with a fixed and expansion pier, as calculated by the surveying as well as by expansion meters mounted on each abutment. The movements measured by the expansion meters record a plateauing at both ends of the temperature spectrum, something the research team was unable to explain.

Figure 6.57 shows the total change in length measurements of Bridge 309 measured by the monthly survey as well as by long range distance meters mounted at each abutment and pier. Bridge 309 is an integral abutment bridge with two fixed piers. For the most part, the measured results from the survey data and from the long range distance meters correspond to one another and both show a linear relationship between the change in length of the bridge and the effective temperature of the bridge.

Figure 6.58 shows the total change in length versus effective bridge temperature for Bridge 2208, an integral abutment bridge with a fixed and expansion pier. The best fit of the survey line and the theoretical free expansion line produce very close results, suggesting less expansion restraint at this bridge.

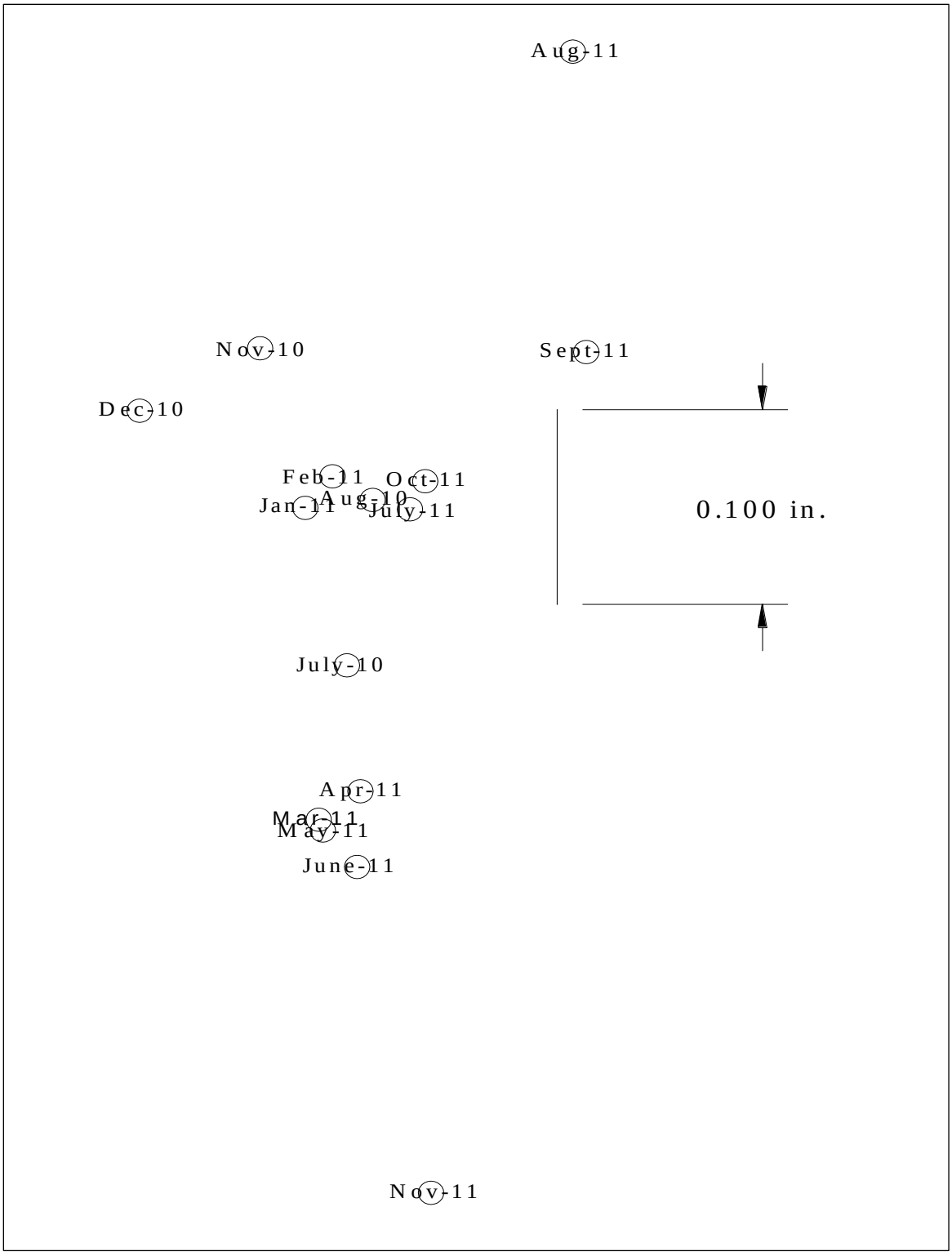

Figure 6.54. Bridge 309 Benchmark three movements

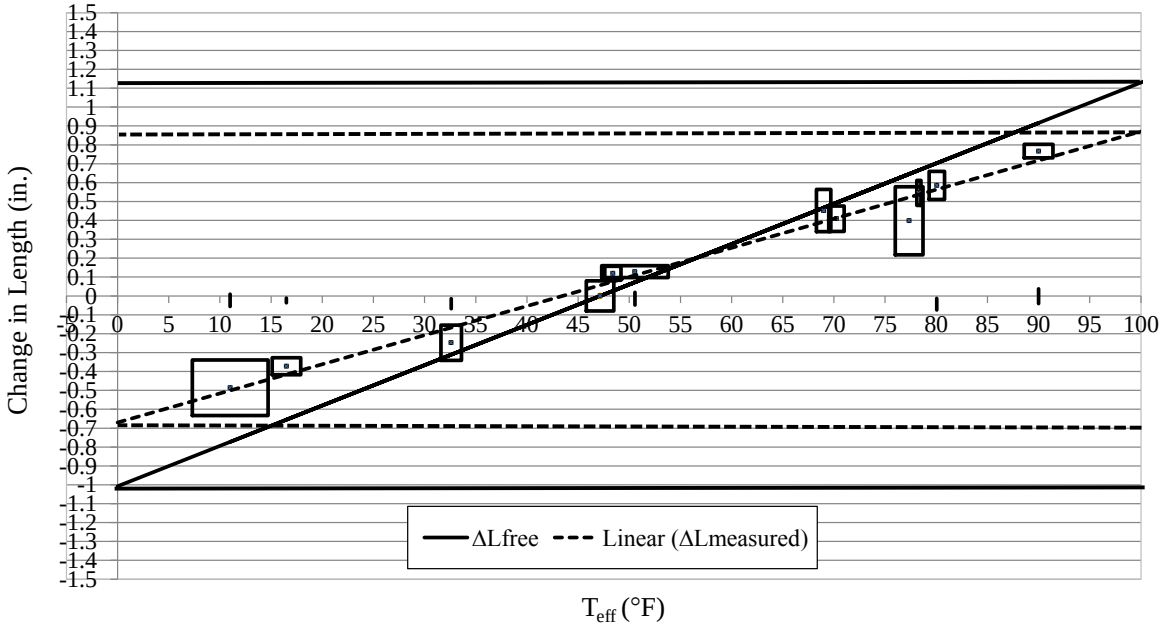

Figure 6.55. Total change in length Bridge 109

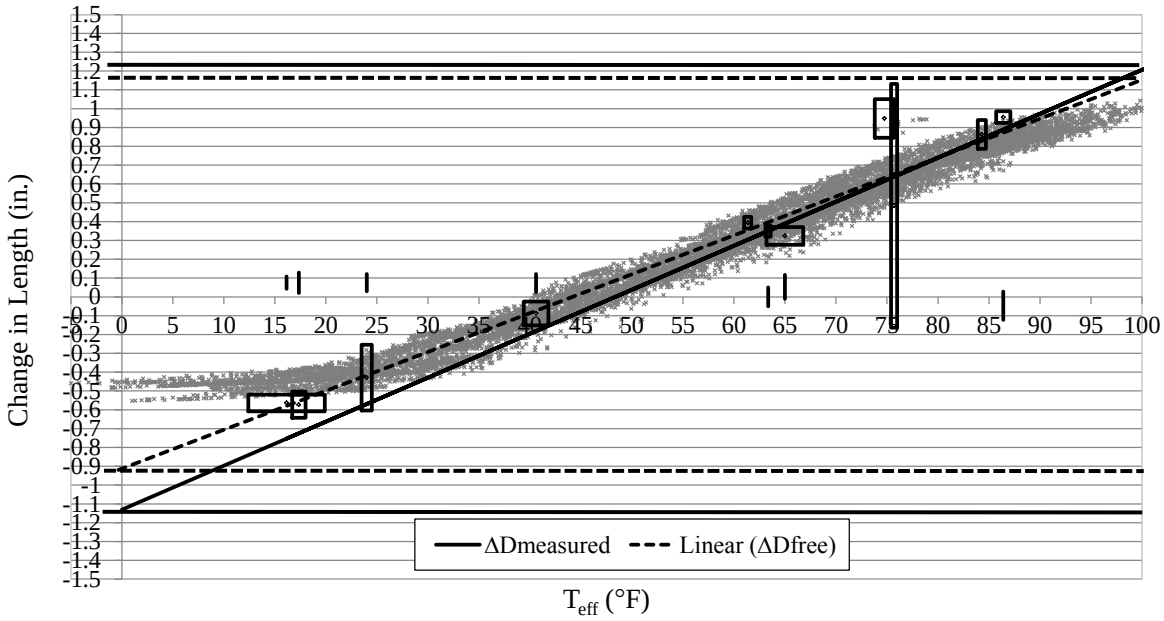

Figure 6.56. Total change in length Bridge 209

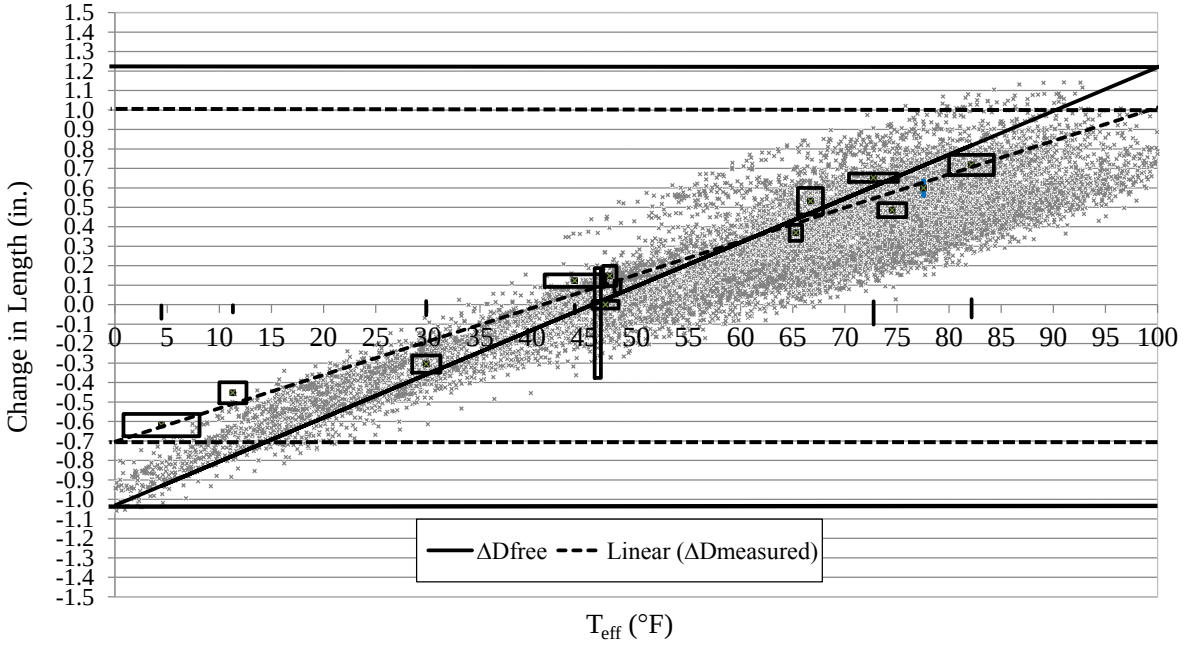

Figure 6.57. Total change in length Bridge 309

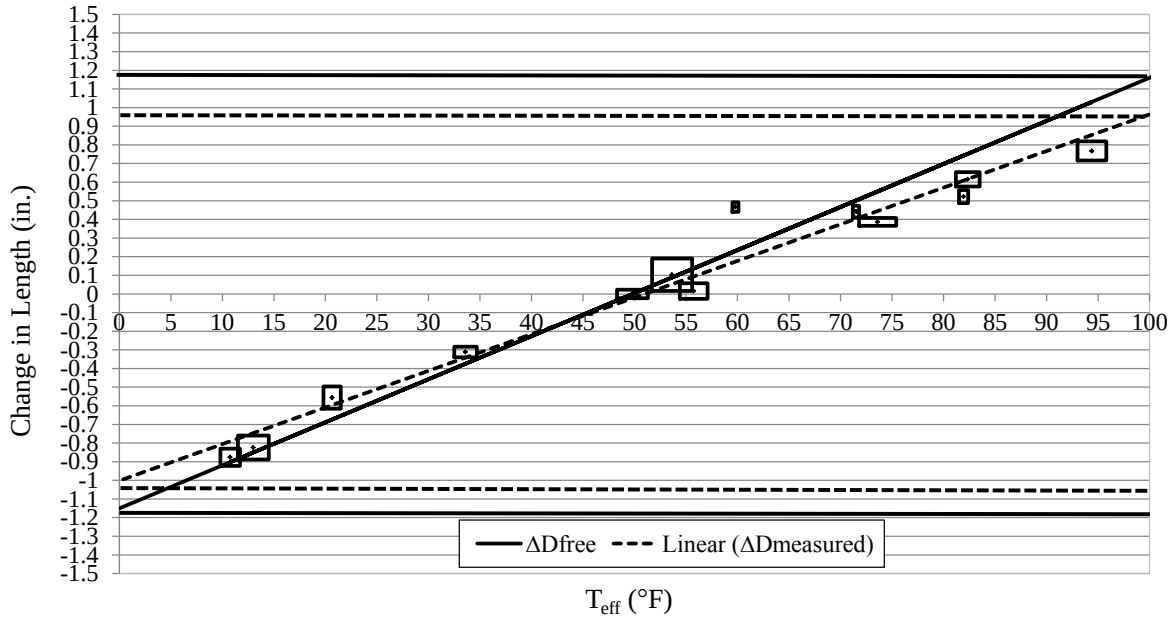

Figure 6.58. Total change in length Bridge 2208

Figure 6.59 displays the total change in length of Bridge 2308 by surveying and expansion meter measurements. As with bridge 209, the expansion meters plateau at high and low temperatures. Bridge 2308 is a semi-integral abutment bridge with two fixed piers.

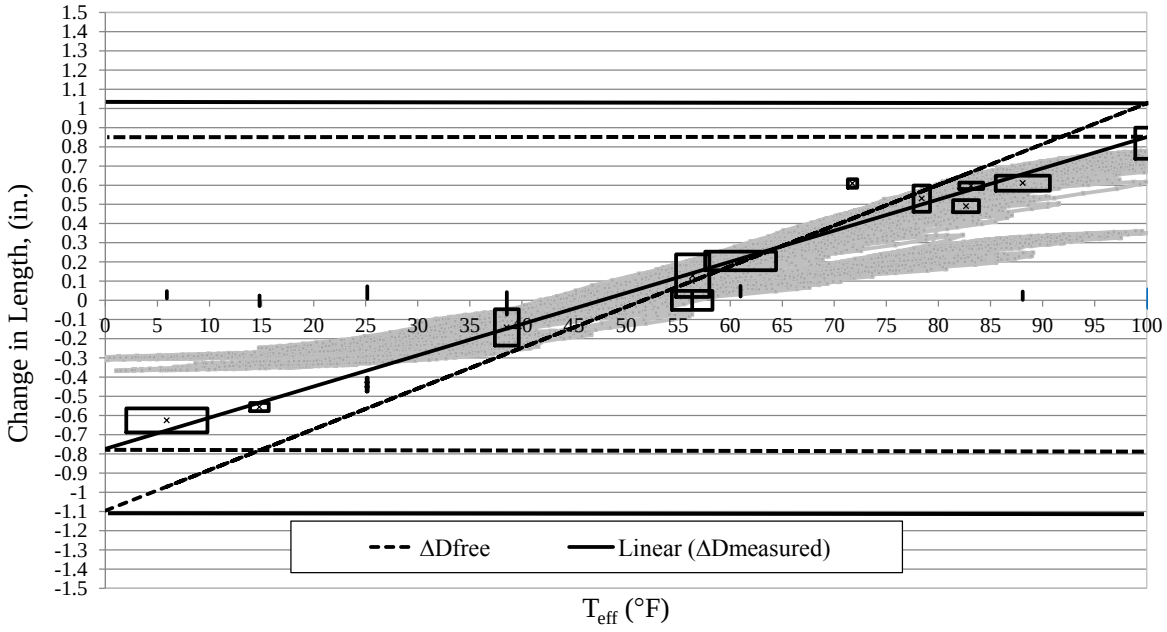

Figure 6.59. Total change in length Bridge 2308

Figure 6.60 shows the total change in length of Bridge 2408 versus the effective bridge temperature. As with Bridge 109, Bridge 2408 is a straight bridge with integral abutments and two fixed piers.

The results from each figure were tabulated for comparison. Table 6.8 shows the total free expansion change in length, ΔL_{free}, and the total measured change in length, $\Delta L_{measured}$, for each bridge.

An axial strain as a result of expansion resistance was calculated from the difference between these two lines by Equation 6.30:

$$\Delta\varepsilon_r = (\Delta L_{free} - \Delta L_{measured})/L \qquad (6.30)$$

where,

$\Delta\varepsilon_r$ = resistance axial strain, and

L = length of bridge along curve.

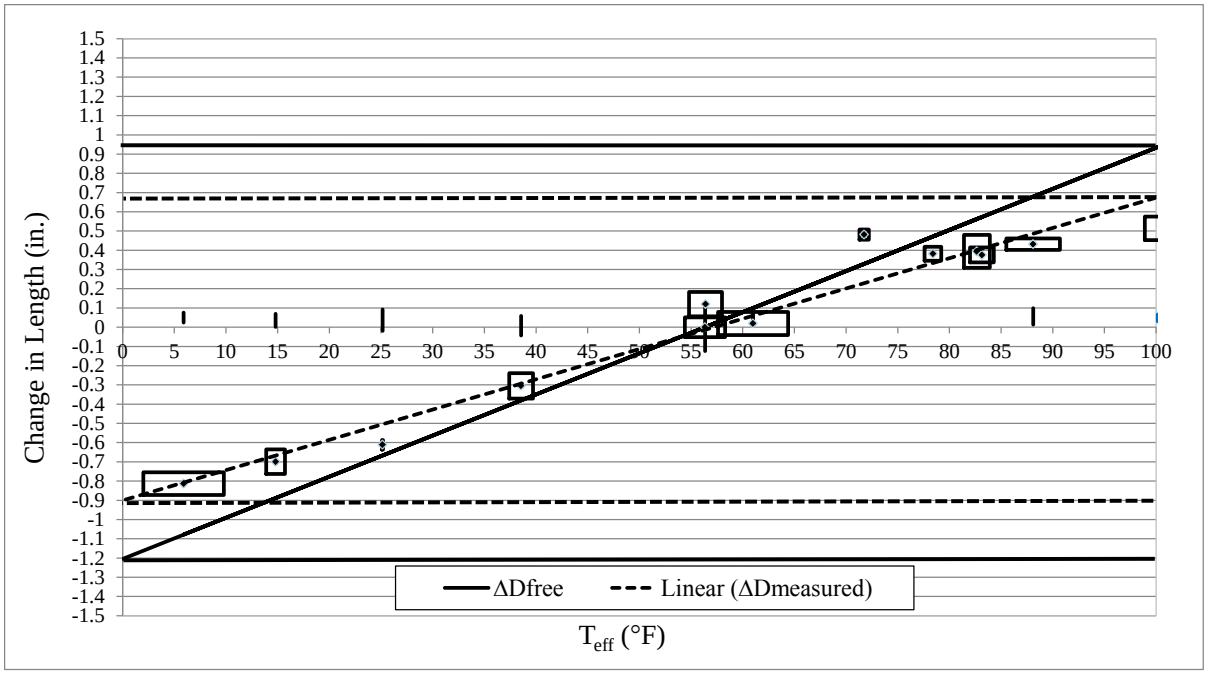

Figure 6.60. Total change in length Bridge 2408

Table 6.8. Total free expansion and measured change in length

Bridge/Range	109	209	309	2208	2308	2408
ΔL_{free}	2.14	2.32	2.24	2.24	2.14	2.14
$\Delta L_{measured}$	1.54	2.15	1.7	2.00	1.65	1.58

Table 6.9 shows the results from Equation 6.33 as well as the average axial strain in the respective bridge from the strain gauge data.

Table 6.9. Calculated average axial strain vs. measured average axial strain

Bridge/Strain	109	209	309	2208	2308	2408
$\Delta\varepsilon_r(\mu\varepsilon)$	141	43	141	61	135	154
$\Delta\varepsilon_a(\mu\varepsilon)$	180	169	165	108	153	NA

The resistance axial strain, $\Delta\varepsilon_r$, is similar to the strain-gauge measured axial strain, $\Delta\varepsilon_a$, for Bridges 109, 309, and 2308. The resistance axial strain for Bridges 209 and 2208 are much lower than the strain-gauge measured axial strain, and no comparison can be made for Bridge 2408 as there is no strain-gauge data.

Total Change in Span Length

From the survey data, the change in span length was calculated from displacements along

the respective t-axis at the abutments and piers, v′. Figures 6.61 through 6.66 show the change in span length for Girder A and Girder D of each span of Bridges 109, 209, 309, 2208, 2308, and 2408, respectively. Also shown in the figures are the average of Girder A and Girder D for each span and the total average of all spans.

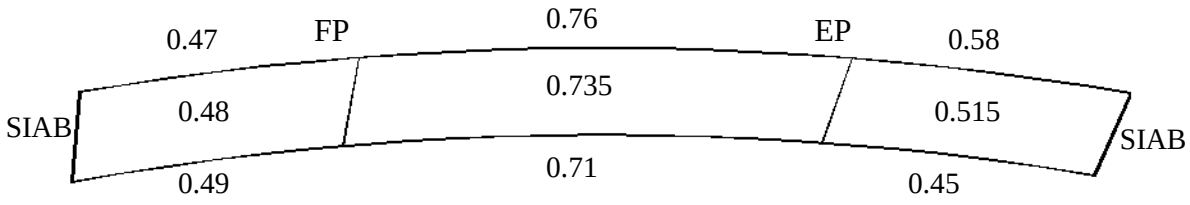

Avg: 0.58

Figure 6.61. Change in length per span Bridge 209

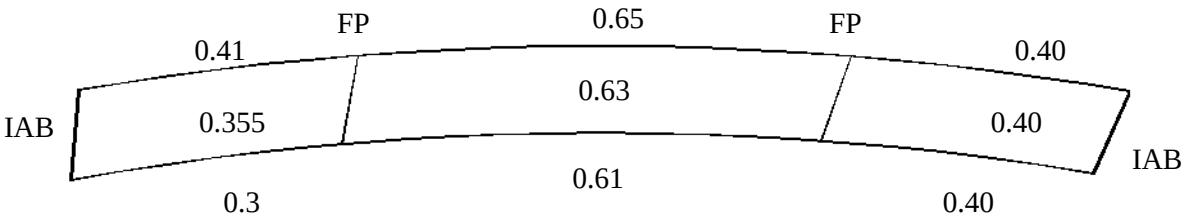

Avg: 0.46

Figure 6.62. Change in length per span Bridge 309

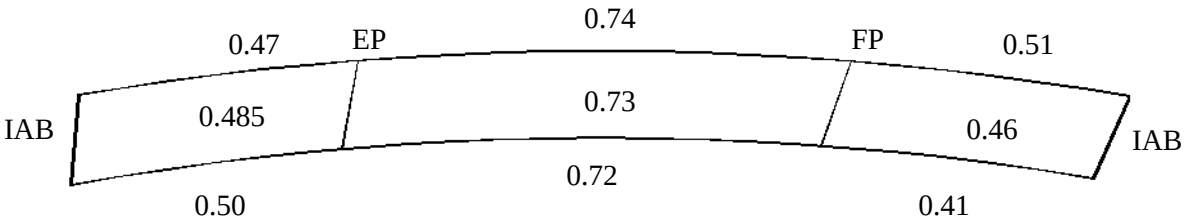

Avg: 0.56

Figure 6.63. Change in length per span Bridge 2208

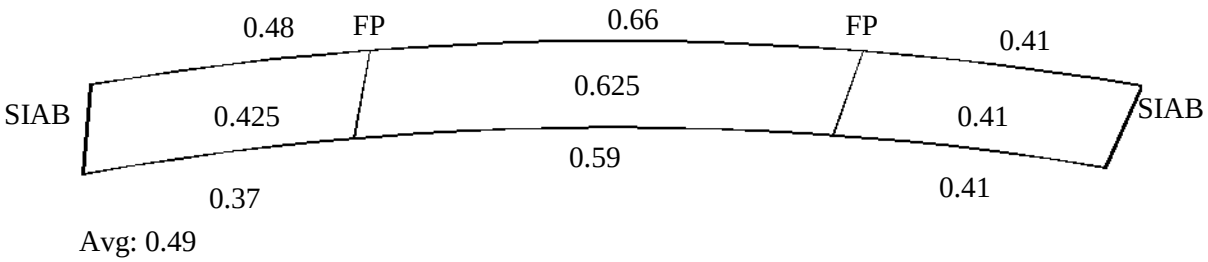

Figure 6.64. Change in length per span Bridge 2308

Figure 6.65. Change in length per span Bridge 109

Figure 6.66. Change in length per span Bridge 2408

As shown in Figure 6.60 through 6.66 the change in length of the center span is, as one might expect, largest for all bridges. With regard to the curved-girder bridges, Figure 6.60 through 6.64, the bridges with one fix pier and one expansion, Bridge 209 and 2208, show higher values in the change in length of the center span compared to the two bridges with both piers fixed, Bridge 309 and 2308. With regard to the two straight bridges, Bridge 109 and 2408, the change in length of both end spans and the center span were similar between

the bridges.

Bridge Movements Month to Month

The monthly reflector coordinates calculated from the survey data were input into a commercial drafting program. This allowed the research team to produce graphical images summarizing the bridge movements with time. Because the movements were very small compared to the geometry of the bridges, the drawings had to be scaled. In the following the scale is shown in its respective figure.

Figures 6.67 through 6.72 display the location of the bridge, at the reflectors, for three months during the monitoring portion of the project life. The three months include February 2011, a cold month; April 2011, the reference month; and July 2011; a hot month. In the figures, the respective bridge is shortest during the cold month, at its longest during the hot month, and in the middle during the reference month.

Figures 6.73 through 6.96 track the monthly location of the abutments and piers reflectors on each bridge during the monitoring period. The west and east reflectors at each abutment and pier are positioned next to each other. Also, the figures are ordered starting with the north abutment and end with the south abutment, for each bridge respectively.

In general the reflector movements documented by Figures 6.73 through 6.96 show much larger longitudinal movements of the bridge superstructure compared to radial or transverse movements. As one might expect, the movement ranges of the superstructures near fixed piers are generally smaller than the movement ranges displayed near an expansion pier. The range of superstructure movements documented near IAB's and SIAB's show little difference between the two abutment configurations. Also, generally there is little noticeable difference between the movements in both the longitudinal and transverse direction of the two straight bridges and the four horizontal bridges when considering similar pier and abutment fixities.

Effective Thermal Length

One way to calculate longitudinal forces on piers from thermal expansion of girders is to establish a design length. The design length is the length of a girder whose expansion contributes to the development of forces on the pier. From here on, this report refers to this as the effective thermal length.

Table 6.6.2.12.4.1 of the Iowa Dot's LRFD Bridge Design Manual specifies an effective thermal length based on abutment and pier fixity configuration. The table covers two- to four-span integral abutment bridges with expansion and fixed piers, and is used with bridges that do not have large variations in pier stiffness (Offices 2011). In this report, the research team used the survey data and Equation 6.31 to calculate an effective thermal length.

$$L_{eff} = \frac{\Delta d}{\alpha_{eff} \Delta T} \tag{6.31}$$

where,

Leff = effective thermal length,

Δd = range on longitudinal movement of fixed pier or integral abutment, and

ΔT is a temperature range of 100°F.

Table 6.10 shows the effective thermal length calculated by the research team as well as the effective thermal length given by the Iowa DOT. The Iowa DOT's values are in parentheses.

Table 6.10. Effective Thermal Length

Bridge/Location	S. Abut (ft)	S. Pier (ft)	N. Pier (ft)	N. Abut (ft)	Bearing
109	91		72	105	IAB-EP-FP-IAB
309	95	60 (74.5)	65 (74.5)	116	IAB-FP-FP-IAB
2208	142		113	150	IAB-EP-FP-IAB
209		51			SIAB-FP-EP-SIAB
2308		50 (71)	46 (71)		SIAB-FP-FP-SIAB
2408	155	115		101	IAB-FP-EP-IAB

As shown in Table 6.10, the effective thermal length approximation proposed by the Iowa DOT results in higher effective thermal lengths. As a result, there is a level of conservatism built into their design. Also, the results of the approach taken by the research team results in values for end spans that are larger than the actual length of the corresponding

span.

Fixed Pier Displacement

The fixed pier of Bridge 109, the north pier, was instrumented with an expansion meter to measure the relative displacement between the bottom flange of Girder B and the pier cap. Figure 6.97 shows the displacement results from the expansion meter vs. effective bridge temperature.

Figure 6.97 shows that there is little measurable relative displacement between the pier cap of the fixed pier and the bottom flange of Girder B. As a result, this figure helps to confirm pier fixity assumptions.

Along with the relative displacement between the pier cap and the bottom flange of Girder B, the absolute displacement of the bottom flange of Girder B perpendicular to the pier was calculated using the survey data. Figure 6.98 shows the results of the absolute movement of Girder B from the survey.

Combining the results of Figure 6.97 and Figure 6.98 implies that, although there is no relative movement between the pier cap and the bottom flange of Girder B, there is movement at the pier location. Thus, there must be flexure in the pier due to thermal girder movement induced forces.

Expansion Pier Displacement

The expansion pier of Bridge 209 and Bridge 2208 was instrumented with an expansion meter. This meter measured the relative displacement between the bottom flange of Girder B and the pier cap. Figure 6.99 shows the results of typical relative displacement of the expansion pier measured by the expansion meter and by the surveying results. Similar to the displacements measured by the expansion meters mounted on the semi-integral abutments, the expansion meters mounted on the expansion piers start to plateau at the effective bridge approaches the hot and cold extremes.

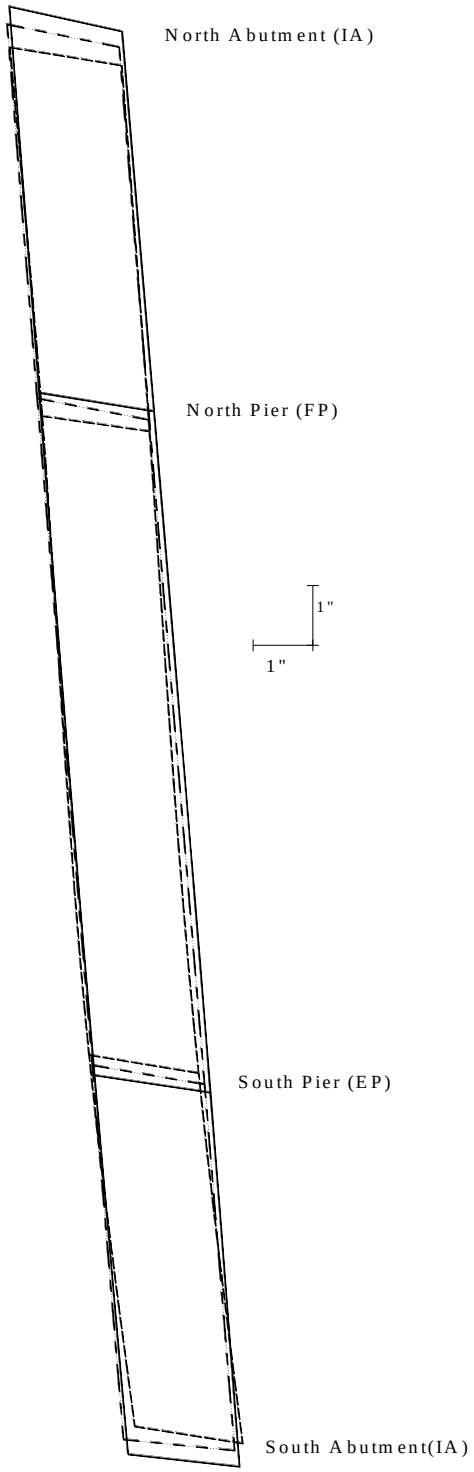

Figure 6. 67. Deflected shape Bridge 109

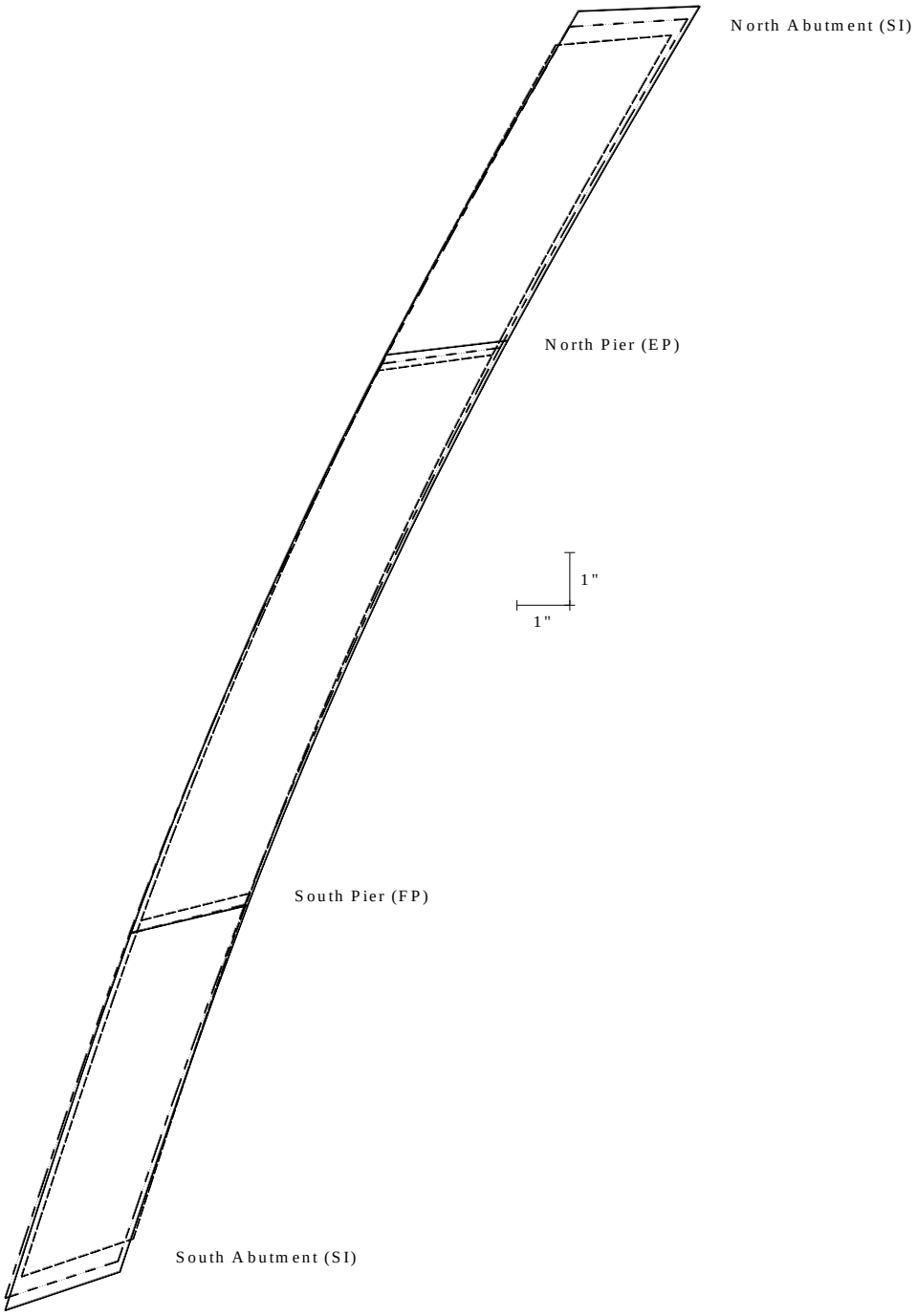

Figure 6.68. Deflected shape Bridge 209

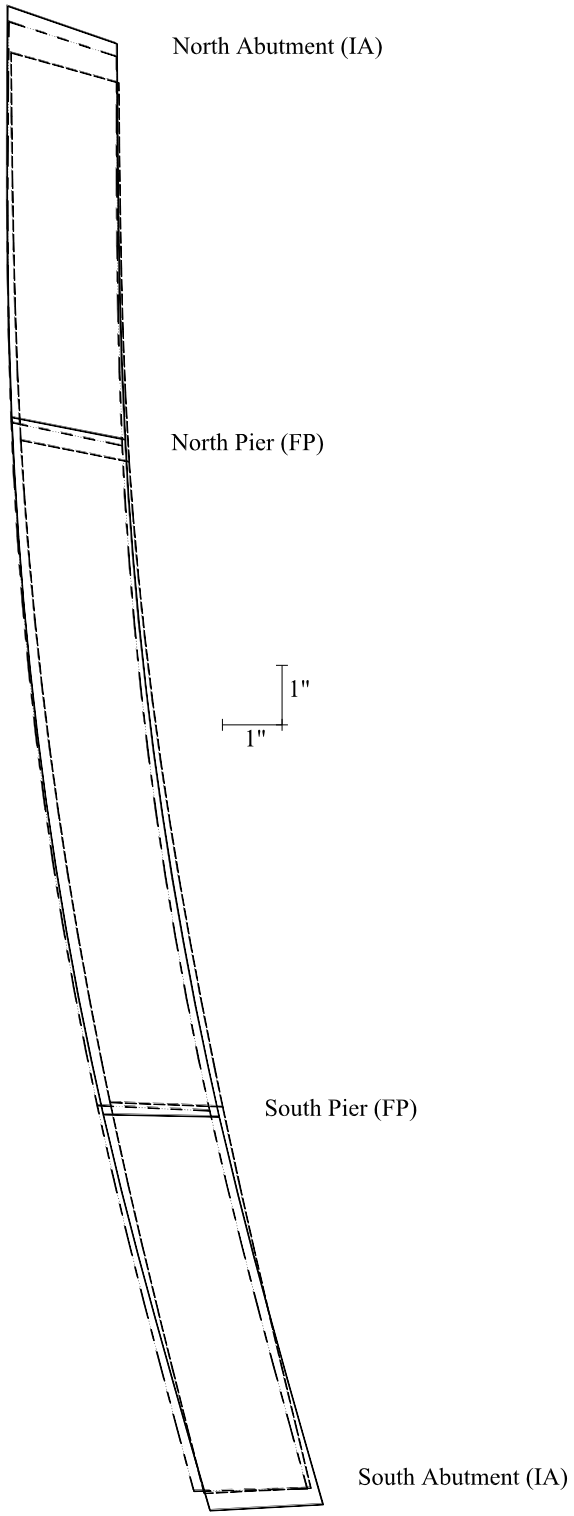

Figure 6.69. Deflected shape Bridge 309

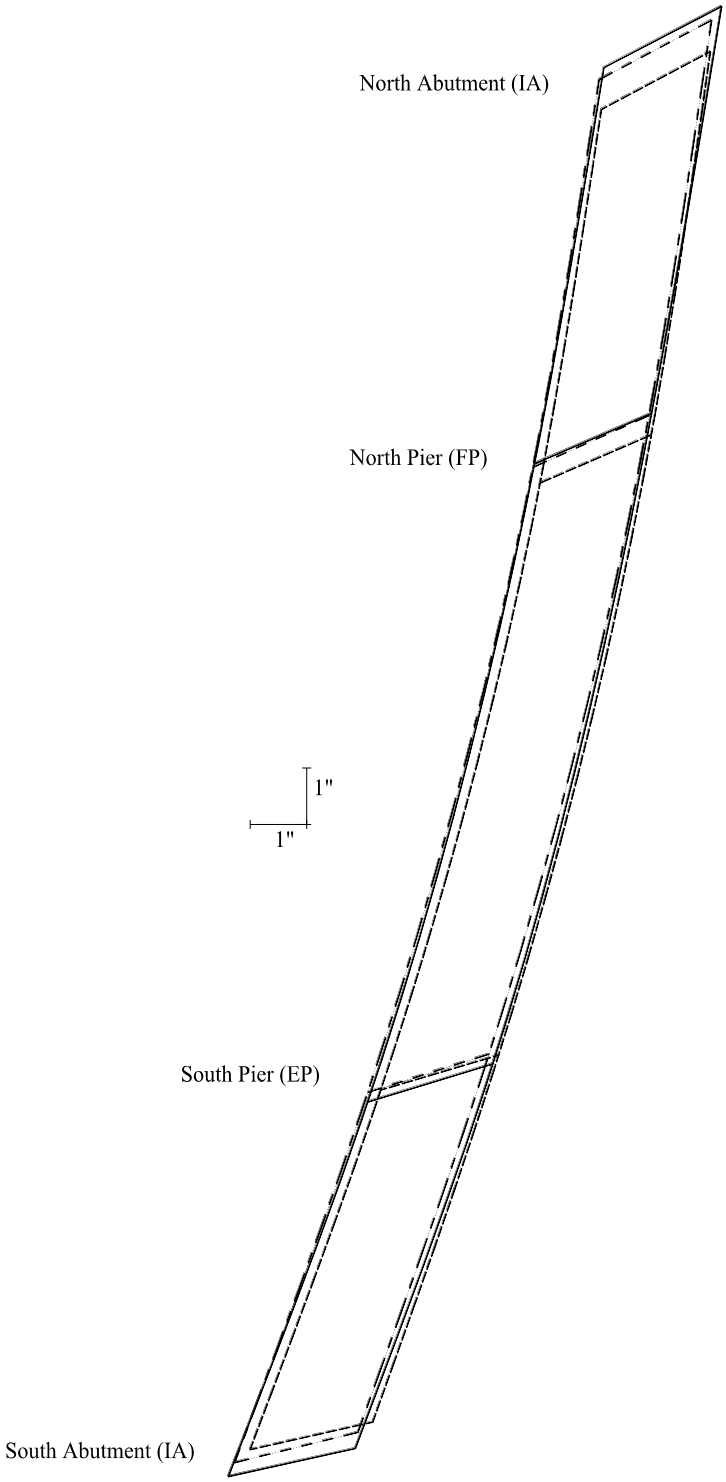

Figure 6.70. Deflected shape Bridge 2208

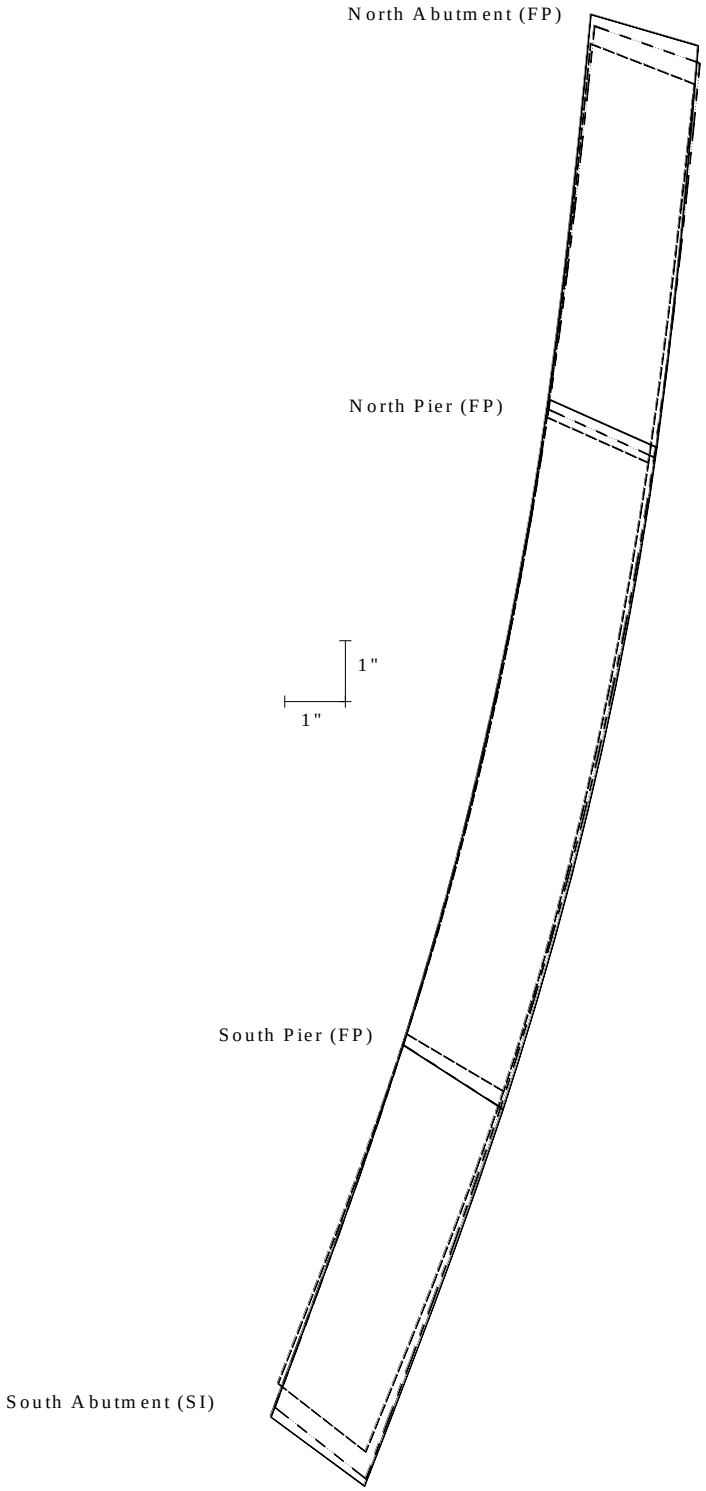

Figure 6.71. Deflected shape Bridge 2308

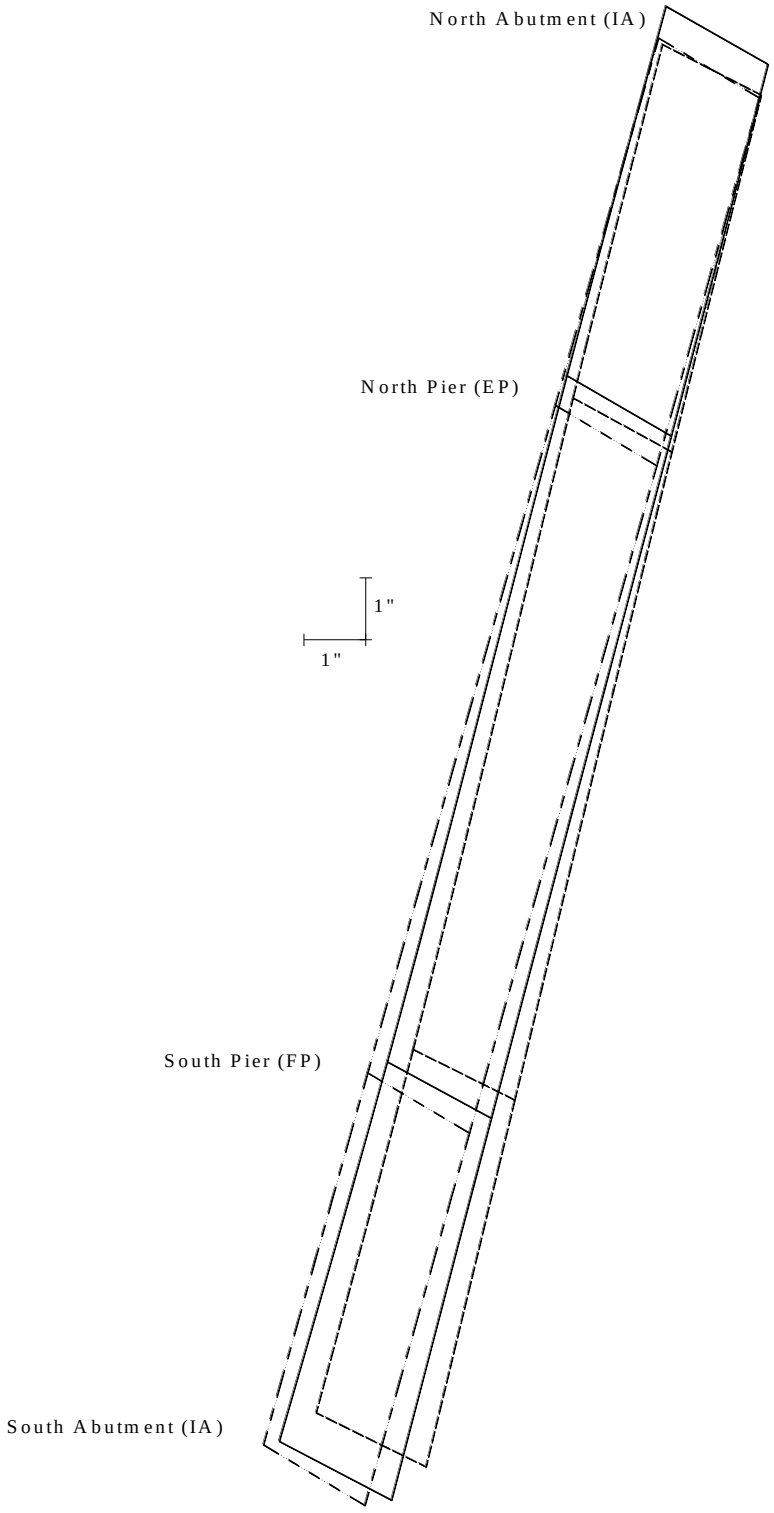

Figure 6.72. Deflected shape Bridge 2408

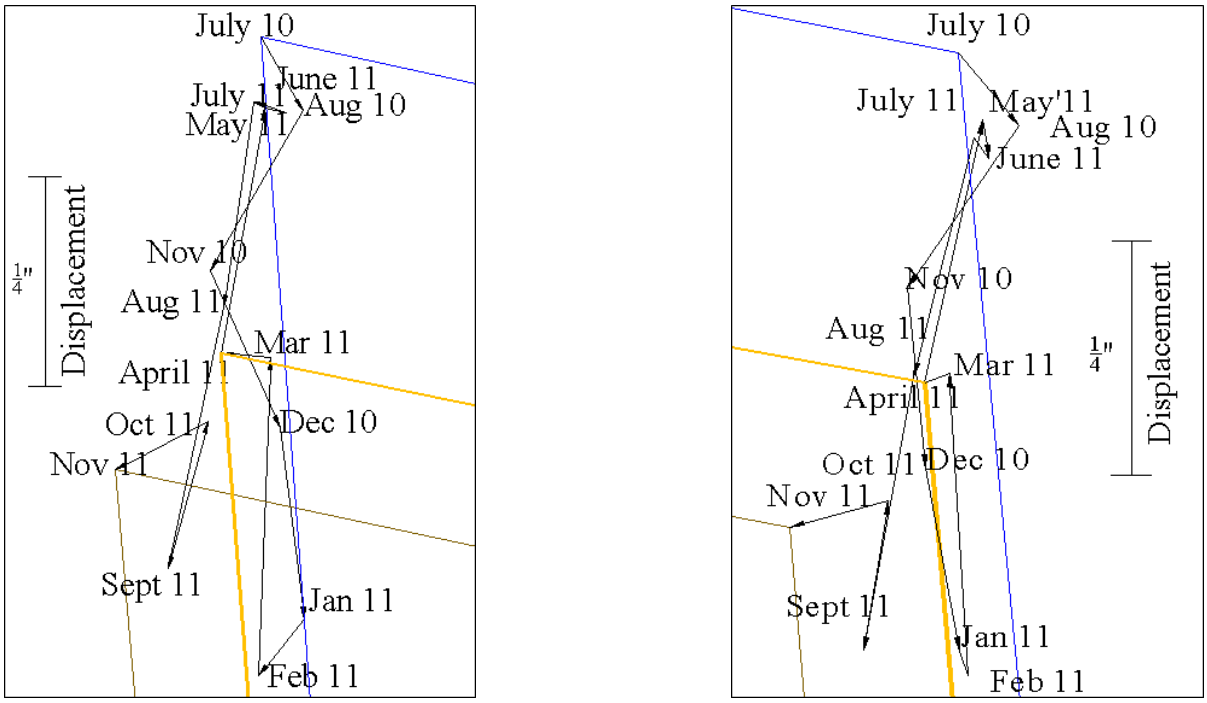

Figure 6.73. Bridge 109 movements at north abutment west and east reflectors

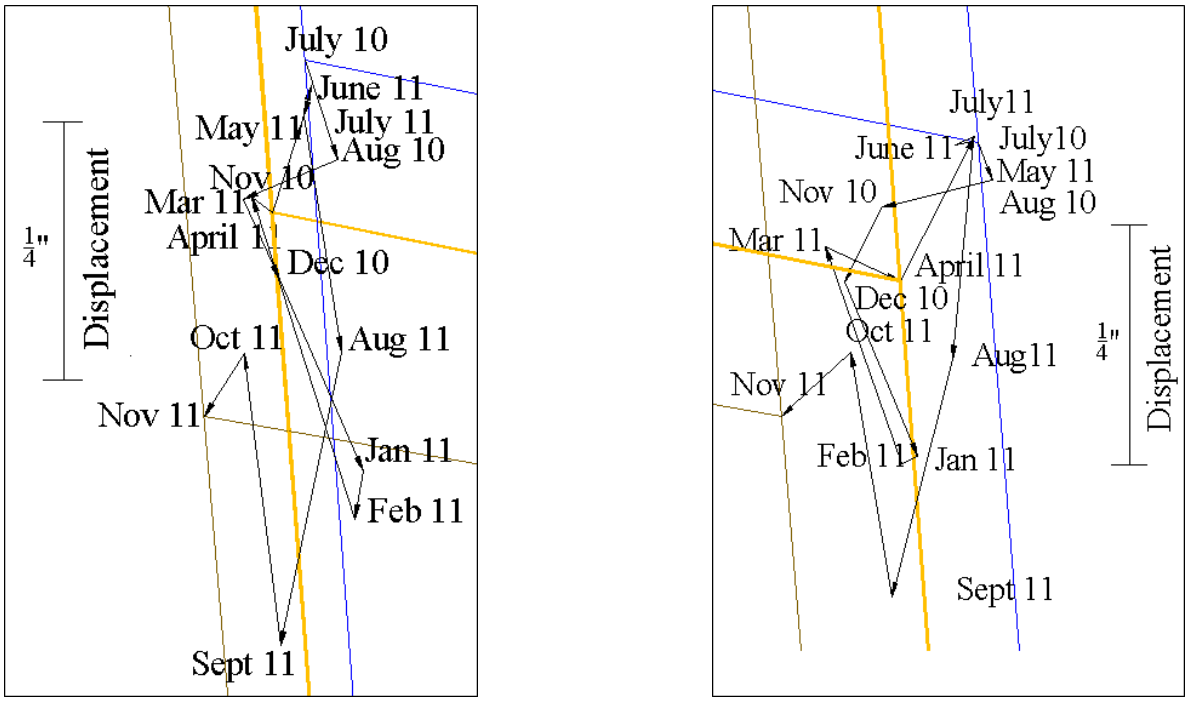

Figure 6.74. Bridge 109 movement at north pier west and east reflectors

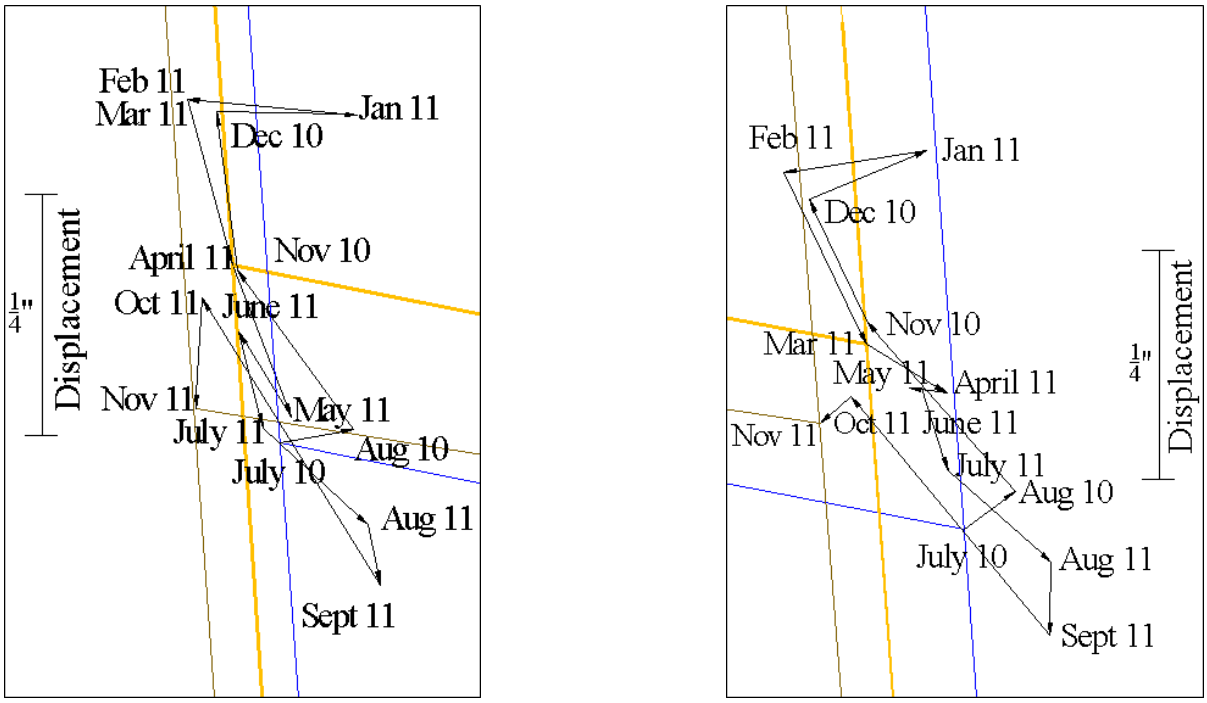

Figure 6.75. Bridge 109 movement at south pier west and east reflectors

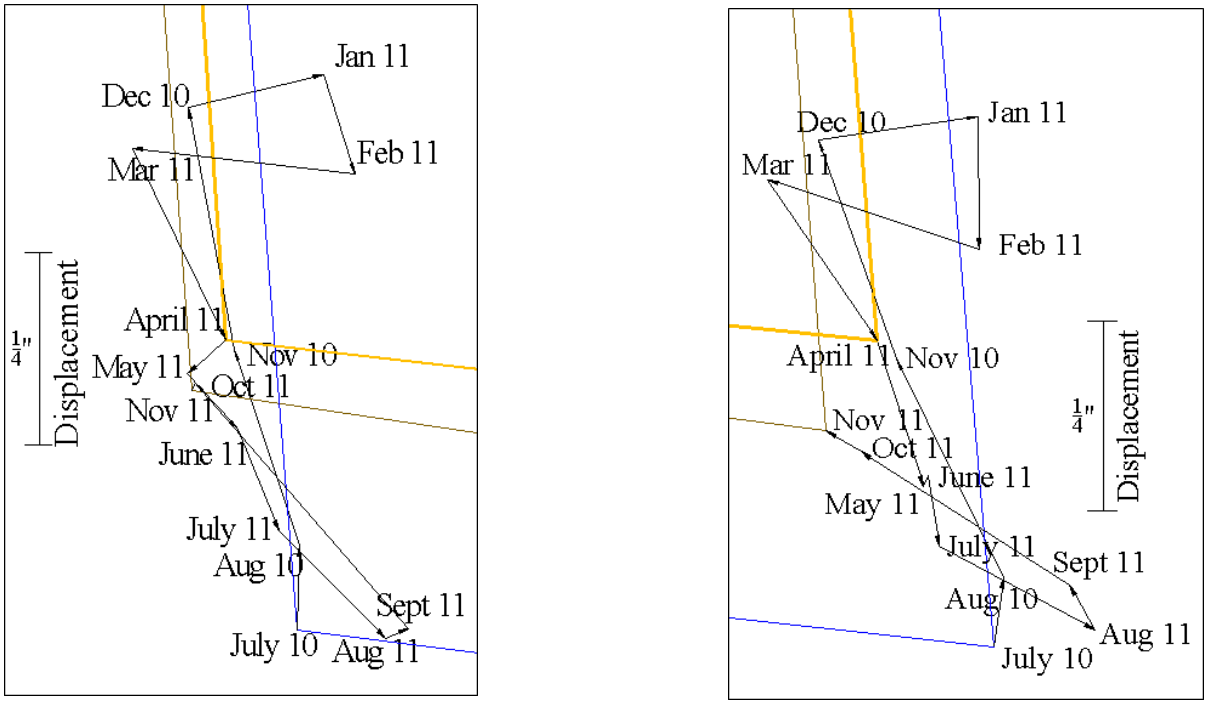

Figure 6.76. Bridge 109 Movement at south abutment west and east reflectors

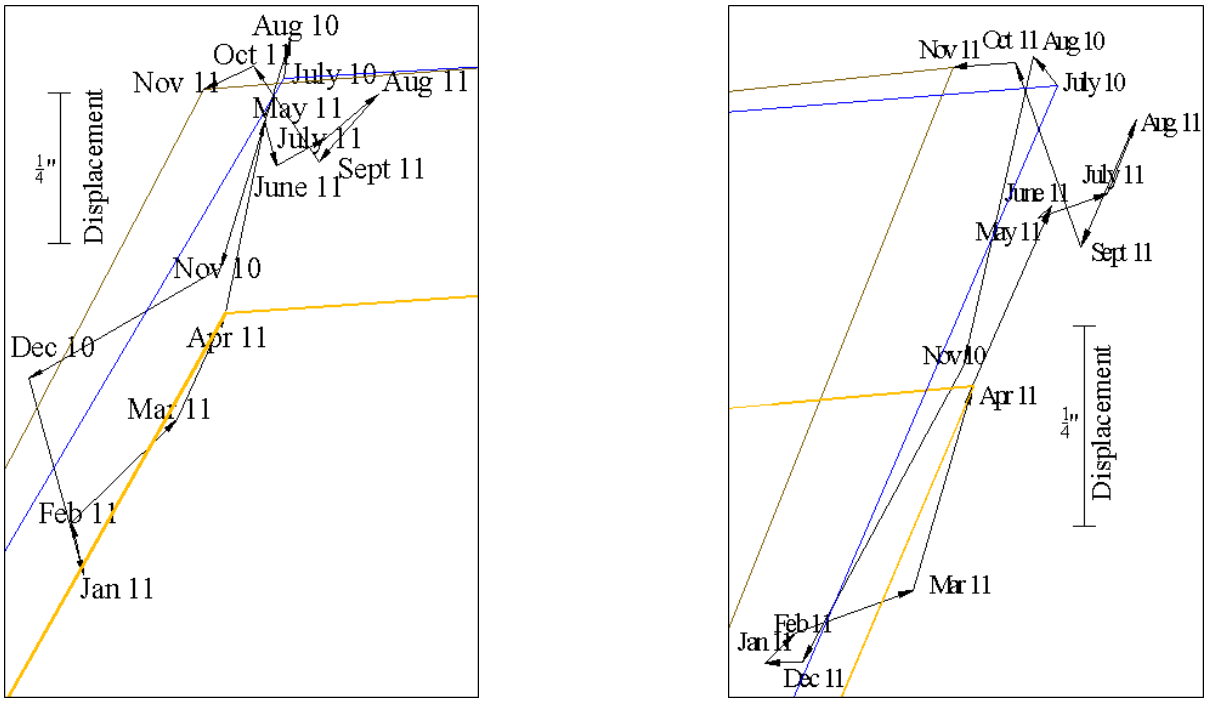

Figure 6.77. Bridge 209 movement at north abutment west and east reflectors

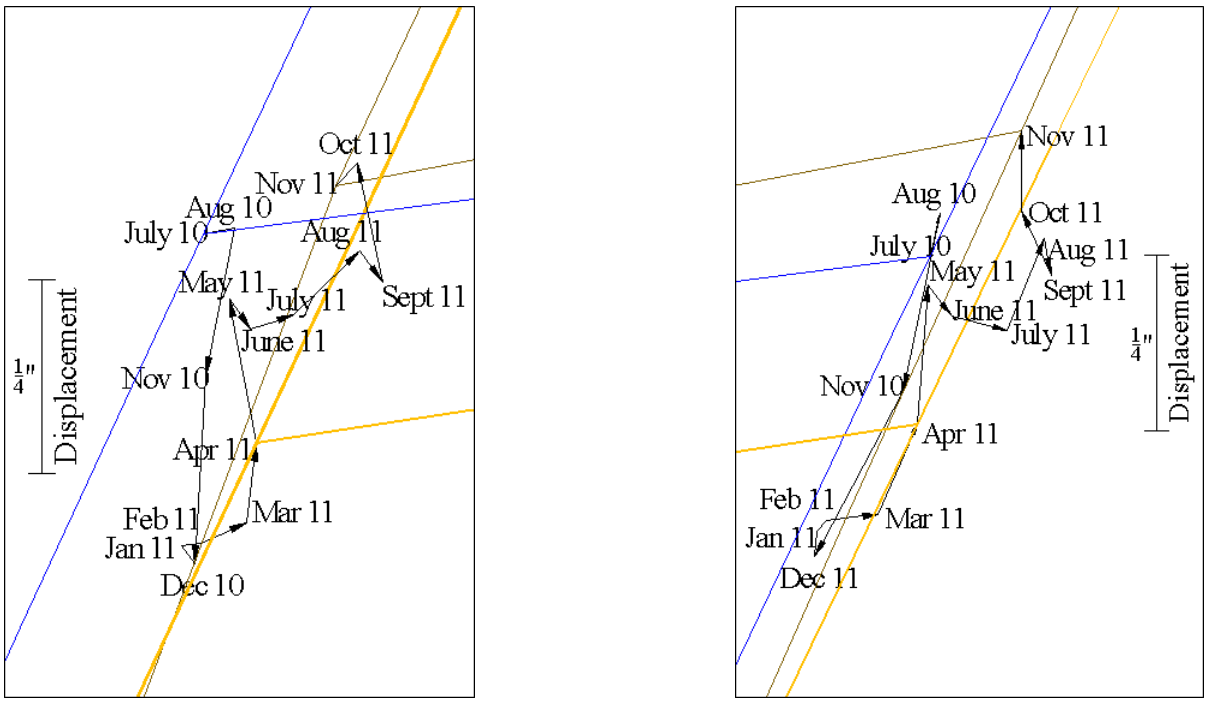

Figure 6.78. Bridge 209 movement at north pier west and east reflectors

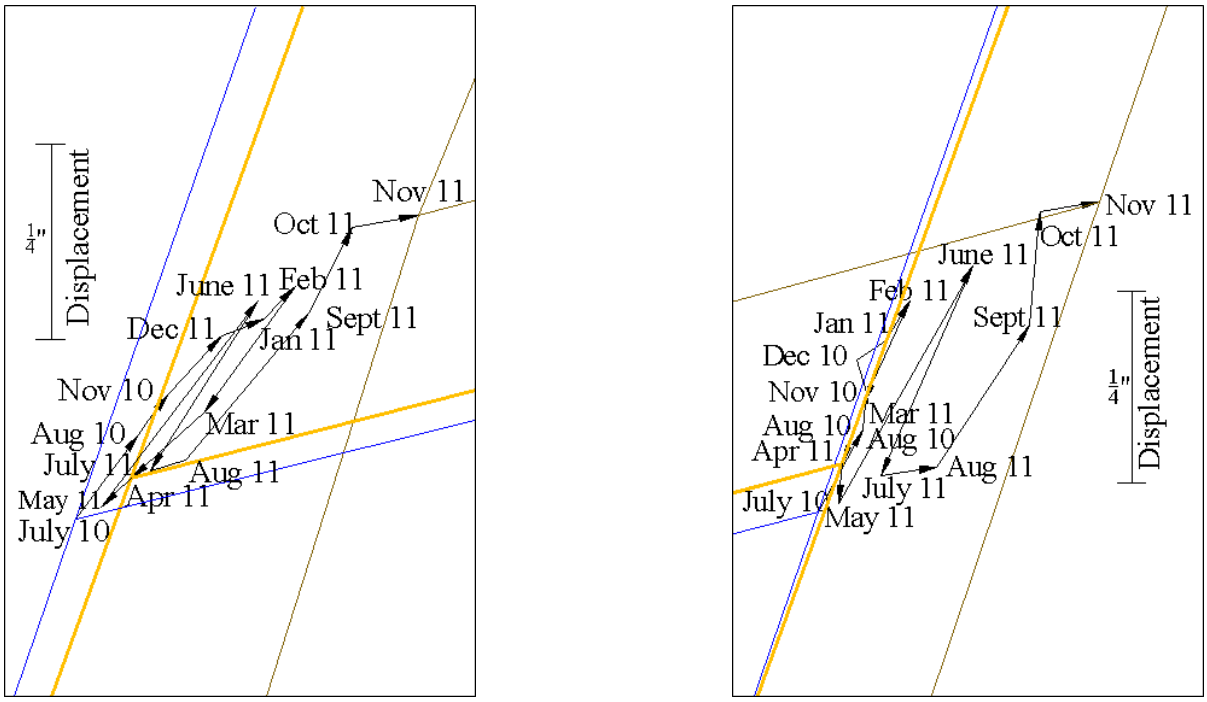

Figure 6.79. Bridge 209 movement at south pier west and east reflectors

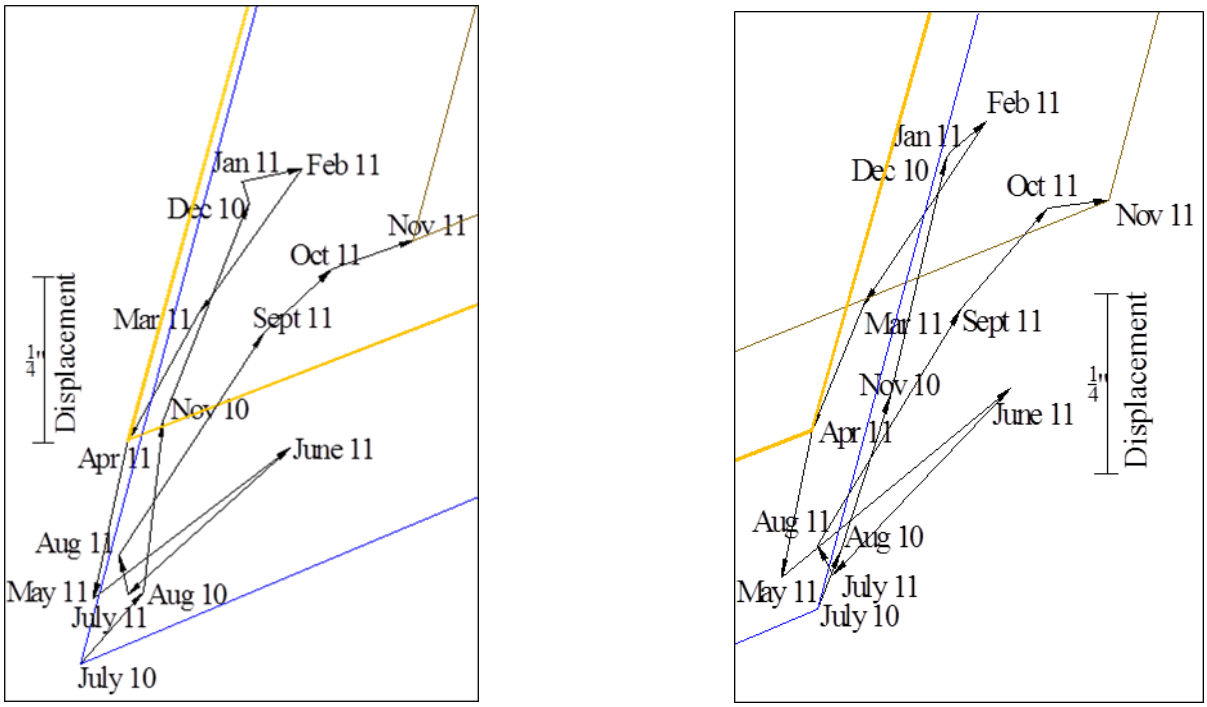

Figure 6.80. Bridge 209 movement at south abutment west and east reflectors

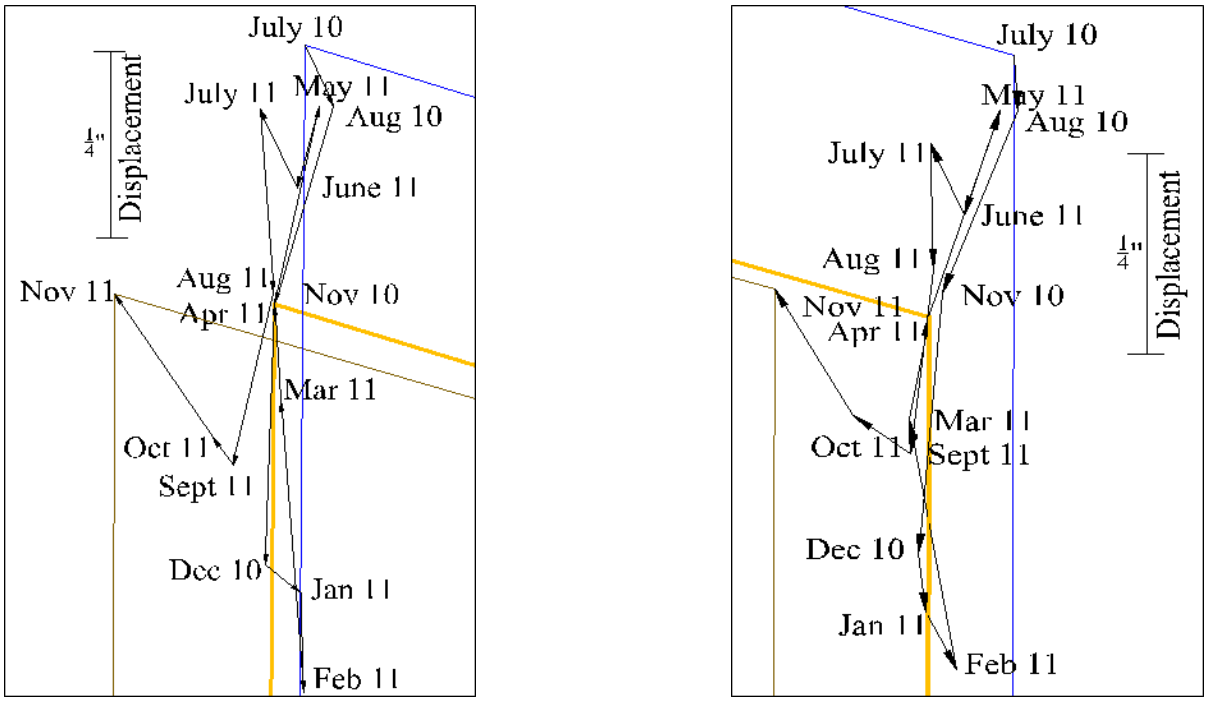

Figure 6.81. Bridge 309 movement at north abutment west and east reflectors

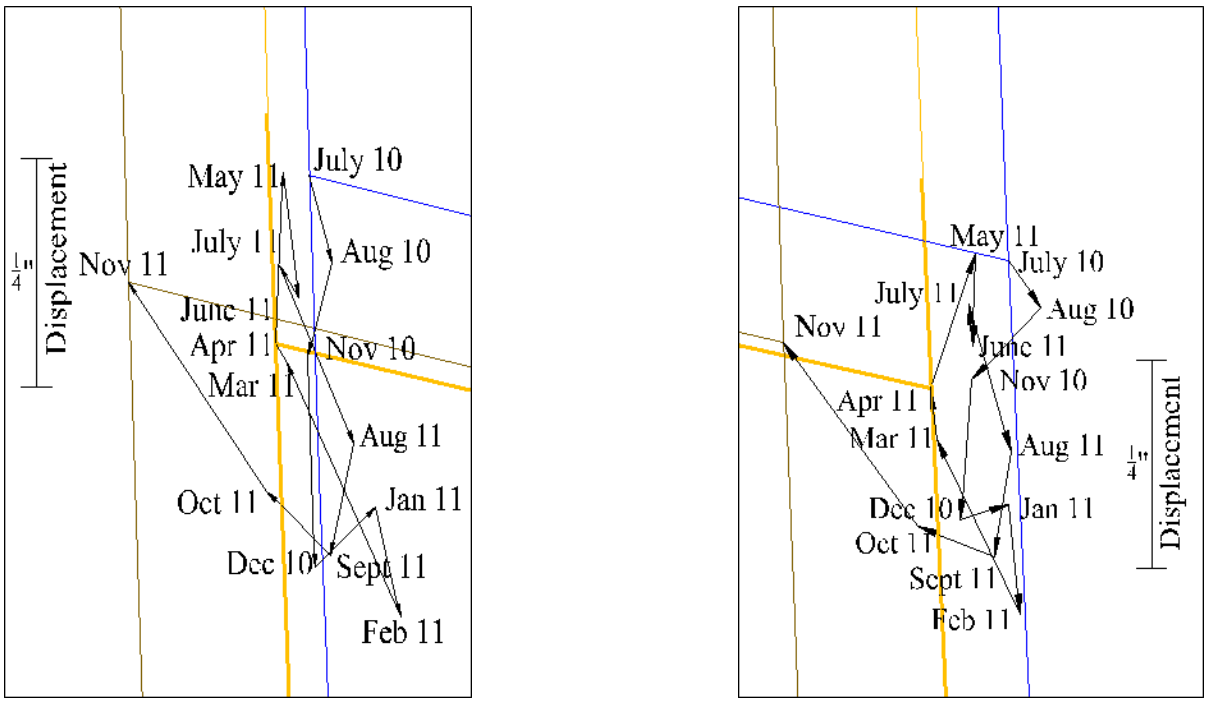

Figure 6.82. Bridge 309 movement at north pier west and east reflectors

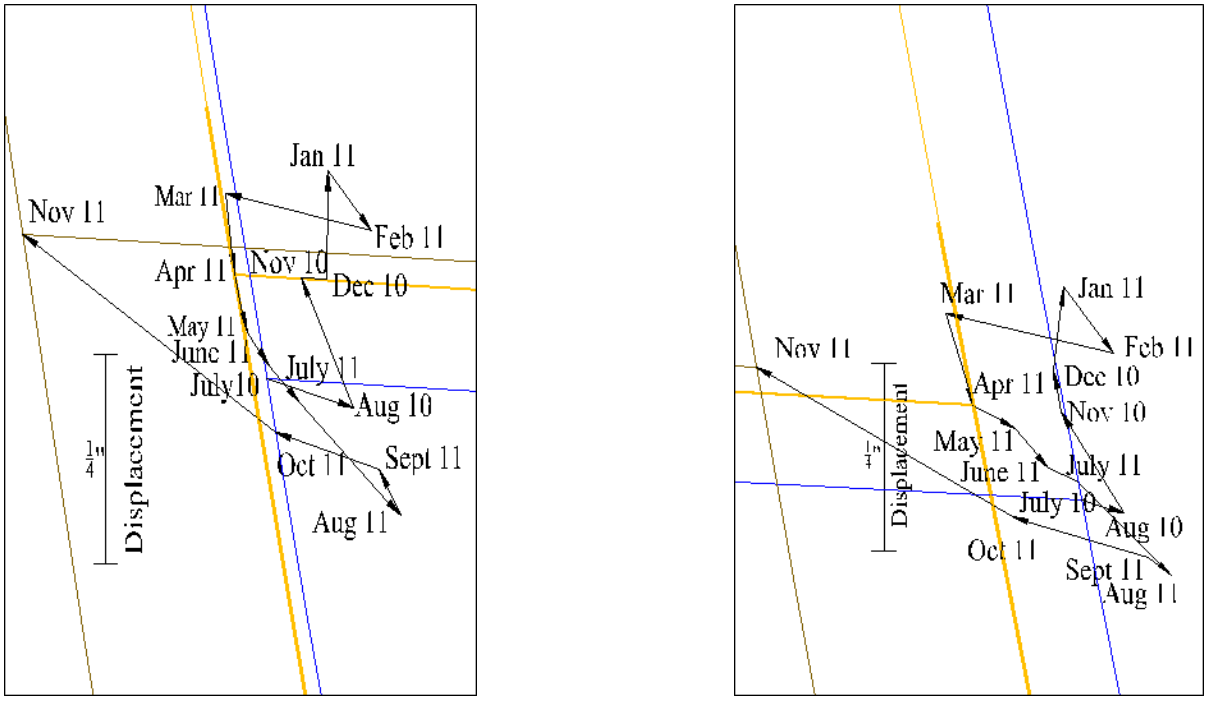

Figure 6.83. Bridge 309 movement at south pier west and east reflectors

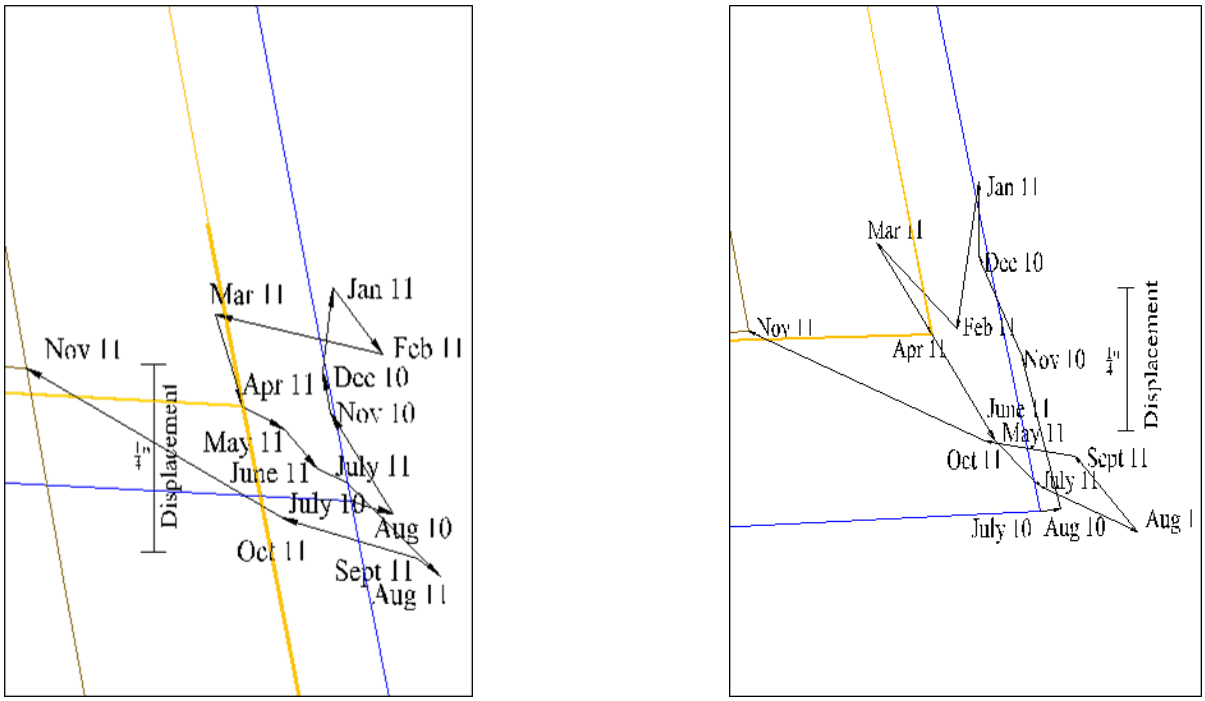

Figure 6.84. Bridge 309 movement at south abutment west and east reflectors

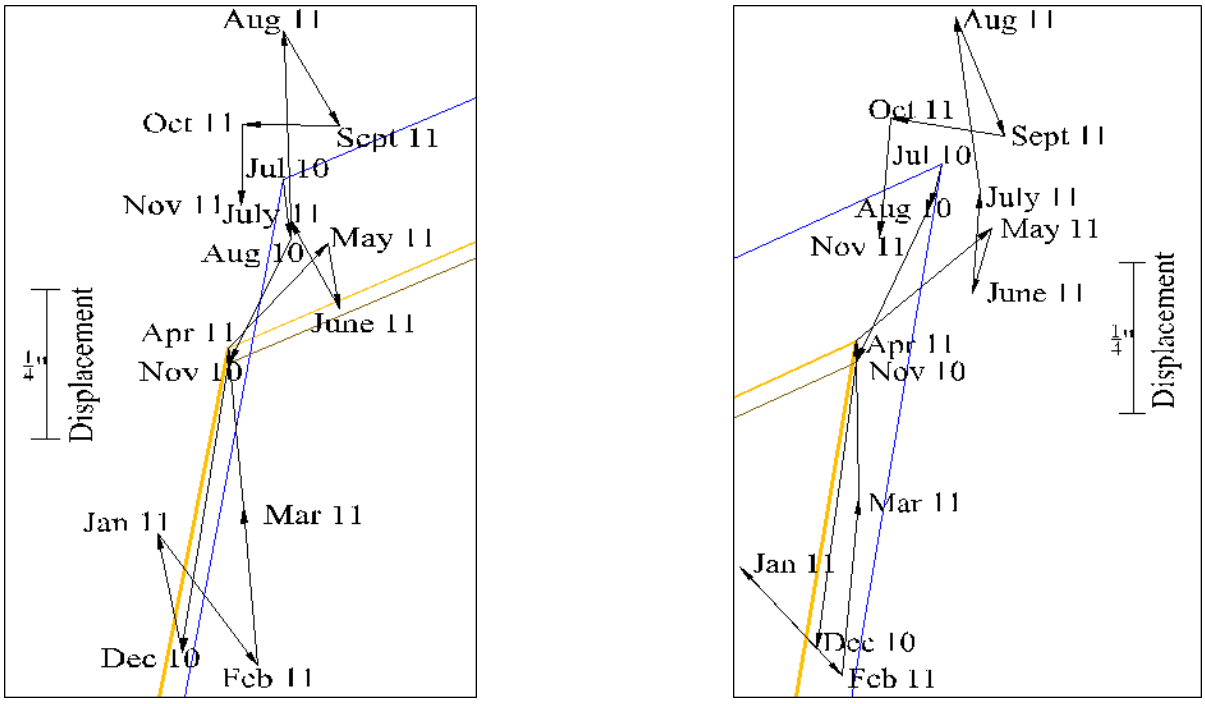

Figure 6.85. Bridge 2208 movement at north abutment west and east reflectors

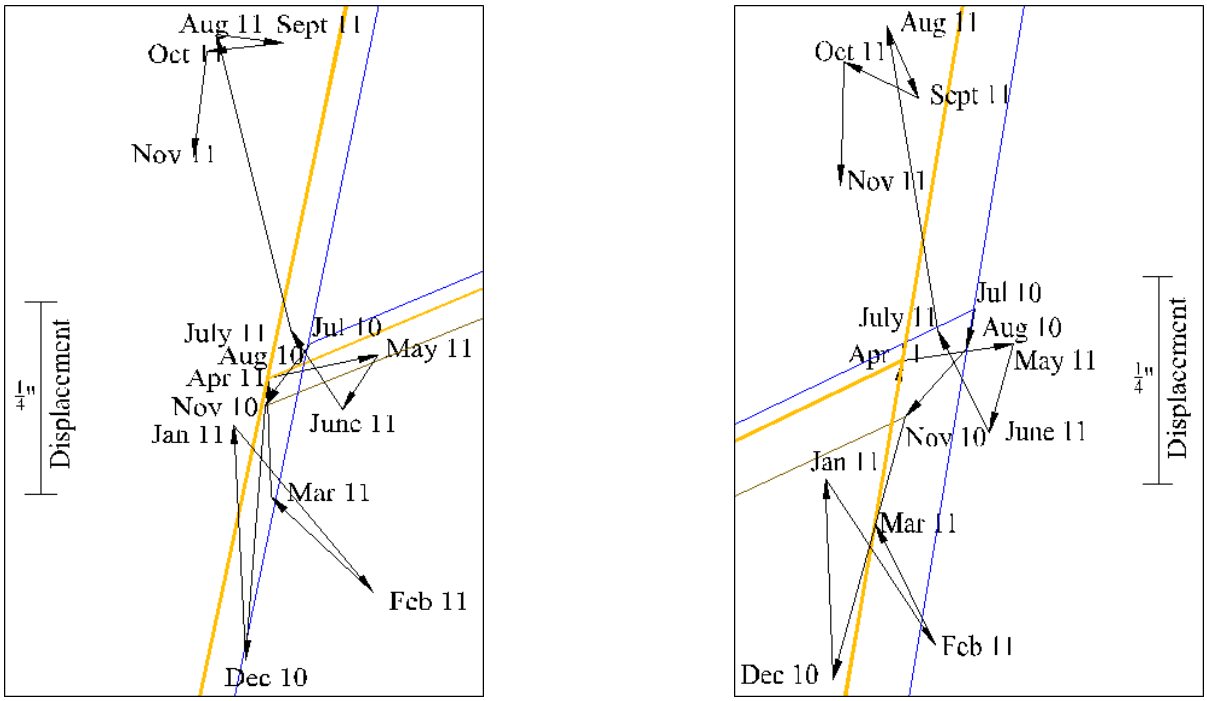

Figure 6.86. Bridge 2208 movement at north pier west and east reflectors

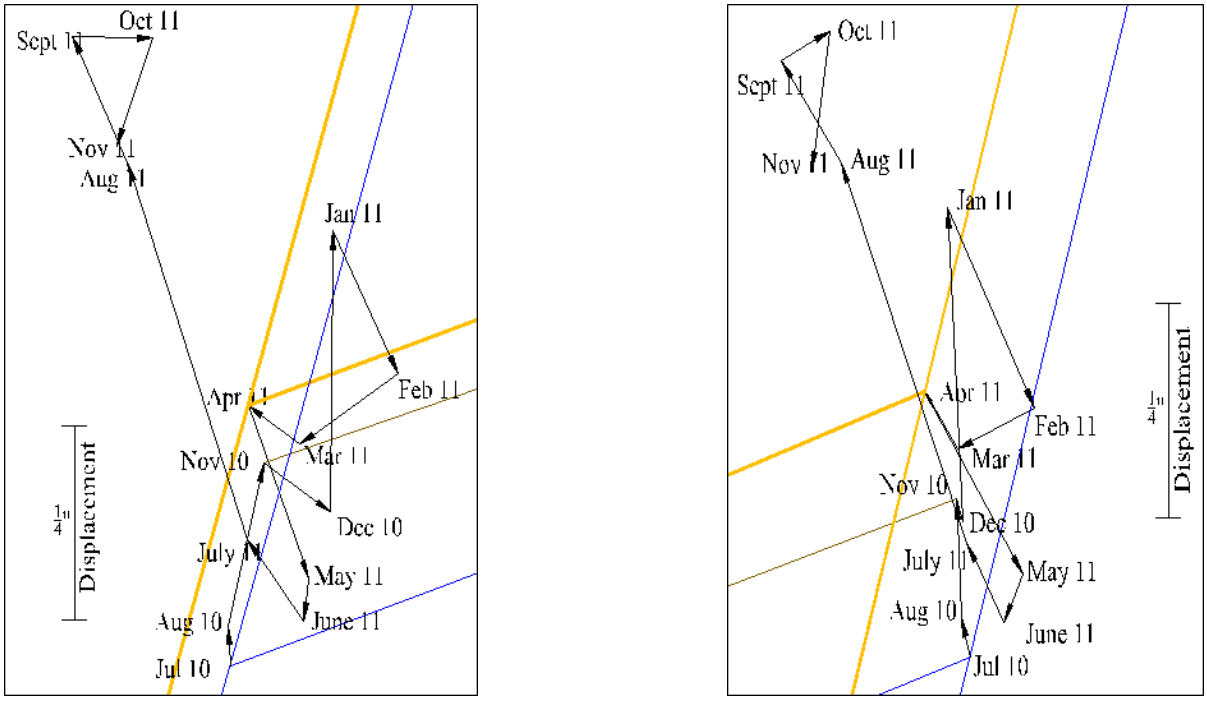

Figure 6.87. Bridge 2208 movement at south pier west and east reflectors

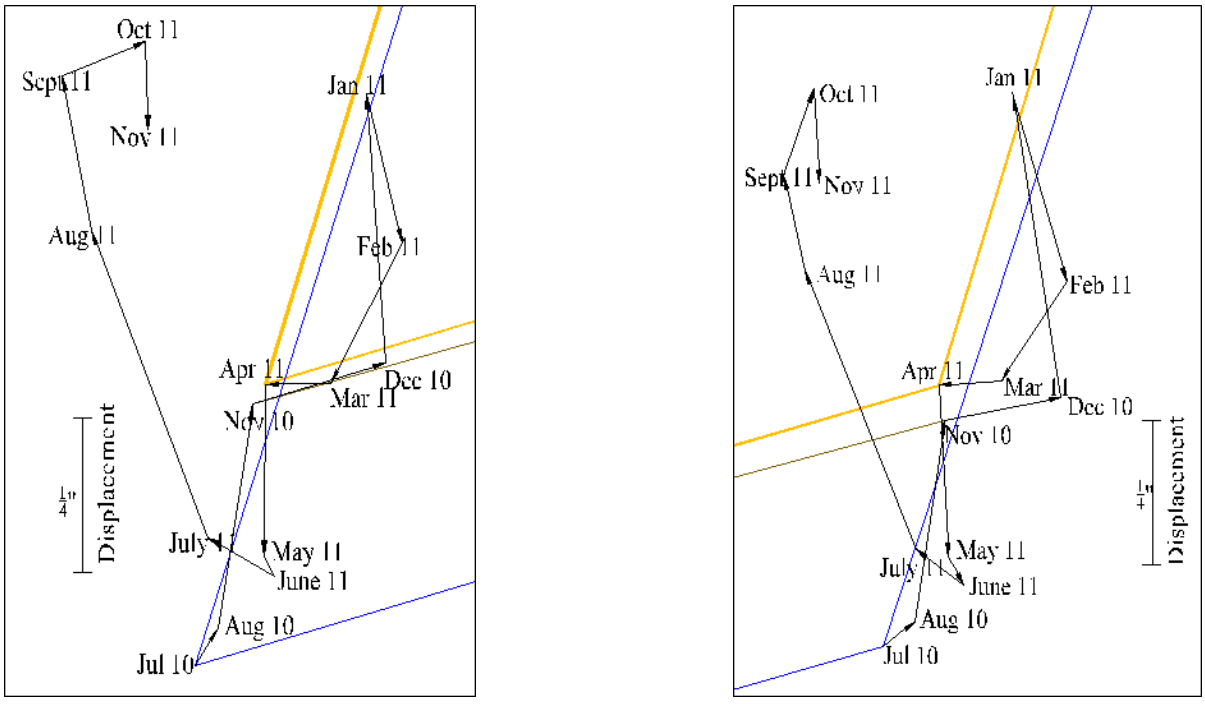

Figure 6.88. Bridge 2208 movement at south abutment west and east reflectors

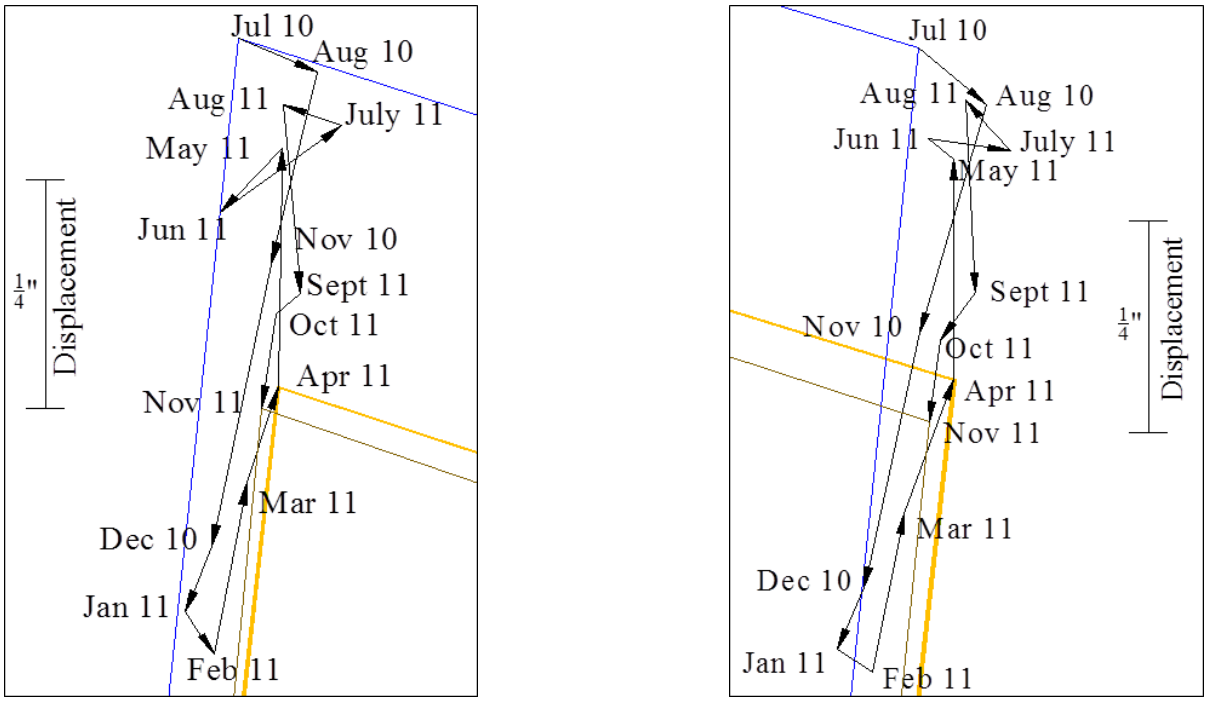

Figure 6.89. Bridge 2308 movement at north abutment west and east reflectors

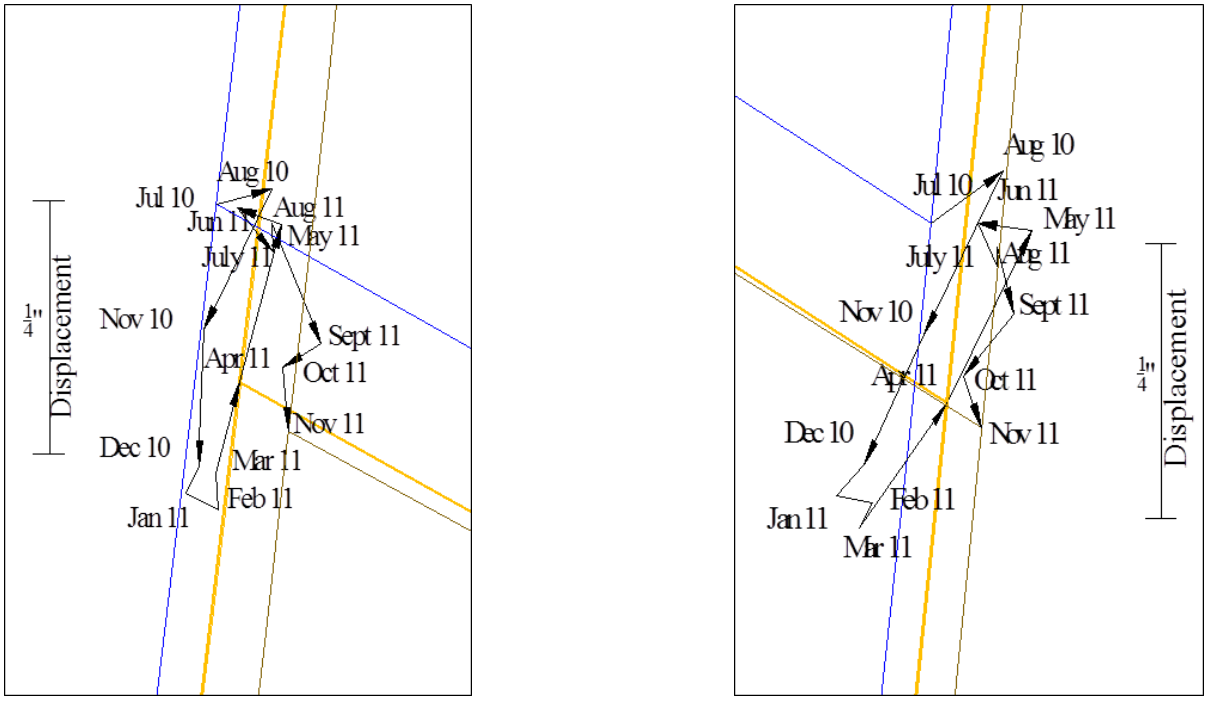

Figure 6.90. Bridge 2308 movement at north pier west and east reflectors

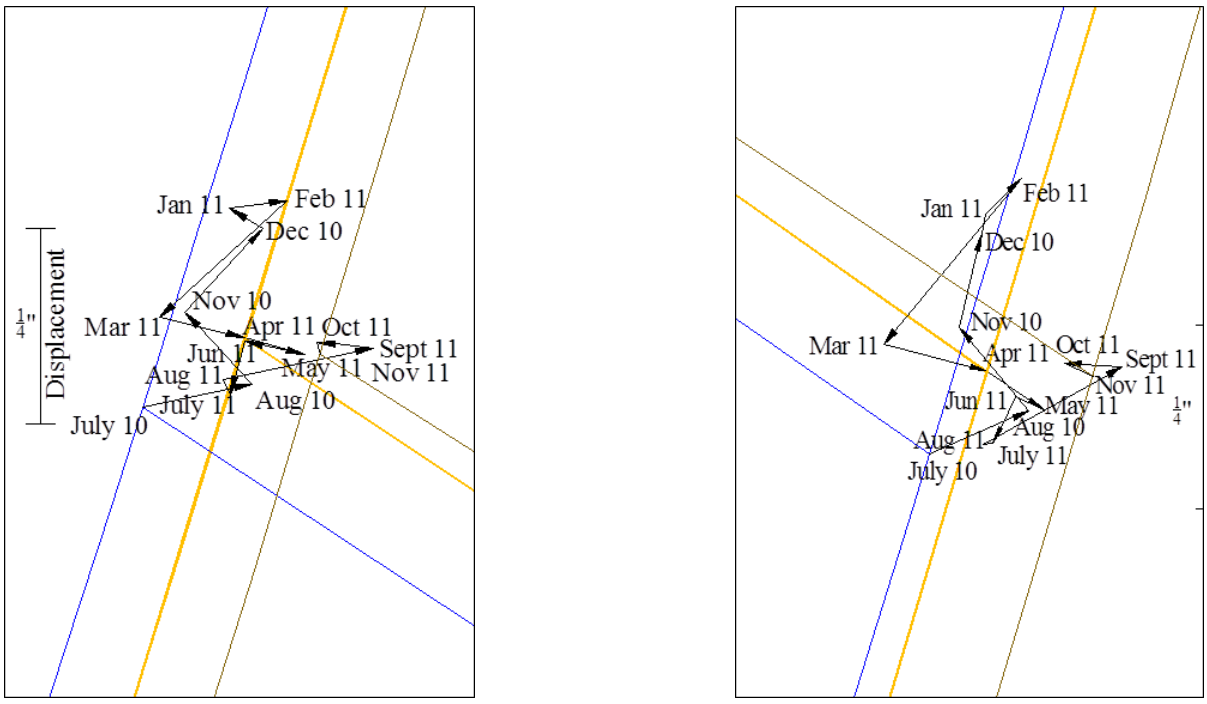

Figure 6.91. Bridge 2308 movement at south pier west and east reflectors

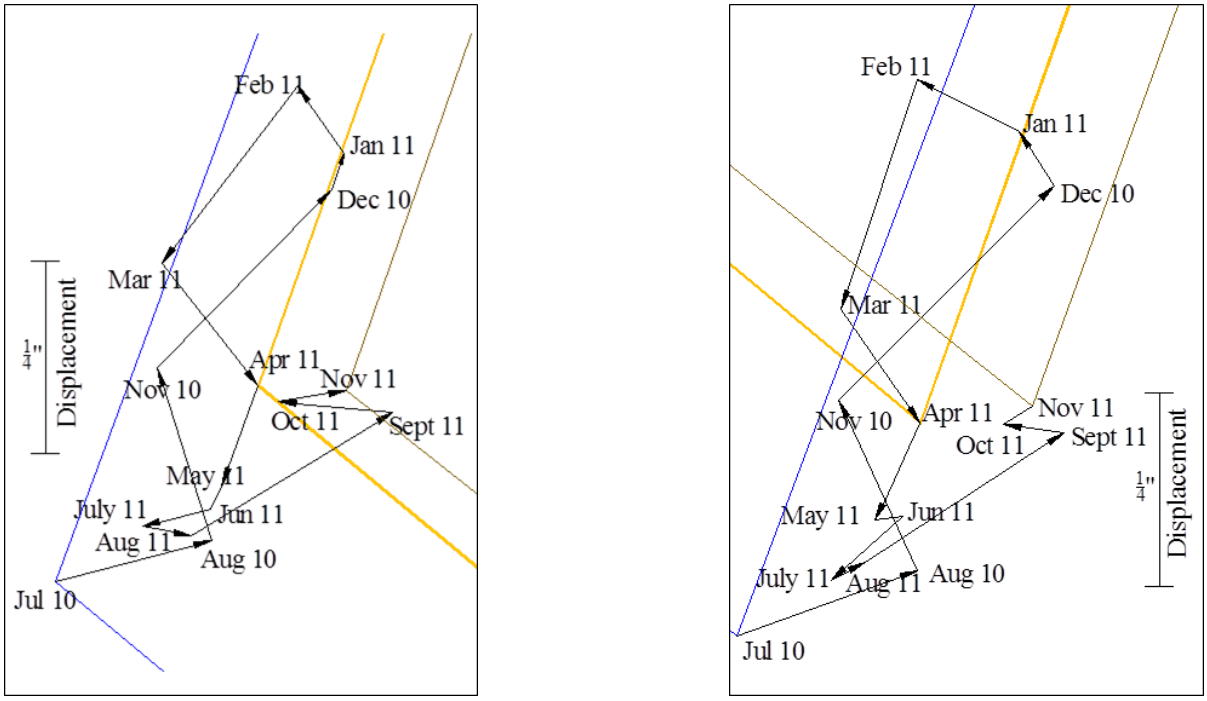

Figure 6.92. Bridge 2308 movement at south abutment west and east reflectors

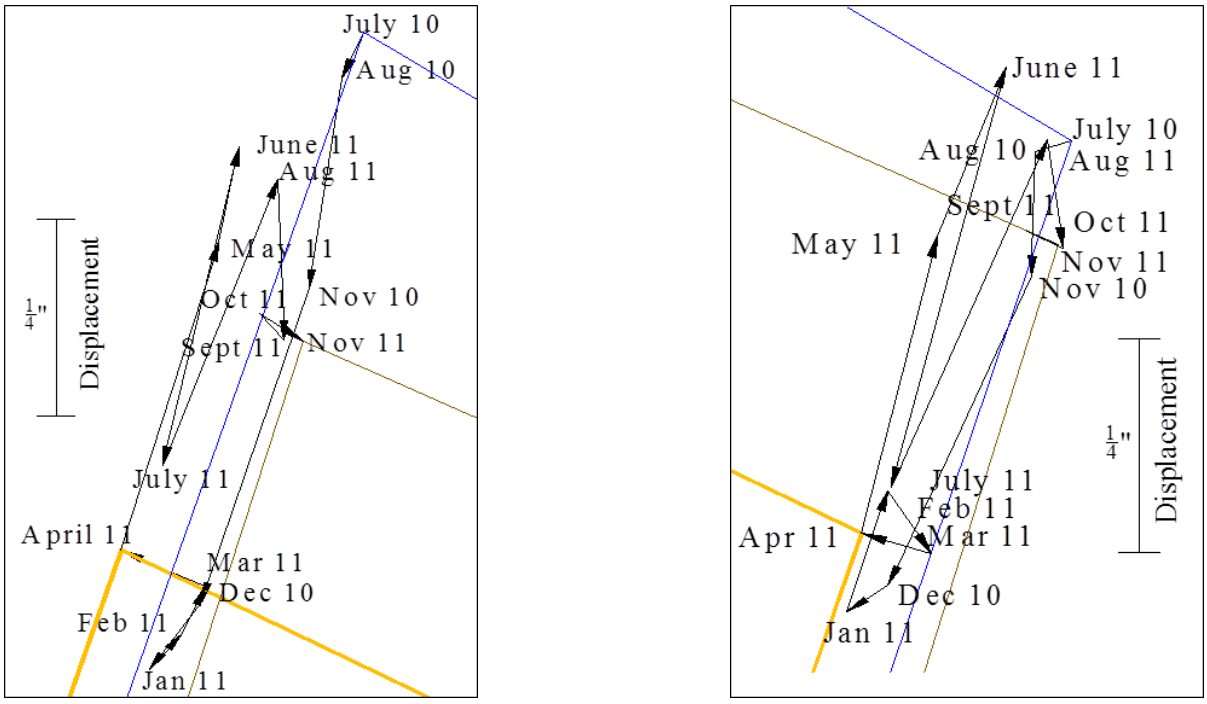

Figure 6.93. Bridge 2408 movement at north abutment west and east reflectors

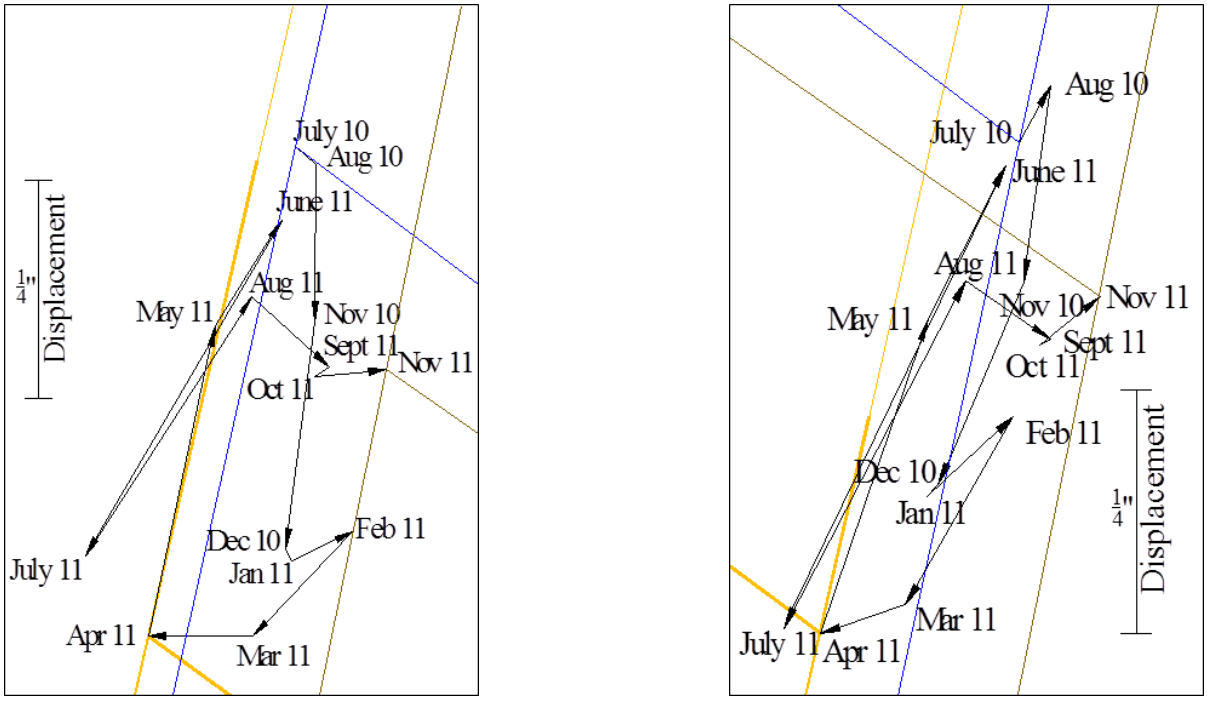

Figure 6.94. Bridge 2408 movement at north pier west and east reflectors

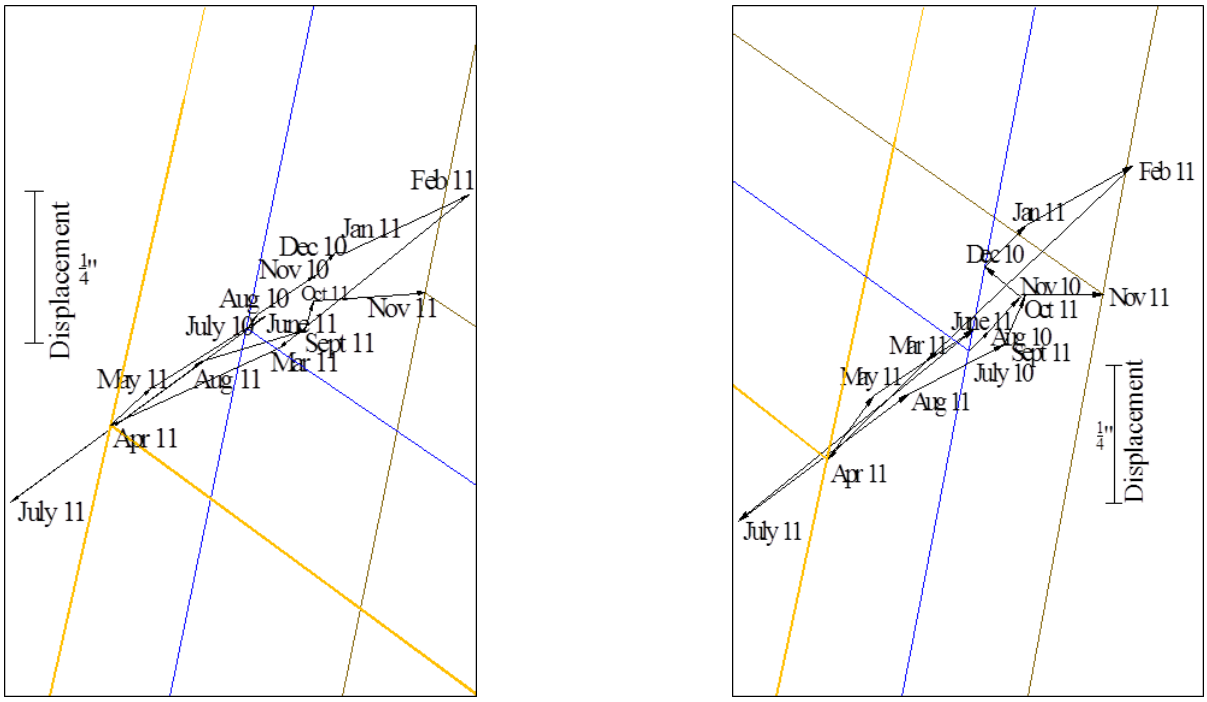

Figure 6.95. Bridge 2408 movement at south pier west and east reflectors

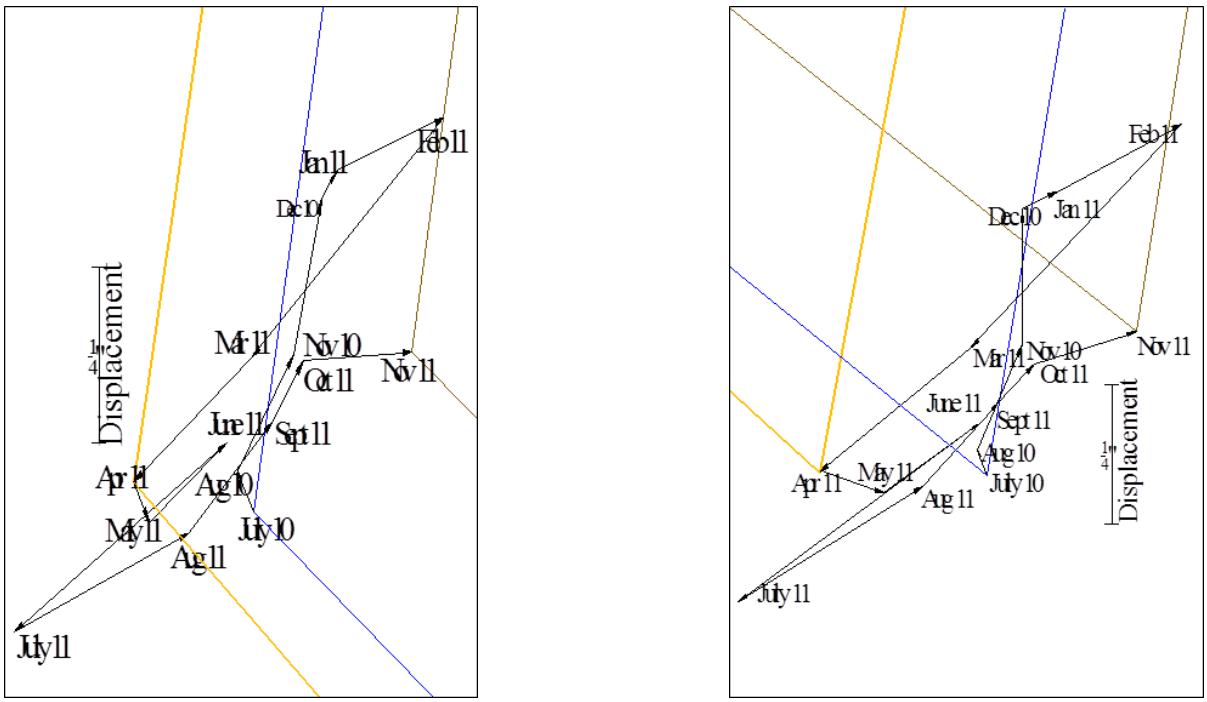

Figure 6.96. Bridge 2408 movement at south abutment east and west reflectors

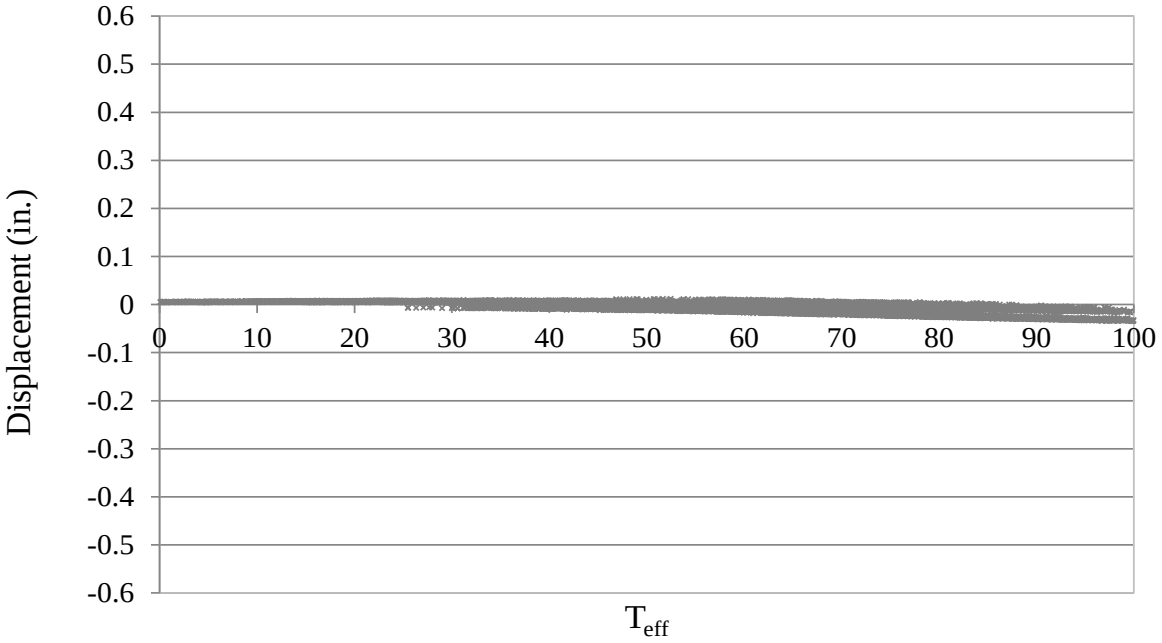

Figure 6.97. Bridge 109 relative displacement between fixed pier and Girder B

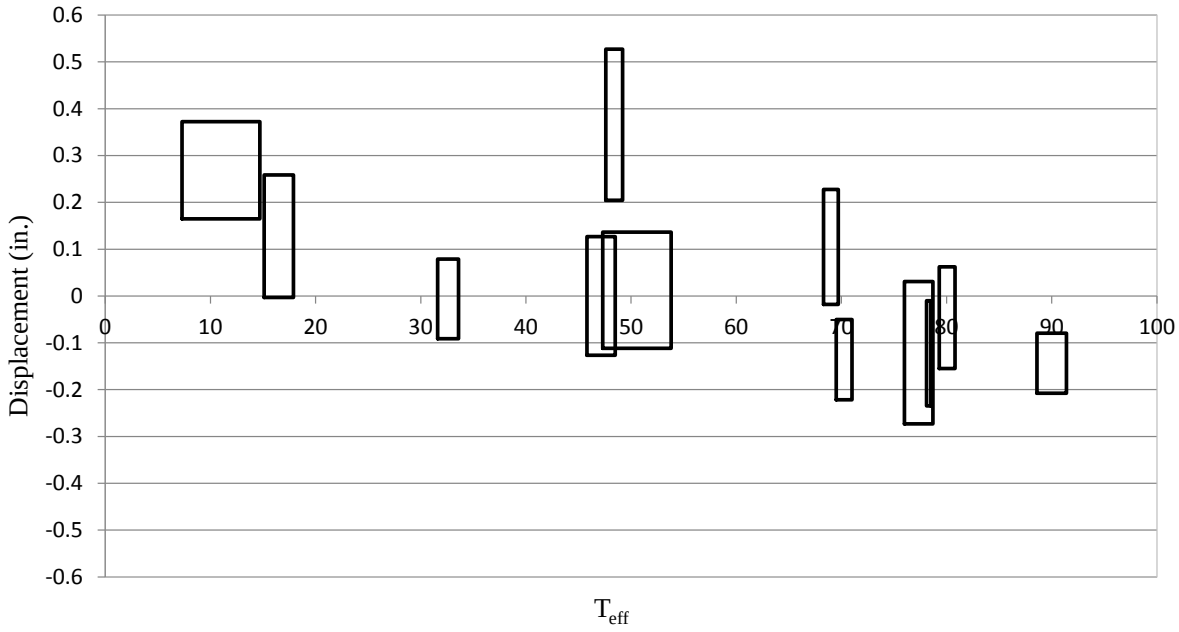

Figure 6.98. Absolute movement of bottom flange of Girder B at north pier reflector

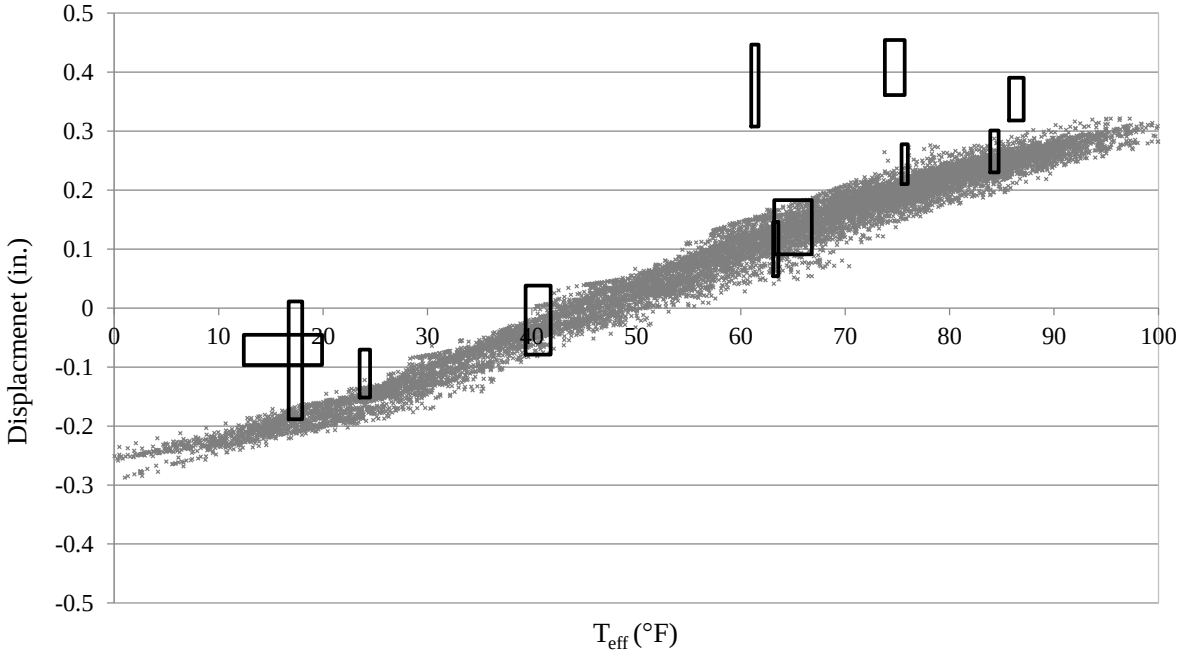

Figure 6.99. Expansion pier displacement

6.3.2 Steel Pile Behavior

Equivalent Cantilever Model

The equivalent cantilever analytical model shown in Figure 6.100 attempts to estimate the weak axis bending moment in an integral abutment steel pile (Abendroth 2005). In the model, the steel pile is idealized as an isolated column with an equivalent length, L, and rotationally fixed ends.

Equation 6.32 describes the relationship between the applied displacement, Δ, and the resulting end moment, M.

$$M = \frac{\Delta 6EI}{L_e^2} \tag{6.32}$$

Assuming a linear moment diagram for the pile because no intermediate forces exist, the end moment M can be calculated from Mg by Equation 6.33.

$$M = \frac{M_g L_e}{L_g} \tag{6.33}$$

The relationship between weak axis bending moment at the location of the strain gauges, M_g, and the weak axis bending strain at the location of the strain gauges, ε_g, is given by Equation 6.34.

$$\varepsilon_g = \frac{M_g c}{EI} \tag{6.34}$$

By combining Equation 6.32 through 6.34, the weak axis bending strain at the location of the strain gauges can be expressed by Equation 6.35.

$$\varepsilon_g = \frac{\Delta 6 L_g c}{L_e^3} \tag{6.35}$$

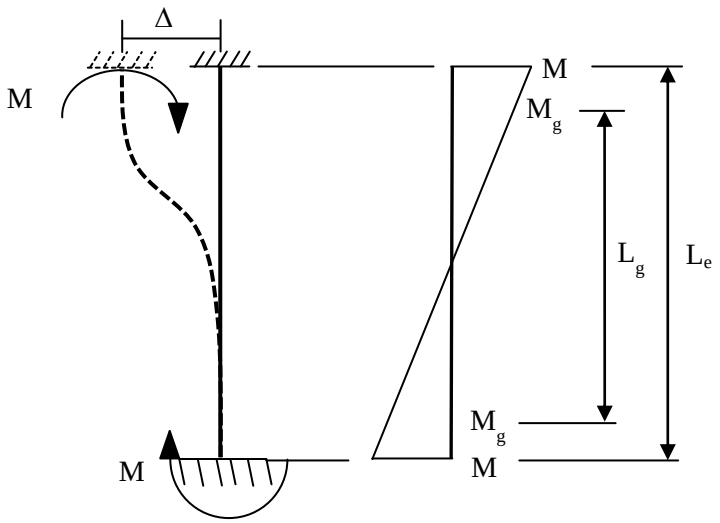

Figure 6.100. Equivalent cantilever pile model

where,

Δ = applied lateral end displacement,

M = resulting end moment,

M_g = resulting moment at location of strain gauges

L_e = equivalent cantilever length, and

Lg = distance between equivalent Mg moments

Pile Expansion

Figures 6.101 through 6.106 show the weak axis bending strain versus displacement for the six instrumented piles of Bridge 309. The data in the figures come from the survey data and from the pile strain gauge data. Each rectangle in the figures represents a survey date. The horizontal sides of the rectangle represent the 95% confidence interval of pile displacement, at the top of the pile, for a given survey date. The vertical sides of the rectangle represent the change in the measured microstrain in the pile during the life of the respective survey, at the location of the strain gauge. The solid, diagonal lines represent the theoretical relationship between pile displacement and microstrain calculated using the analytical cantilever method. Based on the soil conditions shown in the bridge plan set and following the work of Abendroth and Greimannan equivalent cantilever length of 18 ft was calculated. From there, an approximate relationship between pile expansion and internal weak axis bending strain was plotted alongside the measured results.

In each of the figures there are a couple survey months that show conflicting results with the rest of the data. One of the months has a very large confidence interval and two of the months show displacement without any resulting strain. These results have been unexplainable except for errors in the electronic and/or survey data.

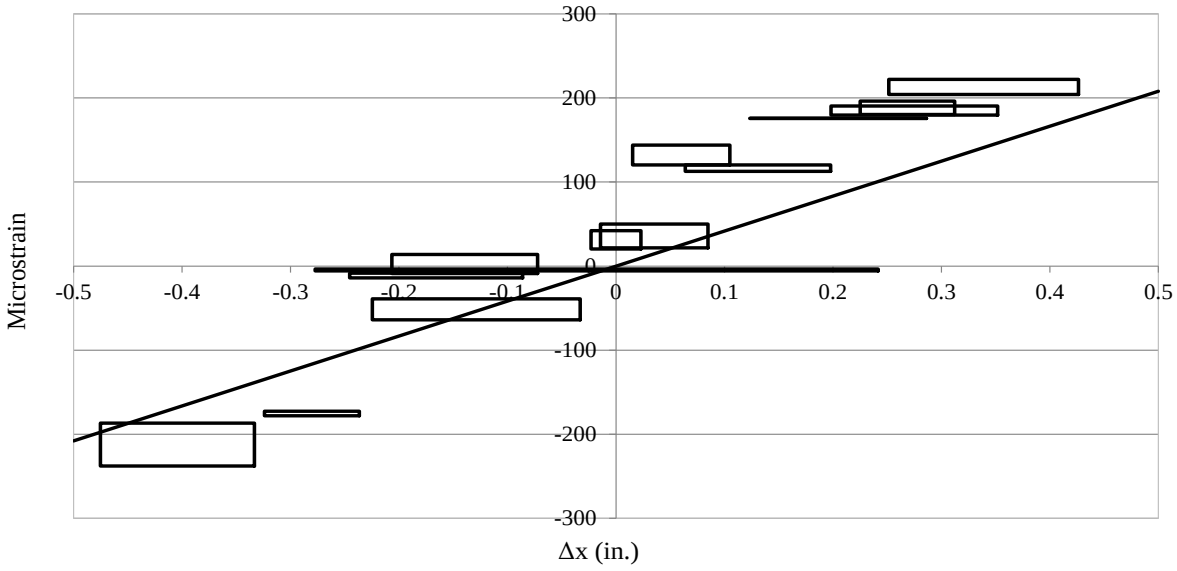

Figure 6.101. Weak axis bending strain vs. displacement SAHP1

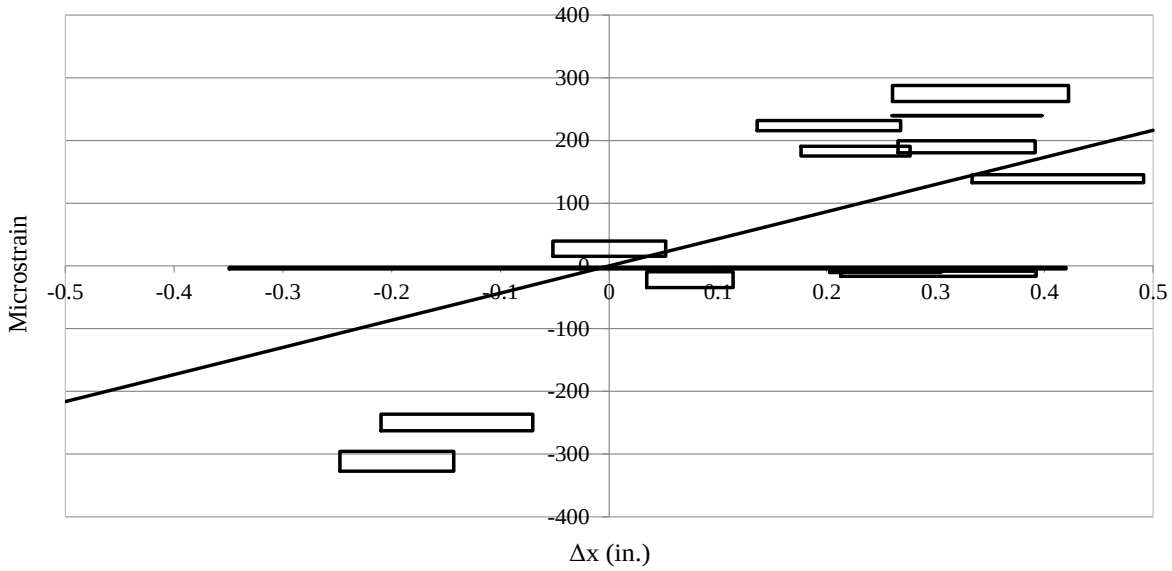

Figure 6.102. Weak axis bending strain vs. displacement SAHP4

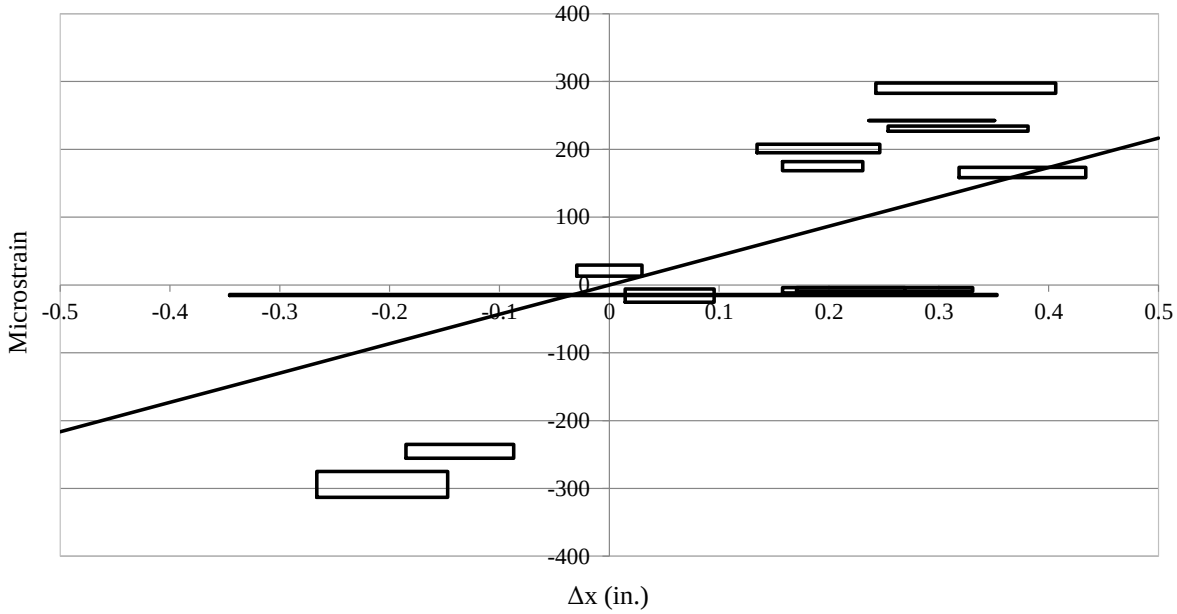

Figure 6.103. Weak axis bending strain vs. displacement SAHP6

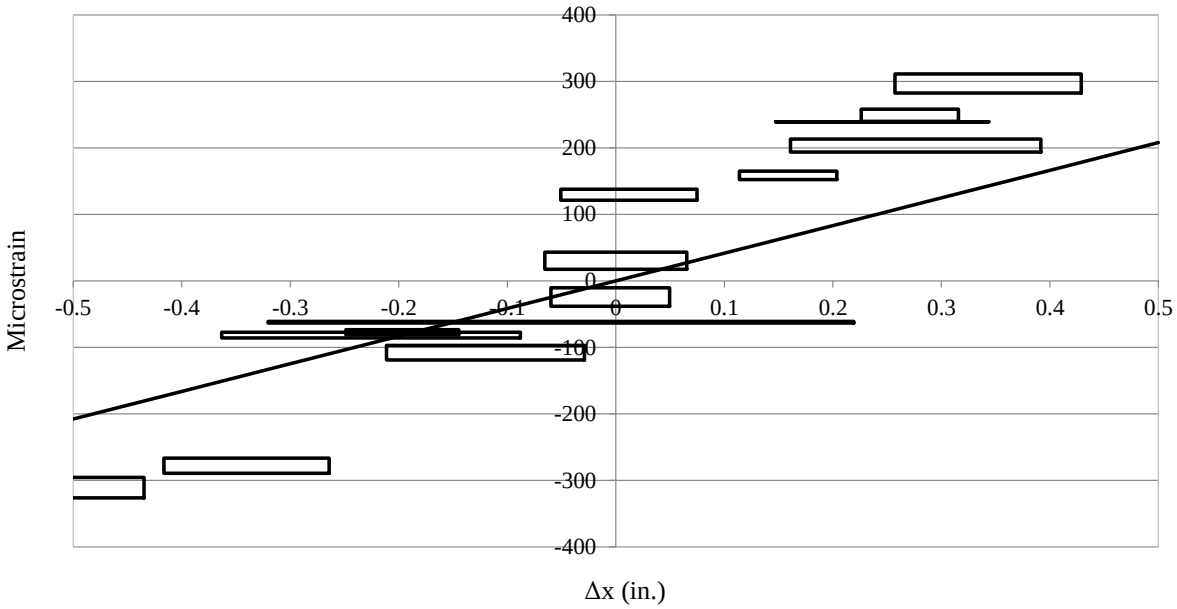

Figure 6.104. Weak axis bending strain vs. displacement NAHP1

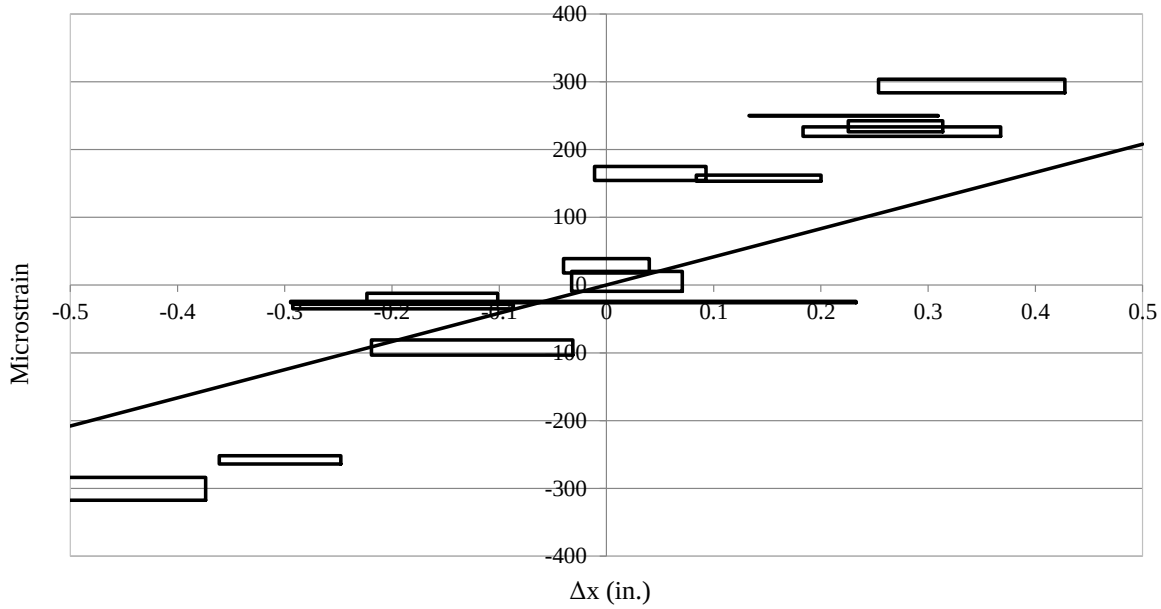

Figure 6.105. Weak axis bending strain vs. displacement NAHP4

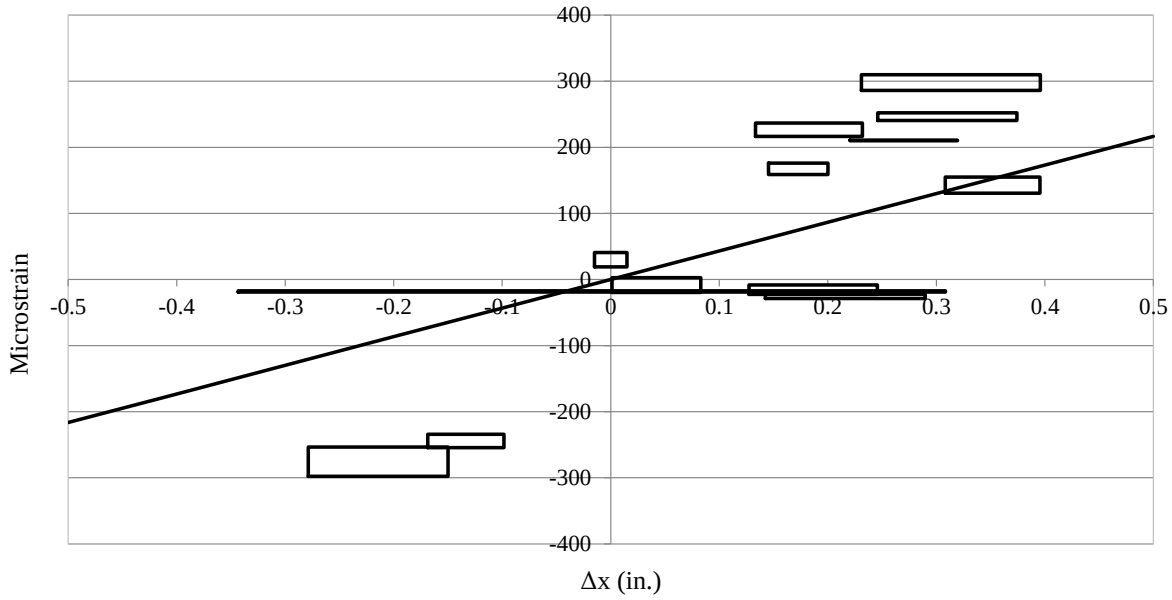

Figure 6.106. Weak axis bending strain vs. displacement NAHP6

Based on the figures it appears that the analytical cantilever model was a better predictor of stress vs. displacement for the HP1 piles, the piles closest to the outside curve. The equivalent length was too large to accurately reflect the measured results of the HP4 and HP6 piles, at both abutments. The equivalent length is directly related to the pre-bored depth of each pile as well as the soil conditions surrounding the piles. As a result, there are a number of explanations as to why the equivalent length was artificially large, none of which the research team could definitely narrow down.

CHAPTER 7 DIFFERENTIAL ABUTMENT PILE AXIAL LOAD INVESTIGATION

The purpose of this chapter is to investigate the behavior of an integral abutment under an internal temperature gradient and the resulting effects on the abutment pile axial loads. One abutment from the empirical study was modeled using the finite element software package ANSYS 12.1. A temperature gradient was applied to the models abutment and the resulting pile axial loads were recorded and compared. Recommendations for future work follow.

7.1 BACKGROUND

Data recorded during the monitoring period of this work has shown some inconsistencies in the internal axial strains in the piles. Figure 7.1 and 7.3 show the internal axial strains versus effective bridge temperature of the three instrumented piles at Bridge 309's south abutment. In the figure the grey data is the strain-gauge data recorded during the project lifecycle, and the dashed, black line is the linear best-fit line for the data.

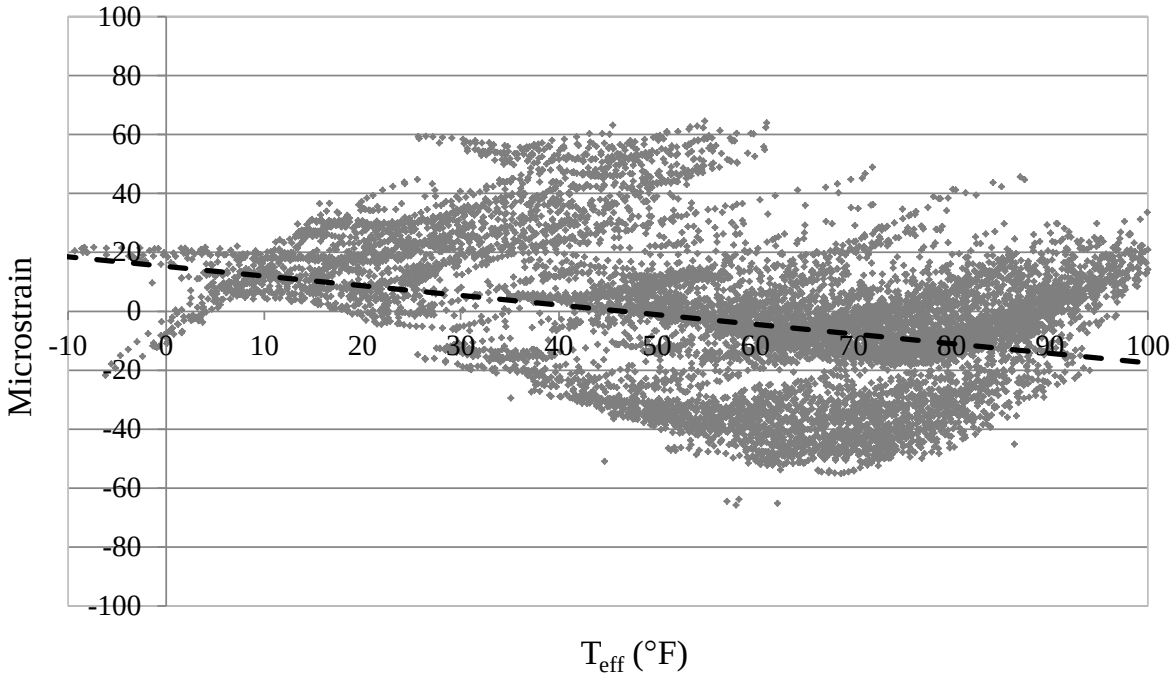

Figure 7.1. SAHP1 axial strain vs. effective bridge temperature

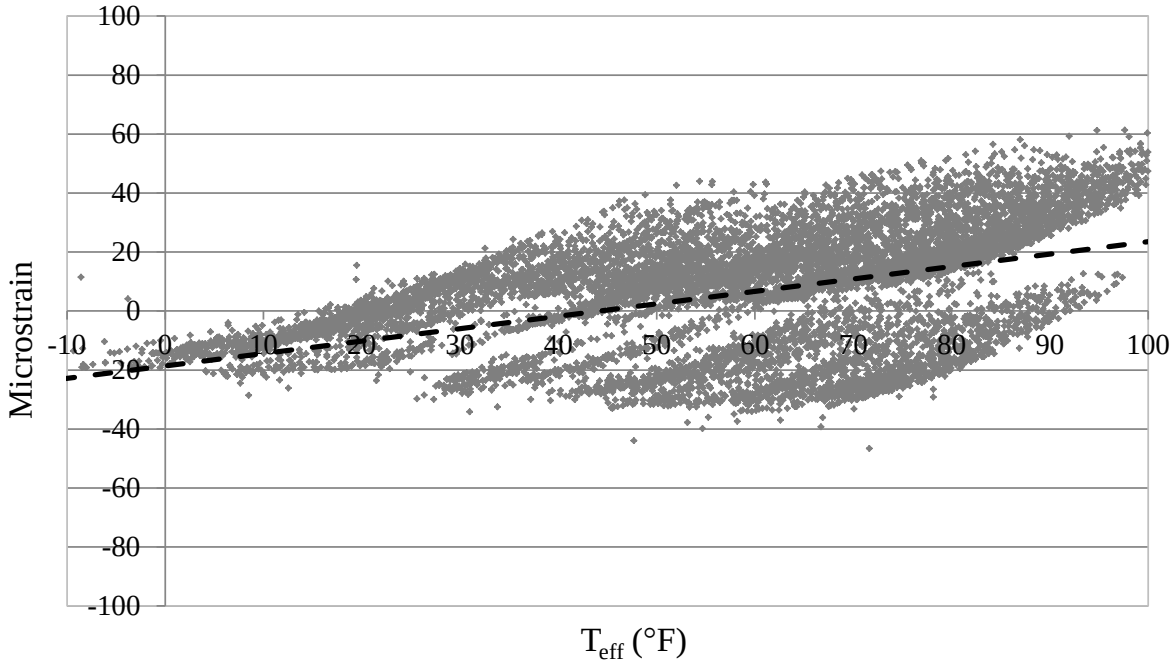

Figure 7.2. SAHP4 axial strain vs. effective bridge temperature

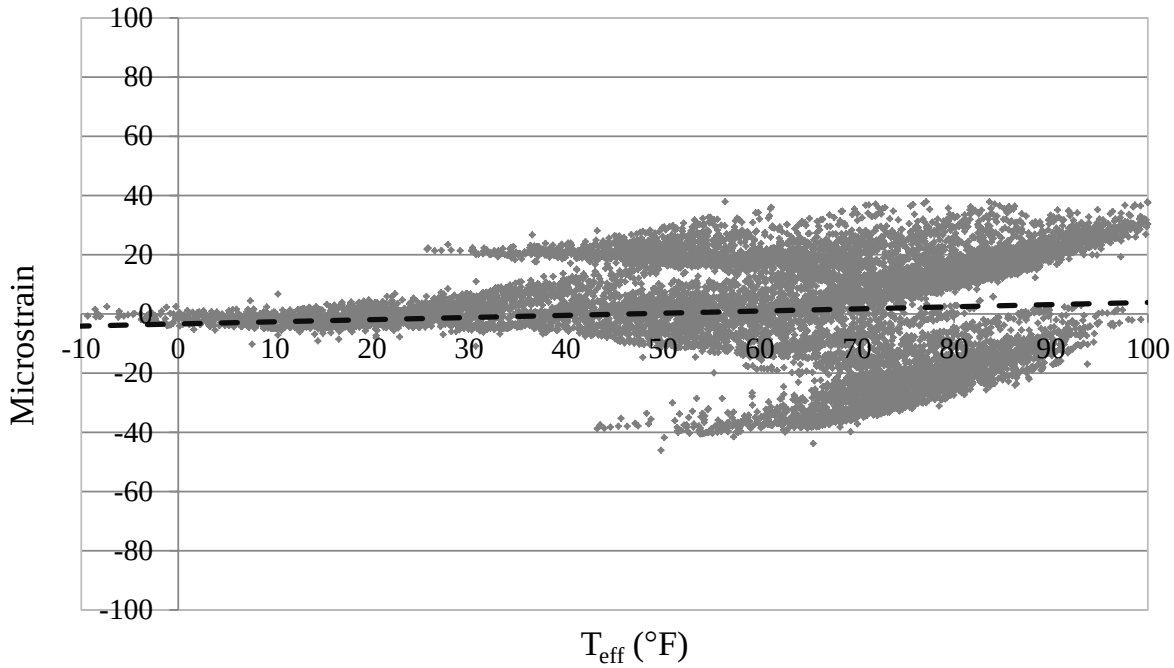

Figure 7.3. SAHP6 axial strain vs. effective bridge temperature

As shown in Figure 7.1 through 7.3, the best fit lines that describe each data set have

unique slopes. At higher effective bridge temperatures the interior pile, SAHP4, is showing higher (higher tension) axial strains than the exterior piles, SAHP1 and SAHP6. The opposite is true at lower bridge temperatures where the interior pile shows lower (higher compression) axial strains than the exterior piles.

In order to estimate the temperature gradient in the abutment, the temperatures record by the embedded concrete deck temperature gauges and the abutment pile strain-gauges were plotted for a hot period and a cold period. The difference between the deck temperature data and the pile strain-gauge temperature was then used as an input in the ANSYS analysis. Figure 7.4 shows the temperature data from the previously mentioned gauges for the warm period. The temperature differential from the cold period was nearly equal to the warm period.

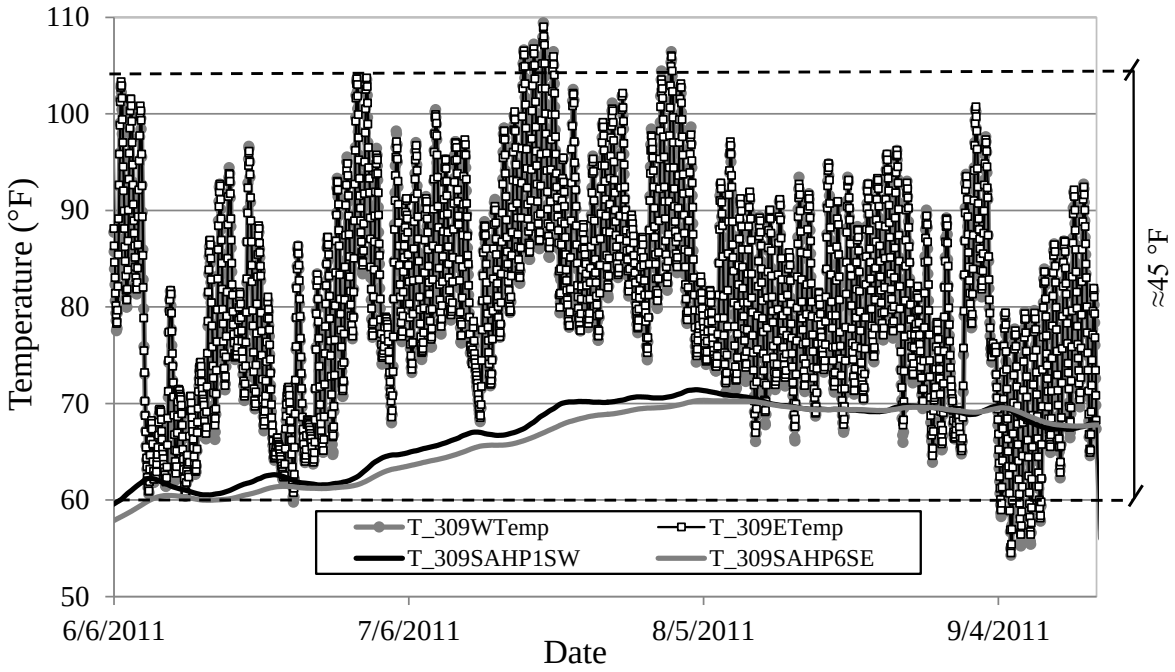

Figure 7.4. Temperature data

As Figure 7.4 shows, during a hot period the temperature at the pile strain-gauges typically remains cooler compared to the embedded concrete deck gauges. Assuming the bottom of the abutment acts in a similar manner a temperature gradient through the abutment

would result. The largest difference between the two gauge locations as shown in the figure is approximately 45 °F.

7.2 MODEL DEVELOPMENT

7.2.1 Geometry

The model design for the analysis has geometry similar to Bridge 309's south abutment. The analytical model's abutment top and bottom elevations, the pile locations, and the pilecap and backwall thicknesses are the same as Bridge 309's south abutment. Figure 7.5 through 7.7 depict the geometry of the analytical model.

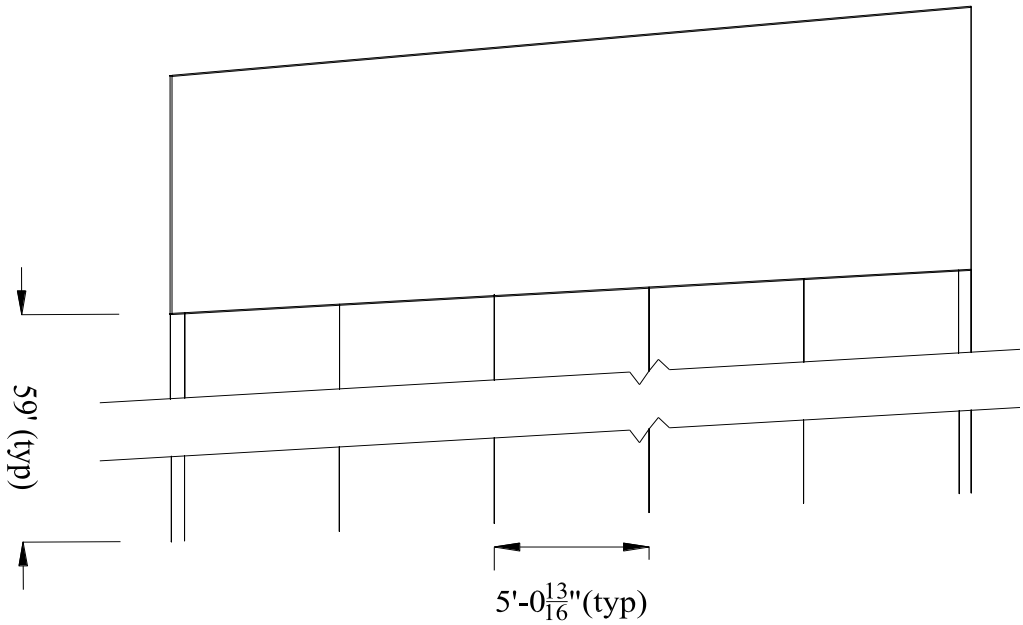

Figure 7.5. Analytical model elevation view

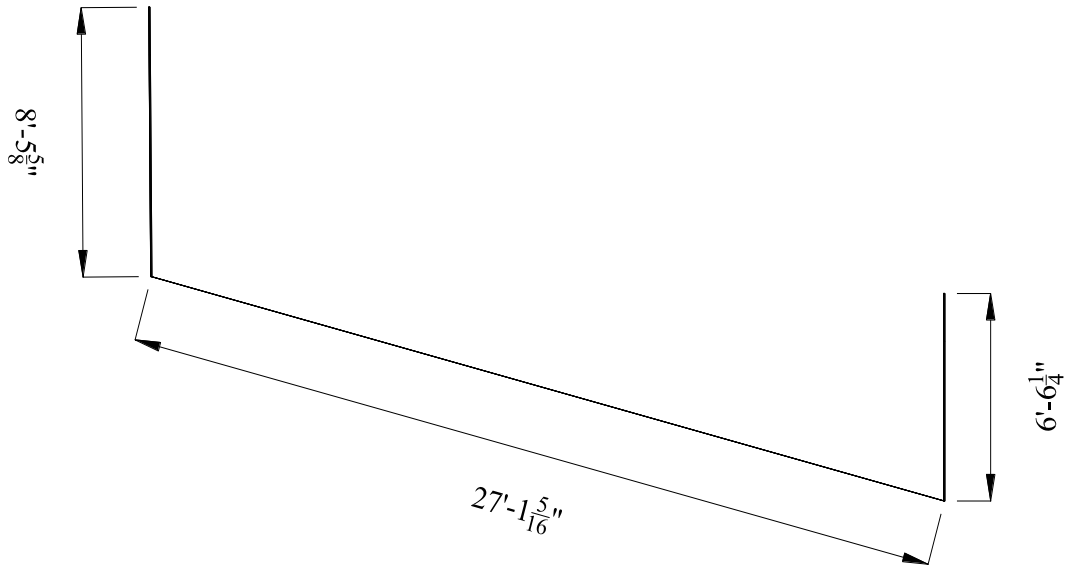

Figure 7.6. Analytical model plan view

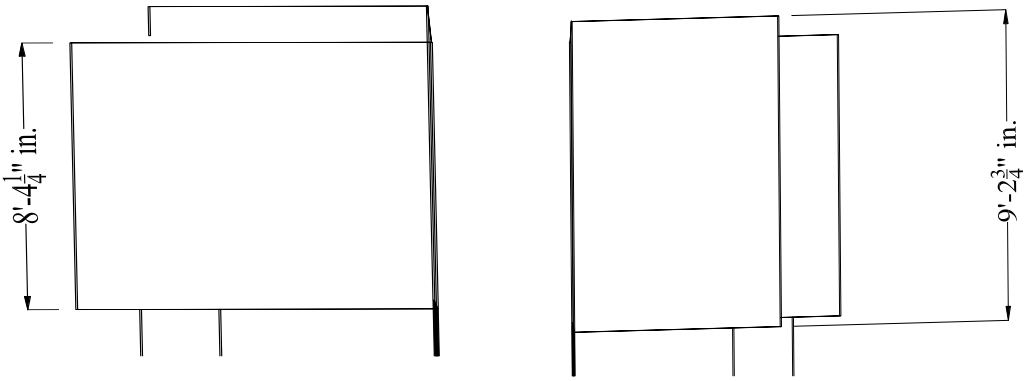

Figure 7.7. Analytical model end views

As shown in Figure 7.5 through 7.7, in order to simplify the design, in the analytical model the wingwalls are extended the full height as the abutment backwall and the thickness of the abutment is a constant 36 in. (defined in shell element properties). Also, the portion of the wingwall that extends forward past the backwall, regarding Bridge 309's abutment, was not included in the analytical model.

7.2.2 Elements

SHELL57

SHELL57 is a 3-D thermal shell element having in-plane thermal conduction capability. The element was used to mesh the abutment during the thermal conduction portion of the analysis. In this analysis, the element geometry was defined by four nodes, a constant thickness, and the material properties. At each node there is a single degree of freedom; temperature. This element is applicable to a 3-D steady-state or transient thermal analysis.

SHELL63

SHELL63 is a 3-D elastic shell element that has both bending and membrane capabilities. This element was used to mesh the abutment during the thermal stress portion of the analysis. In this analysis, the element geometry was defined by four nodes, a constant thickness, and the orthotropic material properties. There are six degrees of freedom at each node: translations in the nodal x, y, and z directions and rotations about the nodal x, y, and z axes. Both in-plane and normal loads are permitted.

BEAM4 3-D

BEAM4 is a uniaxial 3-D elastic beam element with tension, compression, torsion, and bending capabilities. This element was used to model the abutment piles and the composite girders during the thermal stress portion of the analysis. In this analysis, the element was defined by two nodes, the cross-sectional area, two area moments of inertia (IZZ and IYY), two thicknesses (TKY and TKZ), an angle of orientation (θ) about the elements x-axis, the torsional moment of inertia (IXX), and the material properties. At each node the element has six degrees of freedom: translations in the nodal x, y, and z directions and rotations about the nodal x, y, and z axes.

COMBIN14

COMBIN14 is a spring-damper element that has longitudinal or torsional capability in 1-D, 2-D, or 3-D applications. This element was used to model the soil skin friction along the length of the piles during the thermal stress portion of the analysis. In this analysis, the element was defined by two nodes and a spring constant (k). The longitudinal spring-damper option is a uniaxial tension-compression element with up to three degrees of freedom at each node: translations in the nodal x, y, and z directions. No bending or torsion is considered. The

spring-damper element has no mass, and the spring or the damping capability may be removed from the element. Since only soil skin friction was considered, the element was restrained so that only one degree of freedom was free, parallel to the piles.

7.2.3 Material Properties

Abutment

In order to run the thermal conduction and thermal stress analyses certain assumptions had to be made about the thermal and structural properties of the concrete abutment. The modulus of elasticity of the concrete, E_c, was estimated using the recommendations of ACI 318-08 section 8.5.1. The concrete's poisson ratio, ν_c; density, ρ_c; specific heat, C_{pc}; thermal conductivity, k_c; and coefficient of linear thermal expansion,α_c; were selected from appropriate charts (The Engineer ToolBox 2012). Table 7.1 shows the concrete thermal properties that were inputted into ANSYS 12.1.

Table 7.1. Abutment material properties ANSYS model

E_c (psi)	ν_c	ρ_c (lb/in.^{3})	C_{pc} (Btu/lb$_m$°F)	k_c (BTU/(in.hr.°F)	α_c (10^{-6} in./in. °F)
3,372,165	0.15	0.086806	0.2	0.03	5.5

The values shown in Table 7.1 were assumed values for the given material properties. These estimates should provide sufficient results for the scope of the analysis.

Piles and Composite Girders

Since the piles and composite girders are excluded from the thermal conductivity portion of the analysis, only structural properties of members are needed for the analysis. The material and cross-sectional properties of the composite girders discussed previously were used in the model. The modulus of elasticity, E_s, and poisson ratio, ν_s, for the steel piles were assumed equal to 29,000,000 psi and 0.3, respectively.

Soil

In order to model vertical soil springs it was necessary to make certain assumptions about the properties of the soil surrounding the piles. Using the boring log provided in Bridge 309's plan set and Table 5.5 from Abendroth and Greimann (2005) the average soil blow count, N; undrained cohesion, C_u; average vertical-skin-frictional resistance, k_v; and bearing resistance,

k_q, were calculated for two soil layers surrounding the piles. Table 7.2 shows the values for the soil properties of each layer used in the analytical model.

Table 7.2. Soil properties ANSYS model

Layer	N	C_u (psi)	k_v (psi)	k_q (pci)
1	15	11.1	12430	4000
2	19	14.9	11949	5360

The values of k_v and k_q, shown in Table 7.2, were calculated using methods put forward by Abendroth and Greimann (2005). In their work k_v and k_q were then used in equations that describe the non-linear P-Δ properties of soil. However, in this work k_v and k_q are used in Equations 7.1 and 7.2 to calculate the stiffness for the vertical soil springs in the ANSYS model.

$$K_v=k_vLp \quad (7.1)$$

$$K_q=k_qA_p \quad (7.2)$$

where,

K_v = skin-friction soil-spring resistance

K_q = end-bearing soil-spring resistance

L_p = tributary pile length for each soil-skin-friction soil-spring

A_p = cross-sectional area of the pile tips

7.2.4 Boundary Conditions

Two sets of boundary conditions were analyzed. The purpose for running the analysis with two sets of boundary conditions was to develop an envelope of the axial loads in the piles, and to study the restraining effect girders might have on the abutment.

In first set of boundary conditions, only the soil springs support the structure in the vertical direction, and horizontal movements of the piles are restricted. The piles and the abutment are connected though sharing a common node at the pile/abutment interface. The

piles must be restricted from horizontal movements, because the soil springs have three degrees of freedom at each node, and the purpose of the soil springs is only for vertical restraint. Also, the soil spring node not attached to the pile is restricted from all movement (fixed support).

In second set of boundary conditions the composite-girders are included in the model. They each share a single node at the girder/abutment interface at the location of their respective neutral axes. The composite-girders were modeled as full-length, straight girders. The lengths of each span corresponded to the actual span lengths, along the curve, of Bridge 309. Both pier locations were modeled as pinned supports with all displacement fixed and rotations about the transverse and vertical axis fixed. The abutment at the opposite end is assumed as a fixed support and, as such, all movements at that location are restricted. The boundary conditions for the piles and the spring elements are the same as those for the first set of boundary conditions. Figure 7.8 shows the boundary conditions applied to the soil springs, abutment piles, and composite girders.

7.2.5 Loading Conditions

The first step in the analysis was to run a thermal conduction study. The abutment was modeled SHELL57 and the appropriate material thermal properties, both covered previously. A temperature of 26 °F was applied across the top of the abutment and a temperature of -26 °F was applied across the bottom of the abutment. The temperatures were chosen as a result of the measured abutment and pile temperature data described previously for Bridge 309. From these inputs, ANSYS generated a temperature gradient though the abutment and stored the information in a .rth file. The information from the .rth file was then used as temperature loading in a thermal stress analysis. Figure 7.10 displays the thermal gradient through the abutment as a result of the thermal conduction analysis.

As one might expect from an analysis such as this, the temperature gradient though the abutment is nearly uniform. The slight variation from one vertical face to another is the result of the height variation from one wingwall to the other.

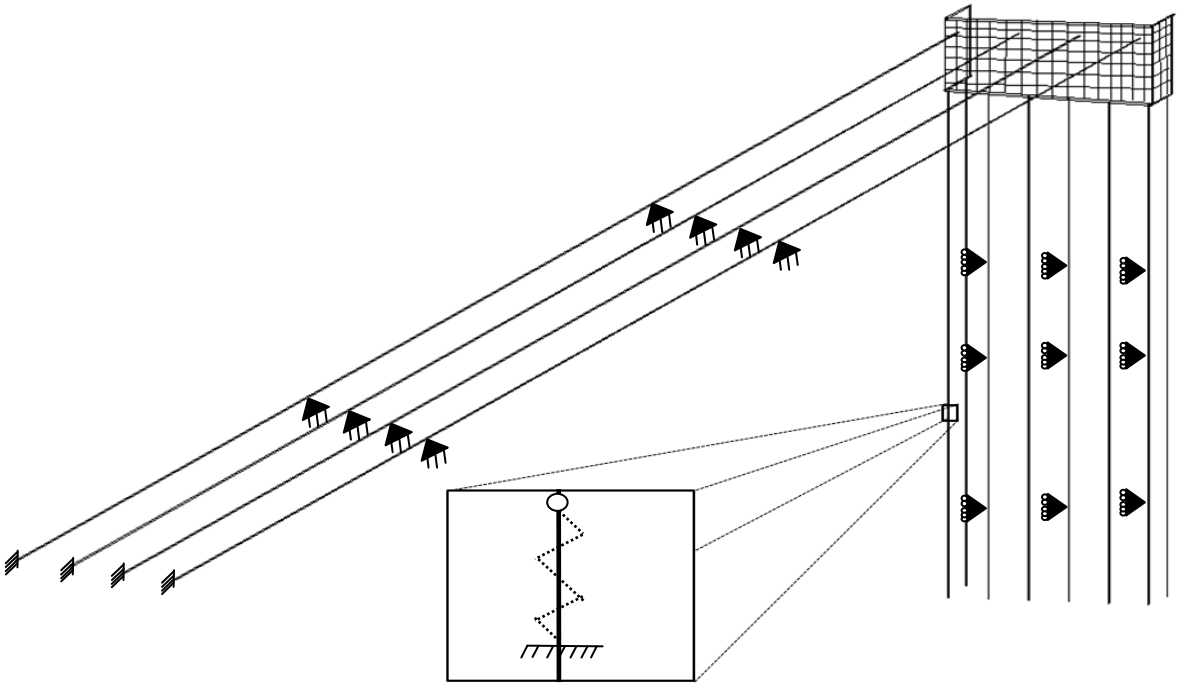

Figure 7. 8. Model boundary conditions

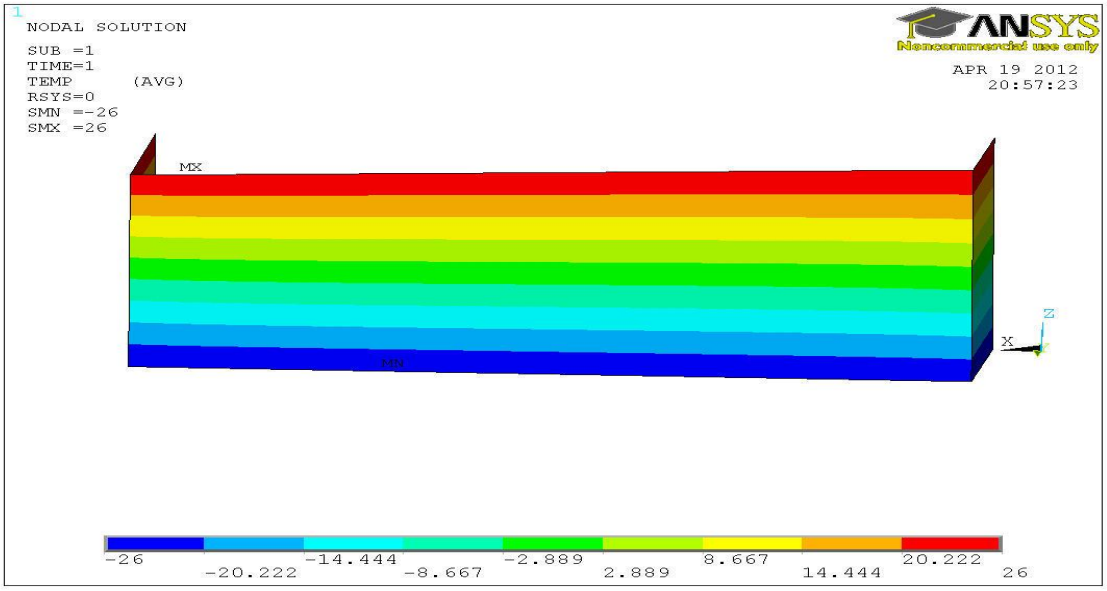

Figure 7.9. Abutment temperature gradient

7.3 RESULTS

7.3.1 Model without Girders

The first analysis run was modeled with boundary conditions set one. Figure 7.11 shows the deformation that took place as a result of the thermal stress in the abutment without the composite girders.

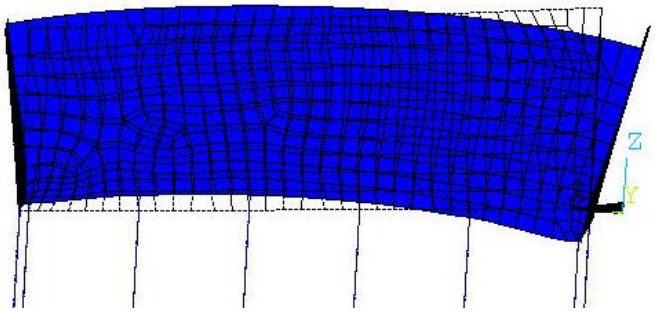

Figure 7.10. Model deformation – boundary set one

As shown in Figure 7.11, the model takes on a convex shape as a result of the thermal stresses. The bending is not completely symmetric due to the slightly unsymmetrical geometry of the abutment. It should be noted that the deformation was exaggerated to produce more visible results.

Along with the plotted deformation, the axial loads in the abutment piles were determined from the analysis; the results of which are shown in figure 7.12. As expected, a temperature gradient in the abutment caused differential axial loading in the piles. The results are similar to those seen in the experimental data for Bridge 309 with interior piles 5 and 6 experiencing high tension loads, and the exterior piles experience either low tension or compressions loads. Note the majority of the load is carried by the skin-friction soil-springs as opposed to the end-bearing soil-springs. This is consistent with a friction pile system typical of clay soils without a rock foundation.

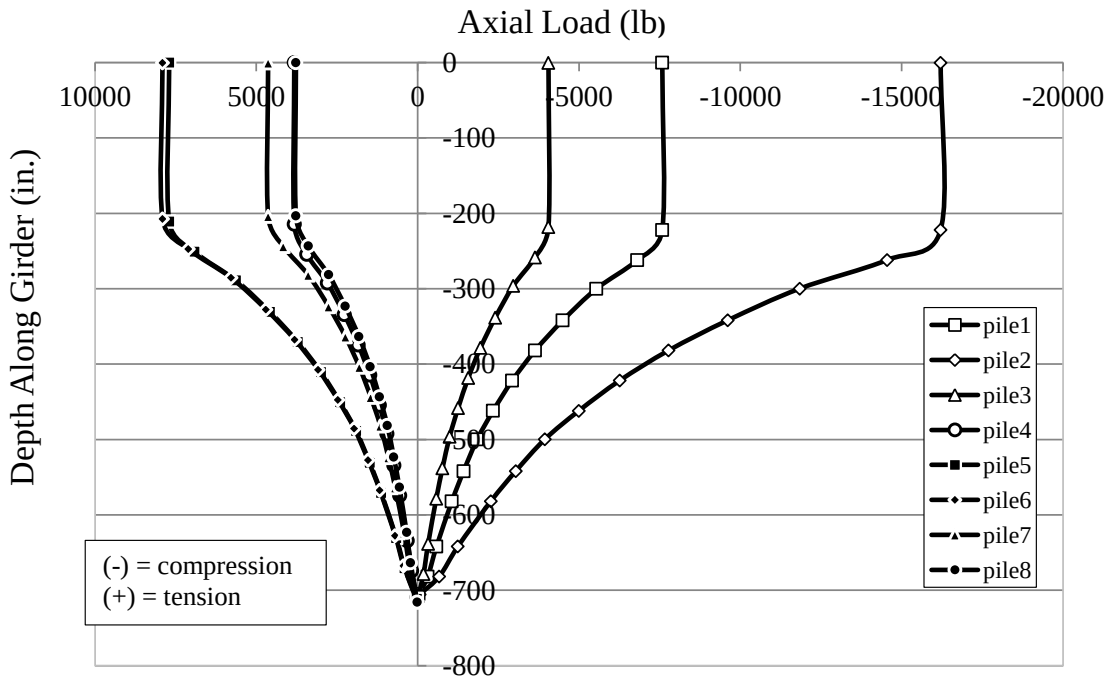

Figure 7.11. Axial load results – boundary set one

The second analysis run was modeled with boundary conditions set two. Figure 7.13 shows the deformation that took place as a result of the thermal stress in the abutment with the composite girders.

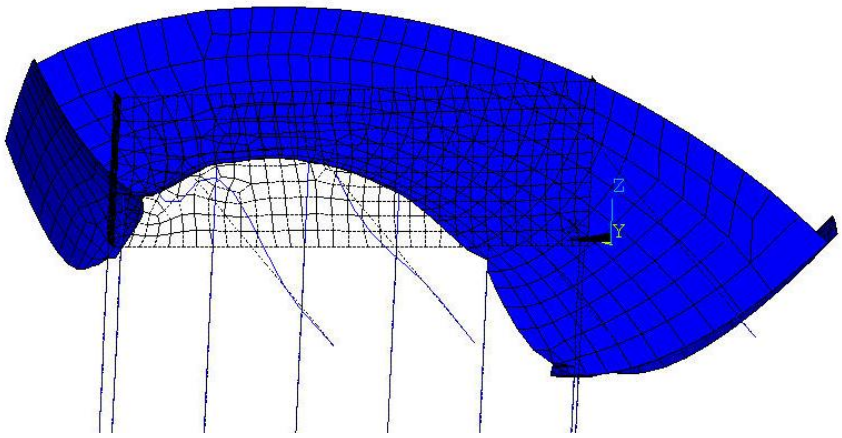

Figure 7.122. Model deformation – boundary set two

As shown in Figure 7.13, the model takes on a more complex shape compared to the first analysis. This is a result of the composite girders influencing the deformation of the abutment. Since the composite girders act on the abutment only through their neutral axis, less surface area is restrained than would occur in reality. Lastly, no boundary conditions were applied to the abutment itself while in all actuality there would be restraint in all directions from the surrounding soil. Initially, to address the abutment restraint by the soil, simple restraint conditions were employed. However, all attempts over constrained the model and model deformations were unrealistic, and, as a result, the abutment was left unrestrained. A more realistic model would incorporate soil springs to restrain the abutment.

Along with deformation, the axial loads in the piles were analyzed; the results of which are shown in Figure 7.14. As before, the temperature gradient in the abutment caused differential axial loading in the piles. The results from the second analysis are similar to the first. The exterior piles 1, 2, and 8 all experience compression loads, the interior piles 4, 5, and 6 all experience tension loads. Interior pile 3 shows a slight compression load and the exterior pile 7 shows a moderate tension load.

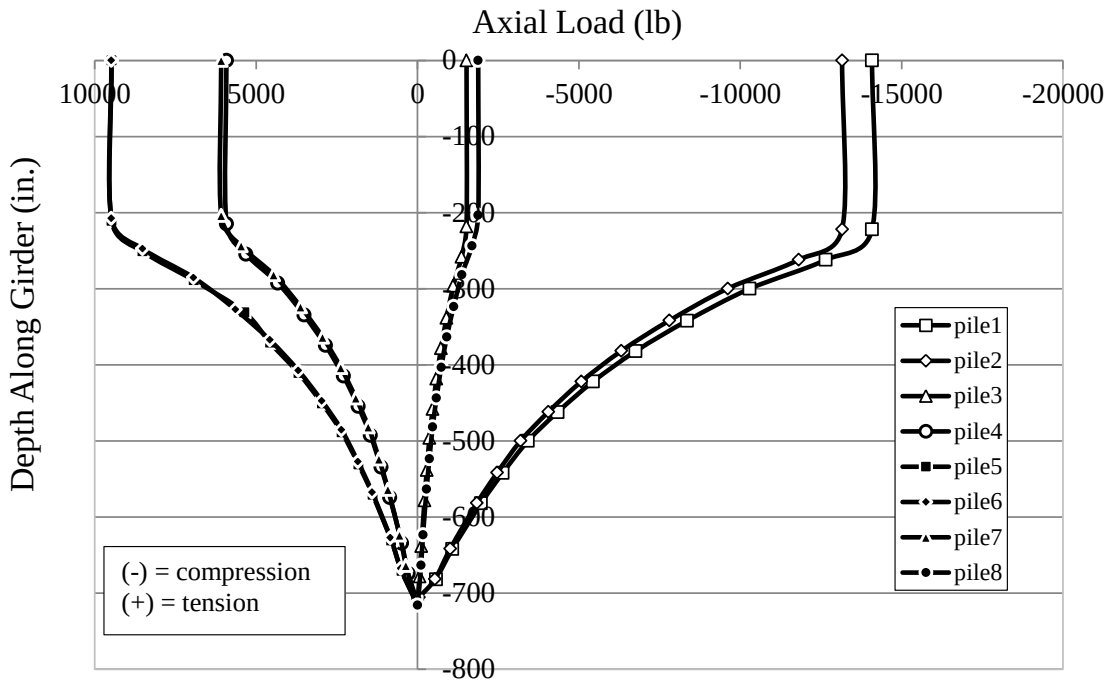

Figure 7.133. Axial load results – boundary set two

7.4 CONCLUSIONS AND RECOMMENDATIONS

Based on the findings of the two analytical models and the data collected during the life of the project, there is reasonable evidence to suggest that a vertical thermal gradient in an integral abutment could induce differential axial loading in the abutment piles. Both models generally showed increased axial tension in the interior piles and increased compression in the exterior piles, as was suggested by the abutment pile strain-gauge data. However, due to the unrealistic nature of the models (e.g. soil restraint on abutment), the degree to which abutment and superstructure geometry can vary between bridges, and the complexities of the abutment-soil and pile-soil interaction, suggesting that the models used in this analysis were accurate predictors of the axial load is an unreasonable conclusion from this work.

Further investigation into the effects that an abutment vertical thermal gradient could have on abutment pile axial loads is suggested. A more complex analytical model utilizing non-linear soil springs in both the horizontal and vertical direction, and a more realistic girder-abutment and pile-abutment connection detail along with empirical data correlation is suggested.

CHAPTER 8 SUMMARY, CONCLUSIONS, AND RECOMMENDATIONS

This chapter presents a summary of the project approach, a discussion of the measured results, conclusions drawn from those results, and recommendations developed by the research team.

8.1 SUMMARY OF PROCEDUE

The reconstruction of the NEMM provided the opportunity to monitor the behavior of straight and horizontally-curved, steel-girder, integral-abutment bridges. There were six, 26-ft-wide roadway bridges included in this work. The interchange design was such that two straight-girder bridges were constructed with integral abutments, two curved-girder bridges were constructed with semi-integral abutments with expansion joints, and two curved-girder bridges were constructed with integral abutments.

The typical instrumentation plan for each bridge consisted of four girder strain-gauges at the mid-span of exterior girders on select spans, temperature sensors embedded into the concrete deck, and expansion meters strategically placed between the bottom flange of the girders and the pier-cap and the abutment-cap. On Bridge 309, six abutment piles were also instrumented with strain gauges approximately ten inches below the bottom of the pile cap, long range displacement meters were installed at each abutment and pier, and pressure cells were installed on the back face of the abutment backwalls. The bridges were monitored for a period of approximately 15 months.

Along with the electronic instrumentation placed on the bridges, each of the six bridges was outfitted with eight prismatic reflectors for the purpose of performing monthly surveys of the bridges. These reflectors were placed on the bottom flange of the exterior girders near both abutments and both piers.

8.2 SUMMARY OF RESULTS

Composite Girder Strains and Forces

The axial-strain range, $\Delta\varepsilon_a$, at measured locations was between 70 με and 220 με for all six bridges, with an average value of 153 με. The strong-axis-bending strain range, $\Delta\varepsilon_x$, at the monitored girder locations was measured between 20 με and 110 με, with an average

value of 73 με. The monitored lateral-bending strain range for the top and bottom flanges were measured between 10 με and100 με and 10 με and 120 με, respectively. The top flange lateral-bending strain range had an average value of 31 με and the bottom flange lateral-bending strain range had an average value of 21 με.

The axial-force range, ΔP, for all six bridges ranged from 70 kip to 770 kip with an average value of 596 kip. The strong-axis-bending moment ranged from 1200 kip-in. to 6300 kip-in. with an average value of 4400 kip-in. The lateral-bending strain range for the top and bottom flanges were between 13 kip-in. and 260 kip-in. and 12 kip-in. and 260 kip-in. with an average value of 43 kip-in. and 42 kip-in., respectively.

Abutment Steel Pile Strains

The axial-strain range, $\Delta\varepsilon_a$, in the six abutment pile instrumented locations was measured between 60 με and 120 με, with an average value of 83 με. The strong-axis-bending strain range, $\Delta\varepsilon_x$, was measured between 140 με and 240 με, with an average value of 198 με. The weak-axis-bending strain range, $\Delta\varepsilon_y$, was measured between 590 με and 900 με, with an average value of 750 με. The torsional-warping strain range, ε_t, measured from 20 με to 60 με, with an average value of 39 με.

The strain ranges in the piles show only a few discernible relationships with the geometry of Bridge 309. The strong-axis bending-strain ranges are highest for HP6s, closest to Girder D. HP4s, closest to the interior girders; show the next highest strong-axis-bending strain ranges, followed by HP1s, closest to Girder A. The weak-axis-bending strain ranges are highest for HP1s, followed first by HP4s, and then HP6s. This result might be expected since Girder A is nearly eight feet longer than Girder D.

Abutment Backwall Pressure

The measured backwall soil pressure ranges were higher at the north abutment than those at the south abutment. For the north abutment the range in the west pressure cell and the east pressure cell were approximately 10 psi and 20 psi, respectively. For this abutment, the soil pressure range at the obtuse side of the skewed abutment shows a greater soil pressure range than at the acute side of the skewed abutment. This result is consistent with work presented in Abendroth and Greimann (2005). Both the west and east pressure cells on the south abutment measured approximately 8 psi for the soil pressure range against this abutment

backwall.

The estimated axial forces in the girders due to the soil pressures against the abutments were much lower than these forces that were computed from the measured girder strains. The discrepancy in the girder axial forces can be explained by other restraining forces, such as forces from the piers, piles, and pavement. Also, by assuming linear soil pressure on the abutment back wall and equal girder force distribution made during the calculation can lead to errors in these results as well.

Bridge and Span Change in Length

The measured total change in length, $\Delta L_{measured}$, of the six bridges ranged from 1.54 in. to 2.15 in., with an average value of 1.77 in. The total change in length values by free expansion theory, ΔL_{free}, ranged from 2.14 in. to 2.32 in. The total change in length by free expansion theory provides a conservative estimate, on average 0.43 in. or 26% higher than the measured value. The average axial girder strain calculated from the difference between ΔL_{free} and $\Delta L_{measured}$, $\Delta\varepsilon_r$, ranged from 43 με to 154 με with an average value of 113 με. This average is 51 με or 34% lower than the measured value.

For each three span bridge, the center spans experienced the greatest change in length. For all six bridges, the change in their center span lengths range from 0.59 in. to 0.75 in. with an average value of 0.70 in. The average difference for the change in the center span length between the inside and outside girders was 0.03 in. or 5%. The change in length of the center span for the bridge with an acute skew angle at the outside girder ranged from 0.32 in. to 0.58 in. with an average value of 0.43 in. The average difference in this span length between the inside and outside girders was 0.043 in. or 10%. The change in length of the center span for the bridges with an obtuse skew angle at the outside girder ranged from 0.30 in. to 0.50 in. with an average value of 0.41 in. The average difference in this span between the inside and outside girders was 0.06 in. or 18%. For all six bridges, the difference in the span length between the two end spans, for all six bridges, ranged from 0.015 in. to 0.045 in. with an average value of 0.03 in. or 7%.

Abutment and Pier Displacements

As shown in the bridge deflected shape figures presented earlier, the girders typically expanded during warmer temperatures and contracted during colder temperatures. Generally,

longitudinal bridge displacement at expansion piers would show a larger displacement range than that at fixed piers. One of the semi-integral abutment bridges, Bridge 209, shows a larger displacement range at the abutments than that for all of the integral abutments, but the other semi-integral abutment bridge, Bridge 2309, shows a displacement range similar in value to most of the integral abutments.

Effective Thermal Length

An effective thermal length was calculated for all fixed bearing locations. The effective thermal lengths for the integral abutments were all longer than the length of their respective adjoining span. The difference in the effective thermal length and the length of the adjoining span varied from 12% to 94%. The effective thermal lengths for the fixed piers were all shorter than the longest adjacent span. The difference in the effective thermal length and the longest adjoining span ranged from 20% to 68%. In situations where the center span is between two fixed piers, the Iowa DOT uses half the length of the center span for the effective thermal length. The effective thermal length used by the Iowa DOT is conservatively longer by an average of 34% when compared to the effective thermal lengths obtained from this study.

Fixed and Expansion Pier Displacement

According to collected data, the range in the girder-to-pier relative displacements were around 0.6 in. The displacements essentially show a linear relationship with regard to the effective bridge temperature until the temperatures approached 100 °F and 0 °F at which point they behave nonlinear. A correlation between the survey and expansion meter results varied from month to month. In some cases the two data sets overlap one another and in some cases they show a difference of up to 0.2 in. This inconsistency most likely stems from accuracy issues within the survey data.

The data show that there is a relative girder-to-pier displacement of the pier in the direction perpendicular to its longest cross-sectional dimension. According to the surveying results, the displacement can range anywhere from 0.3 in. to 0.6 in and varies linearly with the effective bridge temperature.

Abutment Steel Pile Cantilever Model

The results from the abutment steel pile equivalent cantilever model, as described by

Abendroth and Greimann (2005), fell short of accurately predicting the relationship between the weak axis bending strain in the piles and the pile head displacement. According to the strain gauge data and the survey results, the measured strain was anywhere between 50—150 με higher than the values predicted by the model. The accuracy of the survey data could be a possible explanation for the difference in results, as well as a possible difference between the actual pile pre-bore depths and the pre-bore depths shown on the plan, effectively shortening the effective length and increasing the resulting strains.

Abutment Steel Pile Strain vs. Expansion

According to the measured strains and displacements, the abutment steel pile strains and the bridge expansion show a linear relationship. According to the data, the SAHP1 pile shows a strain range of approximately 470 με under roughly 0.95 in. displacement, the SAHP4 pile shows a strain range of approximately 600 με under 0.75 in. displacement, and the SAHP6 pile shows a strain range of approximately 620 με under a 0.75 in. displacement. Also according to the data, the NAHP1 pile shows a strain range of approximately 650 με under a 0.95 in. displacement, the NAHP4 pile shows a strain range of approximately 620 με under a 0.95 in displacement, and the NAHP6 pile shows a strain range of approximately 610 με under a 0.70 in. displacement.

8.3 CONCLUSIONS AND RECOMMENDATIONS

Internal Composite Girder Strains and Forces

The internal axial girder strain showed the largest ranges of all the resulting strains from the measured girder strain gauge data, with the largest range being 220 με. For Grade 60 steel the resulting stress is 6.4 ksi or roughly 11% of the yield stress. By superimposing the four calculated internal strains, the results can exceed 400 με, giving 11.6 ksi or 19% of yield stress for Grade 60 steel. Although the composite girders have substantial resistance to the effects of thermal loading, this does not consider the effects of other loading conditions.

Abutment Steel Pile Internal Strains

The relationship between abutment steel pile internal axial strain and effective bridge temperature varied depending on the pile location with respect to the abutment pile cap. The measured results showed either a proportional, inversely proportional, or erratic relationship between internal axial strain and effective bridge temperature. This behavior could impact

design and further investigation into the phenomena should be undertaken.

The greatest weak axis bending strain, in fact the greatest of all the measured strains, to be resisted by any of the monitored abutment piles was the NAHP1 pile at 900 με. The stress in the section because of the strain equals 26.1 ksi, which amounts to 44% of the yield stress for Grade 60 steel. When considering just weak axis bending, the HP 10x57 piles used as support for the integral abutments in this study had appropriate resistance.

By superimposing the four different abutment pile internal strain ranges on one another, the largest possible strain felt by any of the piles was 1225 με. The stress in the section equates to 36 ksi or 60% of the yield stress of Grade 60 steel. From the results of this study, the piles used for support of the integral abutments at the NEMM had sufficient resistance to thermal expansion; however this is without considering the effects of other loading conditions. Further investigation into the behavior of abutment piles of horizontally curved integral abutment bridges is suggested.

Bridge and Span Change in Length

Based on the results, there is a close correlation between the movements measured by the electronic equipment and by the monthly survey. Also, according to both, free bridge expansion by

REFERENCES

Abendroth, E. R., and L. F. Greimann. (2005). *Field Testing of Integral Abutments*. Iowa DOT Projext HR-399. Ames, Iowa: Highway Division, Iowa Department of Transportation. CD-ROM.

American Institute of Steel Construction Inc. 2007. *Steel Construction Manual Thirteenth Edition*. United States: American Institute of Steel Construction, Inc.

Barker, R. M., J. M. Duncan, K. B. Rojiani, P. S. K. Ooi, C. K. Tan, and S. G. Kim. 1991. *Manuals for the Design of Bridge Foundations*. NCHRP Report 343. Washington, DC: Transportation Research Board, National Research Council.

Coduto, Donald P. 2001. *Foundation Design Principles and Practices: Second Edition*. New Jersey: Prentice Hall

Doust, S. 2011. *Extending Integral Concepts to Curved Bridge Systems*. Ph.D. dissertation, University of Nebraska.

Geokon 2004. *Instruction Manual Model 4700 VW Temperature Gage*. Lebanon, NH: Geokon

Geokon 2008. *Instruction Manual Model 4420 VW Crackmeter*. Lebanon, NH: Geokon

Geokon 2009a. *Instruction Manual 3800/3810 Thermistors & Thermistor Strings*. Lebanon, NH: Geokon

Geokon 2009b. *Instruction Manual Model 4427 VW Long range Displacement Meter*. Lebanon, NH: Geokon

Geokon 2009c. *Instruction Manual Model VK-4100/4150 Vibrating Wire Strain Gages*. Lebanon, NH: Geokon

Geokon 2010. *Instruction Manual Model 4800, 4810, 4820, and 4830 VW Earth Pressure Cells*. Lebanon, NH: Geokon

Hall, D. H., M. A. Grubb, and C. H. Yoo. 1999. *Improved Design Specifications for Horizontally Curved Steel Girder Highway Bridges*. NCHRP Report 424. Washington, DC: Transportation Research Board, National Research Council.

Hassiotis, S., Y. Khodair, E. Roman, and Y. Dehne. 2006. *Final Report Evaluation of Integral Abutments*. Hoboken, New Jersey Department of Transportation, Division of Research and Technology.Moorty, S., and C. W. Roeder. 1992. Temperature-Dependent Bridge Movements. *Journal of Structural Engineering* 118: 1090—105

Offices of Bridges and Structures. 2011. *LRFD Bridge Design Manual*. Ames, IA. Iowa Department of Transportation.

Priestley, M. J. N., F. Sieble, and G. M. Calvi. 1996. *Seismic Design and Retrofit of Bridges*. New York. John Wiley & Sons, Inc.

Richardson, Gordon and Associates. 1976. *Curved Girder Workshop.* Pittsburgh, PA: Federal Highway Administration, Offices of Research and Development.

Salmon, C., J. Johnson, and F. Malhas. 2009. *Steel Structures: Design and Behavior*. Fifth Edition. New Jersey: Prentice Hall

Shah, B. 2011. *3D Finite Element Analysis of Integral Abutment Bridges Subjected to Thermal Loading*. M.S. Thesis, Kansas State University.

Thanasattayawibul, N. 2006. *Curved Integral Abutment Bridges*. Ph.D. dissertation, University of Maryland.

The Engineering ToolBox. 2012. *Material Properties.* http://www.engineeringtoolbox.com/material-properties-t_24.html.

Tennessee Department of Transportation.1996. Highway Structures Design Handbook. Volume II, Chapter 5. Integral Abutments for Steel Bridges. U.S.A: American Iron and Steel Institute, National Steel Bridge Alliance.

Topcon Corporation. 2007. *Pulse Total Station GPT-7500 Series*. Instruction Manual. Tokyo, Japan

Vasant, C. Mistry. *Integral Abutment and Jointless Bridges.* Washington, DC: Federal Highway Administration